DEVELOPMENT OF BRIGHT LUMINESCENT SILICA NANOPARTICLES

A Dissertation

Presented to the Faculty of the Graduate School

of Cornell University

In Partial Fulfillment of the Requirements for the Degree of

Doctor of Philosophy

by

Srikant K Iyer

January, 2014

ABSTRACT

DEVELOPMENT OF BRIGHT LUMINESCENT SILICA NANOPARTICLE

Srikant K Iyer, Ph. D.

Cornell University 2014

Silica based luminescent nanoparticles provide tremendous potential as biocompatible and robust inorganic materials in nanobiotechnology and nanomedicine. Sol-gel derived silica act as excellent host for covalently encapsulating organic fluorophores to enhance brightness while independently controlling the size of the nanoparticle.

The first part of this dissertation describes the development of bright multicolor fluorescent silica probes in a layer by layer approach. Three spectrally distinct dyes (green, blue and red) were incorporated in three different levels or number of dyes per particle (0, 5, 20) to generate twenty-six spectrally distinguishable nanoparticles. Each particle was designed by precisely controlling the number of dyes per particles and each dye layer was spatially separated by blank silica shell to minimize energy transfer. These particles were used to demonstrate fluorescence multiplexing via cellular uptake.

The second part of this thesis describes development of chemiluminescence based probes. Template based near-infrared dye was covalently incorporated into mesoporous silica nanoparticles seems to orient the dye such that the non-radiative pathway disappears resulting in brightness enhancement for chemiluminescence. These highly porous nanoparticles facilitated the diffusion of the reactive precursor resulting in chemiluminescence. These particles along with polybase additives were used to tune the kinetics of photon emission.

BIOGRAPHICAL SKETCH

Srikant K. Iyer was born in New Delhi, India to Jayshri and Kannan on April 28th, 1982. The elder of their two sons, Srikant was socially amicable which made him easy to talk to and make friends very easily. His father was his greatest professional influence. At the tender age of 2, he was taught the Archimedes principle, and would enact 'Archimedes' reaction' within the confines of his home.

Srikant graduated from high school and went on to graduate with B.S. in honors in Chemistry at Delhi University. His interest in research began to take shape when he worked on projects in National Laboratory during his summer vacation. His perception of science further evolved after joining Indian Institute of Technology, Delhi. Here he was exposed to various scientific concepts and modeling, but it was with the able support and mentoring of his professors and his father that he began to explore the world of nanoscience and nanotechnology. After graduating from IIT, Delhi he joined The University of North Carolina at Charlotte and had the experience to carry out synthesis of quantum dots as a Master's student. He was awarded the Thomas Walsh scholarship for being an outstanding graduate student.

For his PhD, Srikant was accepted in the Department of Chemistry and Chemical Biology at Cornell University in 2007. In his quest to work towards a more application based field, he joined the Wiesner group in the Department of Material Science and Engineering. Here he started working on incorporating organic fluorophores into silica nanoparticles. He went on to work towards developing bright luminescent probes for his thesis dissertation. Srikant completed his doctoral work in summer, 2013.

"Over the years, I've learned how to avoid huge

amount of pitfalls by walking

into them and surviving" – Louis CK

ACKNOWLEDGMENTS

First and foremost, I would like to thank Prof. Uli Wiesner for taking a chance and being patient with me for all these years. I have learned how to plan, execute and write in a scientific manner. He has been an immense support as a mentor and has helped me grow as a person and a scientist. I also thank Prof. Warren Zipfel for his unconditional support and guidance during my scientific journey at Cornell University. I also thank my committee members Prof. Chakesha Liddell Watson and Prof. Lara Estroff who were very helpful in taking the time to discuss my progress as a graduate student at Cornell University.

I am deeply indebted to the past and present members of the Wiesner group. Dr. Andrew Burns, Dr. Erik Herz and Dr. Teeraporn Suteewong were very supportive and taught me everything about silica based fluorescent particles and were very helpful as mentors during and after graduating from the group. Dr. Chris Orillal and Dr. Morgan Stefik were very insightful in making scientific suggestions. I would like to thank my co-workers Zihui Li, Jennifer Drewes, Yao Sun, Christina Cowman-Eggert, Xian Shi, Spencer Robbins, Kwan Wee Tan and Kahyun Hur who were always willing to participate and offer ways to improve my experiments. I would like to especially mention Teresa Kao, Ketat Sarakune, Jake Brown, Kai Ma, Hiroaki Sai, Jörg Werner, Marcus Wilkes, Dr. Roy Cohen and Dr. Tobias Hoheisel who were always around to bounce ideas off helped me mould my thought process to further my goal as a PhD student in the Wiesner group. Finally, I would like to thank Rachel Mika Dorin and Dolores Dewbury who were great emotional support and helped me re-define my perspective as a researcher.

My journey as a Cornell graduate student would be incomplete without mentioning my friends who were instrumental in maintaining the strong support system that made each year memorable. I would like to thank Chinmayee Subban, Pinshane Huang, Natalie Henkhaus, Cassie Hobbs, Will Baumgardner, Arthur Barnard, Syud Momtaz Ahmed, Ry Forseth, Ryan Henderson and Nikhil Fernandez for keeping me grounded and making every moment at Cornell memorable. I would like to thank Marie Krysak my 'work spouse' who made every day at Duffield fun and helped soak up the daily pressures at lab. Deirdre Costello, Diarmuid Cahalane, Avtar Singh, Kylan Szeto and Mohanram Gudipati helped me "keep it real" by making sure my emotions were in check. They were selfless in making time and space for me in time of crisis. Clea Weiss and Inish O'Doherty, introduced me to Crossfit, which made me physically and mentally stronger. I would like to reach out to Penny DeLong Burke, Sarah Ploss, Lap Wang, Elizabeth Keokosky, Bill Keokosky, Sofia Keokosky, Kalpana Raman, Subbu, Varun Subramaniam, Tony Krysak, Debbie Krysak and Allison Perotti for lending perspective to my life and helping me recognize the importance of appreciating the little things.

Finally, my family, Jayshri Kannan, K. Kannan and my brother Abishek K Iyer whose constant support and desire to see me succeed kept me focused on the goals at hand. I am grateful to all of you for the sacrifices you made as I grew up, and for putting up with my tantrums, both as a child and as an adult.

TABLE OF CONTENTS

LIST OF FIGURES

LIST OF TABLES

LIST OF ABBREVIATIONS

CL – Chemiluminescence

CTAB – hexadecyltrimethylammonium bromide

CPPO – bis-(2-carbopentyloxy-3,5,6-trichlorophenyl)oxalate

Cy5m – Cy5-maleimide

DACm – N -(7-dimethylamino-4-methylcoumarin-3-yl)maleimide

DMSO – dimethylsulfoxide

dSNP – dye coated silica nanoparticles

dMSN – dye incorporated mesoporous silica nanoparticles

FCS – Fluorescence correlation spectroscopy

FRET – Förster resonance energy transfer

GSB – Ground state bleach

LbL – layer by layer

NIR – Near infrared

PDMAEMA – poly(*N*,*N*-dimethylaminoethyl methacrylate)

PEI – polyethyleneimine

PEG silane – polyethyleneglycol silane

PI-*b*-PDMAEMA – poly(isoprene–*block*–*N*,*N*-dimethylaminoethylmethacrylate)

POCL – Peroxyoxalate chemiluminescence

PIA – Photo-induced absorption

RI – Reactive intermediate

TA spectroscopy – Transient Absorption spectroscopy

TMRm – tetramethylrhodamine-5-maleimide

TEOS – tetraethylorthosilicate or tetraethoxysilane

SEM – Scanning electron microscopy

TEM–Transmission electron microscopy

CHAPTER 1

INTRODUCTION

Luminescence-based techniques are powerful tools used in modern biological research and sensing for quantitative analytical measurements with molecular contrast on a large range of length scales.[1,2] Luminescence is the emission of photons from electronically excited species and is classified based on the mode of excitation source.[3] Fluorescence and chemiluminescence based detection are particular cases of luminescence commonly used due to high sensitivity and selectivity along with advantages of spatial and temporal resolution. In both cases, emission of photons is a result of deactivation of an electronically excited species, however mode of excitation for fluorescence is a result of absorption of photons, where as chemiluminescence is a result of chemical process.[3] Different classes of organic and inorganic luminescent emitters exist that are used to label molecules of interest like proteins, nucleic acids, ions, cells etc.[4–7] These probes have their own advantages and shortcomings with regard to biological imaging and sensing. Among the important parameters to consider are spectral properties, probe brightness, photostability, toxicity and size.[8] In order to facilitate these developments bright, photostable probes of suitable size need to be generated.

The smallest fluorescent emitters in use today are single organic or metal organic dye molecules which are available with emission spectra across the spectrum from UV to near infrared (~ 300-900 nm).[4] These emitters besides having a relatively low quantum yield are also susceptible to photobleaching and quenching. Another class of fluorophores is fluorescent proteins which are a product of gene transcription.

These have the similar brightness as organic fluorophores and are susceptible to photobleaching and quenching.[4] Besides organic based probes, colloidal luminescent probes have found applications in the field of imaging. Quantum dots are one such example, which are traditionally semiconducting nanoparticles which range in size from 5-20 nm and the emission can be tuned based on the size of the nanoparticles. Quantum dots are bright, photostable particles and provide a distinct advantage over organic fluorophores and fluorescent proteins.[8] On the other hand these particles due to the presence of heavy metals act as cytotoxins and are hence not desirable for *in vivo* applications.

Hybrid organic/inorganic silica based nanoparticles have been developed as biocompatible materials.[8–13] Silica is a robust biocompatible material with well-defined tunable properties like morphology, size, porosity and surface chemistry. Silica surface can be easily modified with appropriate functional groups via well established siloxane chemistry thus making them viable for diagnostic and therapeutic applications.[10] Currently two types of silica based nanoparticles are extensively used: silica nanoparticles and mesoporous silica nanoparticles. The synthesis of these particles is based on sol-gel process involving hydrolysis and condensation of a silicon alkoxide precursor, typically tetraethoxysilane (TEOS).

Silica nanoparticles are typically synthesized via reverse microemulsions and Stöber method. Silica nanoparticles fabricated by reverse microemulsion method are synthesized in an aqueous medium confined within a surfactant micelle in a non-polar solvent to obtain monodisperse colloids.[14] The free dyes were physically encapsulated into the confined particles, which poses issues towards dye leaching over a period of

time.[8] Alternately, in the Stöber method monodisperse, electrostatically-stabilized silica nanoparticles were synthesized under ambient conditions by carrying out the reaction in an ethanol solvent system in the presence of water and ammonia.[15] Mesoporous silica nanoparticles are synthesized in an aqueous medium using surfactants that act as structure directing agents and are located in pores of the silica matrix.[8,16–18] The intrinsic properties of these materials, such as high surface area, uniform pore distribution and large pore volume make them highly desirable as probes for sensing, biomedical imaging and as drug delivery carriers.[17–23] Since the development of MCM-41 type particles, extensive research has been carried out to synthesize monodisperse, well defined hexagonally ordered mesoporous silica particles (Figure 1.1).[16,18,23,24] Covalent incorporation of organosilanes, and other metal oxides have been successfully carried out while preserving the porosity and morphology of MSNs.[25,26] These materials have been extensively studied as a drug delivery vehicle system.[9,17,19–23]

1.1 Bright dye incorporated fluorescent silica nanoparticles

The Stöber method was modified by co-condensing the organic fluorophore-silane conjugate with TEOS, resulting in micron sized covalently incorporating organic fluorophores silica particles.[16] Wiesner *et al.* developed bright fluorescent nanoparticles called Cornell dots (C dots) that is based on encapsulating small organic fluorophores using a core-shell architecture which were sub-100 nm in diameter (Figure 1.2).[8,12,28] The building blocks of C dots are organic dyes that are conjugated to silica precursors. Following hydrolysis and condensation of these hybrid precursors with pure silica, a dye-rich core is formed. This core can nucleate the growth of a pure

silica shell that encapsulates the organic fluorophores within the core, protecting them from oxidation and preventing dye from leaching out to the external environment. The resulting fluorescent core-shell particles are both bright and photostable with core-shell sizes that can be tuned from nanometers to micrometers by varying the concentrations of reactants during synthesis.[8] The increased brightness of C Dots, when compared to single free dye molecules, is attributed to two factors: the multiplicity of dye molecules in the core as well as per-dye enhancement. The latter phenomenon can be explained by enhancement in radiative decay and reduction in the non-radiative decay modes due to the constriction of dye molecules by the core-shell architecture resulting in increase in quantum yield and thus the per-dye brightness.[29] The silica shell prevents dye molecules from interacting with the environment and is both water-soluble and benign to cells. Spectrally different dye molecules have been encapsulated to generate C Dots along the entire UV-visible to infrared spectrum.[28] This provides biocompatible and bright fluorescent probes for biological applications.[12,19] In order to carry out high throughput screening and high content screening to provide diagnostic information towards diseases and therapeutics fluorescent probes as fluorescence multiplexing needs to be developed.[30–33] Fluorescence multiplexing generally involves spectral separation of different dye species and is facilitated by choosing dyes with minimal overlapping emission spectra to reduce Förster resonance energy transfer (FRET). Furthermore, it is preferable if the spectrally distinct fluorophores involved can be excited using a minimal number of lasers, which can greatly decrease the cost of fluorescence instrumentation. Multiplex encoded beads have been fabricated by different strategies to synthesize multicolor

based beads using fluorescent species in the form of inorganic materials (quantum dots and lanthanides) and organic fluorophores in micron sized particles [20-24] and FRET based silica nanoparticles.[25–30] In order to carry out intracellular imaging the C dot fluorescent nanoparticle platform was expanded towards developing bright and organic dye encoded fluorescent core-shell silica nanoparticles referred to as *multicolor* C dots (*mc*C dots) with sizes below 100 nm for fluorescence multiplexing applications. These multicolor fluorescent core-shell silica nanoparticle probes system is based on multi-dye-ratio-based approach as an alternative method for differentiating between labels, in which the ratio of dye numbers within a single core-shell particle acts as the telling feature. In this novel approach, three fluorescent dyes (green, red and blue) are incorporated into core-shell nanoparticles at three distinct dye concentrations (0, ~5, ~20) in a layer-by-layer fashion resulting in twenty-six different particle combinations. The final particles were coated with polyethylene glycols (PEG) to facilitate stability in buffer conditions and cellular uptake. The photophysical properties of these particles were characterized by a combination of UV-visible spectrometry and fluorometry. The number of dyes per particle and brightness per particle were quantified using fluorescence correlation spectroscopy (FCS). Confocal images of cells containing these particles show potential intracellular imaging applications.

1.2 Bright dye incorporated chemiluminescent silica nanoparticles

Peroxyoxalate chemiluminescence (POCL), a specific example of chemiluminescence is diffusion based process commonly used to detect hydrogen peroxide. [45–49] In POCL the reactive intermediate (1,2-dioxetanedione) is formed as a

result of a reaction between diester oxalate and hydrogen peroxide interacts with the free dye resulting in an electronically exciting the free dye, which subsequently releases photons thereby returning to the ground state.[50,51] Several groups have physically encapsulated organic dyes into peroxyoxalate-based polymer nanoparticles[52,53] and oxalate molecules in nanoparticles[54,55]. Dye leaching and poor stability of oxalate molecules in the particles limits the applications of these particles. Mesoporous silica nanoparticles used to covalently incorporated near infrared dye resulting in dyed mesoporous silica nanoparticles (dMSNs).[56] The covalent incorporation prevented dye leaching and the high mesoporosity of dMSNs facilitated the interaction of the reactive intermediate with the incorporated near-infrared dye. The study revealed that the presence of surfactants caused a specific orientation distribution of the dyes, hence resulting in increased chemiluminescence brightness by switching off of a dark state present only in the free dye. These bright dMSN chemiluminescent probes were used to tune POCL kinetics by polymer additives in the form of polybases which chemically modified CPPO resulting in affecting the rate of formation of 1,2-dioxetanedione.

The focus of this dissertation is developing bright luminescent probes by covalently incorporating organic dyes into sub-100 nm silica based nanoparticles via Stöber method and surfactant directed sol-gel methods. In the first part, detailed description of the synthesis of *mc*C dots is reported with complete characterization with UV-visible spectrometry, fluorometry and fluorescence correlation spectroscopy. The twenty-six particles were spectroscopically distinguishable based on wavelength and fluorescence intensity as a result of brightness enhancements, minimum energy

transfer between the dyes and precise control of the number of dyes per particle. Confocal images showing cells with these sub-100 nm particles indicate the potential applications in intracellular imaging. In the second part, demonstration of template-based dye incorporated mesoporous silica nanoparticles is described. The enhanced chemiluminescence brightness was measured using UV-visible spectroscopy and fluorometry, while transient absorption spectroscopy suggested that an increase in brightness compared the free dye was associated with specific orientation of the dye molecules in the template based particles. Finally, these bright dMSN chemiluminescent probes were used to tune POCL kinetics by polymer additives in the form of polybases which chemically modified the oxalate diester and affecting the rate of formation of 1,2-dioxetanedione.

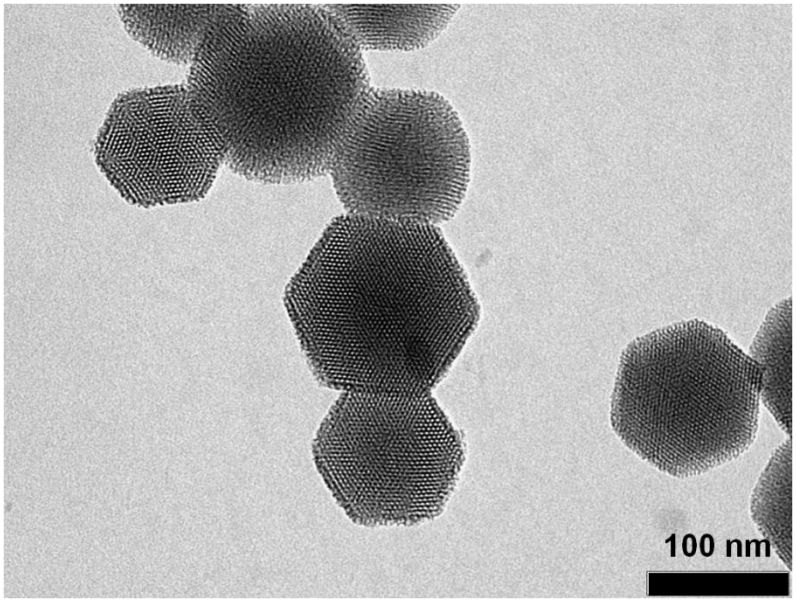

Figure 1.1. TEM image of blank mesoporous silica nanoparticles (MSNs) showing hexagonally ordered pore structure.

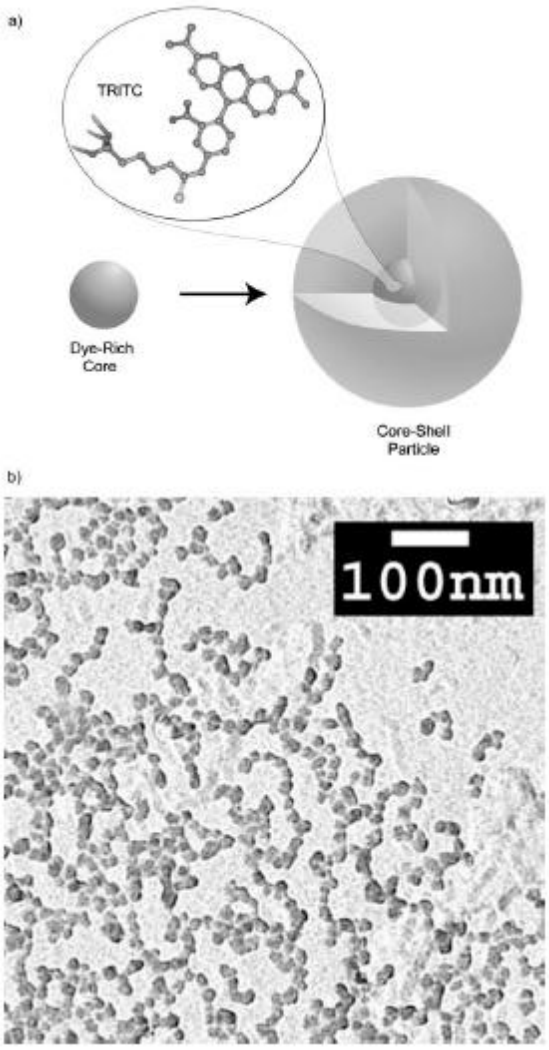

Figure 1.2. (a) Fluorescent core-shell silica nanoparticles or Cornell dots (C dots). (b) SEM images showing monodisperse silica nanoparticles. (Reproduced, in part, with permission from *Nano Lett.*, 2005, **5**, 113-117.[28] Copyright 2005 American Chemical Society)

REFERENCES

(1) Lakowicz, J. *Principles of Fluorescence Spectroscopy*; Lakowicz, J. R., Ed.; third.; Springer US: Boston, MA, 2006; pp. 797–840.

(2) Garcia-Campana, A. *Chemiluminescence in analytical chemistry*; Garcia-Campana, A. M., Ed.; CRC Press, 2001, 2001.

(3) Valeur, B. *Molecular Fluorescence: Principles and Applications*; Wiley-VCH, 2001; Vol. 8, p. 250.

(4) Lavis, L. D.; Raines, R. T. Bright ideas for chemical biology. *ACS chemical biology* **2008**, *3*, 142–55.

(5) Smith, A. M.; Dave, S.; Nie, S.; True, L.; Gao, X. Multicolor quantum dots for molecular diagnostics of cancer. *Expert review of molecular diagnostics* **2006**, *6*, 231–44.

(6) Wang, F.; Tan, W. B.; Zhang, Y.; Fan, X.; Wang, M. Luminescent nanomaterials for biological labelling. *Nanotechnology* **2006**, *17*, R1–R13.

(7) Bonacchi, S.; Genovese, D.; Juris, R.; Montalti, M.; Prodi, L.; Rampazzo, E.; Zaccheroni, N. Luminescent silica nanoparticles: extending the frontiers of brightness. *Angewandte Chemie (International ed. in English)* **2011**, *50*, 4056–66.

(8) Burns, A.; Ow, H.; Wiesner, U. Fluorescent core-shell silica nanoparticles: towards "Lab on a Particle" architectures for nanobiotechnology. *Chemical Society reviews* **2006**, *35*, 1028–42.

(9) Vivero-Escoto, J. L.; Huxford-Phillips, R. C.; Lin, W. Silica-based nanoprobes for biomedical imaging and theranostic applications. *Chemical Society reviews* **2012**, *41*, 2673–85.

(10) Wang, L.; Zhao, W.; Tan, W. Bioconjugated silica nanoparticles: Development and applications. *Nano Research* **2008**, *1*, 99–115.

(11) Wang, L.; Wang, K.; Santra, S.; Zhao, X.; Hilliard, L. R.; Smith, J. E.; Wu, Y.; Tan, W. Watching Silica Nanoparticles Glow in the Biological World. *Analytical Chemistry* **2006**, *78*, 646–654.

(12) Burns, A.; Sengupta, P.; Zedayko, T.; Baird, B.; Wiesner, U. Core/Shell fluorescent silica nanoparticles for chemical sensing: towards single-particle laboratories. *Small (Weinheim an der Bergstrasse, Germany)* **2006**, *2*, 723–6.

(13) Benezra, M.; Penate-Medina, O.; Zanzonico, P. B.; Schaer, D.; Ow, H.; Burns, A.; DeStanchina, E.; Longo, V.; Herz, E.; Iyer, S.; Wolchok, J.; Larson, S. M.; Wiesner, U.; Bradbury, M. S. Multimodal silica nanoparticles are effective cancer-targeted probes in a model of human melanoma. *The Journal of clinical investigation* **2011**, *121*, 2768–80.

(14) Arriagada, F. J.; Osseo-Asare, K. Synthesis of Nanosize Silica in Aerosol OT Reverse Microemulsions. *Journal of Colloid and Interface Science* **1995**, *170*, 8–17.

(15) Stöber, W.; Fink, A.; Bohn, E. Controlled growth of monodisperse silica spheres in the micron size range. *Journal of colloid and interface science* **1968**, *69*, 62–69.

(16) Vallet-Regí, M.; Balas, F.; Arcos, D. Mesoporous materials for drug delivery. *Angewandte Chemie (International ed. in English)* **2007**, *46*, 7548–58.

(17) Fan, J.; Yu, C.; Gao, F.; Lei, J.; Tian, B.; Wang, L.; Luo, Q.; Tu, B.; Zhou, W.; Zhao, D. Cubic mesoporous silica with large controllable entrance sizes and advanced adsorption properties. *Angewandte Chemie (International ed. in English)* **2003**, *42*, 3146–50.

(18) Wu, S.-H.; Mou, C.-Y.; Lin, H.-P. Synthesis of mesoporous silica nanoparticles. *Chemical Society reviews* **2013**, *42*.

(19) Burns, A. A.; Vider, J.; Ow, H.; Herz, E.; Penate-Medina, O.; Baumgart, M.; Larson, S. M.; Wiesner, U.; Bradbury, M. Fluorescent silica nanoparticles with efficient urinary excretion for nanomedicine. *Nano letters* **2009**, *9*, 442–8.

(20) De, M.; Ghosh, P. S.; Rotello, V. M. Applications of Nanoparticles in Biology. *Advanced Materials* **2008**, *20*, 4225–4241.

(21) Park, K.; Lee, S.; Kang, E.; Kim, K.; Choi, K.; Kwon, I. C. New Generation of Multifunctional Nanoparticles for Cancer Imaging and Therapy. *Advanced Functional Materials* **2009**, *19*, 1553–1566.

(22) Tan, W.; Wang, K.; He, X.; Zhao, X. J.; Drake, T.; Wang, L.; Bagwe, R. P. Bionanotechnology based on silica nanoparticles. *Medicinal research reviews* **2004**, *24*, 621–38.

(23) Wan, Y.; Zhao, D. On the controllable soft-templating approach to mesoporous silicates. *Chemical reviews* **2007**, *107*, 2821–60.

(24) Vallet-Regi, M.; Ramila, A. A new property of MCM-41: drug delivery system. *Chemistry of Materials* **2001**, *13*, 308–311.

(25) Suteewong, T.; Sai, H.; Lee, J.; Bradbury, M.; Hyeon, T.; Gruner, S. M.; Wiesner, U. Ordered mesoporous silica nanoparticles with and without embedded iron oxide nanoparticles: structure evolution during synthesis. *Journal of Materials Chemistry* **2010**, *20*, 7807.

(26) Suteewong, T.; Sai, H.; Cohen, R.; Wang, S.; Bradbury, M.; Baird, B.; Gruner, S. M.; Wiesner, U. Highly aminated mesoporous silica nanoparticles with cubic pore structure. *Journal of the American Chemical Society* **2011**, *133*, 172–5.

(27) Van Blaaderen, A.; Vrij, A. Synthesis and characterization of colloidal dispersions of fluorescent, monodisperse silica spheres. *Langmuir* **1992**, *8*, 2921–2931.

(28) Ow, H.; Larson, D. R.; Srivastava, M.; Baird, B. a; Webb, W. W.; Wiesner, U. Bright and stable core-shell fluorescent silica nanoparticles. *Nano letters* **2005**, *5*, 113–7.

(29) Larson, D. R.; Ow, H.; Vishwasrao, H. D.; Heikal, A. a.; Wiesner, U.; Webb, W. W. Silica Nanoparticle Architecture Determines Radiative Properties of Encapsulated Fluorophores. *Chemistry of Materials* **2008**, *20*, 2677–2684.

(30) De Rosa, S. C.; Herzenberg, L. a; Roederer, M. 11-color, 13-parameter flow cytometry: identification of human naive T cells by phenotype, function, and T-cell receptor diversity. *Nature medicine* **2001**, *7*, 245–8.

(31) Perfetto, S. P.; Chattopadhyay, P. K.; Roederer, M. Seventeen-colour flow cytometry: unravelling the immune system. *Nature reviews. Immunology* **2004**, *4*, 648–55.

(32) Mattanovich, D.; Borth, N. Applications of cell sorting in biotechnology. *Microbial cell factories* **2006**, *5*, 12.

(33) Herzenberg, L. a; Parks, D.; Sahaf, B.; Perez, O.; Roederer, M.; Herzenberg, L. a The history and future of the fluorescence activated cell sorter and flow cytometry: a view from Stanford. *Clinical chemistry* **2002**, *48*, 1819–27.

(34) Fulton, R. J.; McDade, R. L.; Smith, P. L.; Kienker, L. J.; Kettman, J. R. Advanced multiplexed analysis with the FlowMetrix system. *Clinical chemistry* **1997**, *43*, 1749–56.

(35) Han, M.; Gao, X.; Su, J. Z.; Nie, S. Quantum-dot-tagged microbeads for multiplexed optical coding of biomolecules. *Nature biotechnology* **2001**, *19*, 631–5.

(36) Trau, M.; Battersby, B. J. Novel Colloidal Materials for High-Throughput Screening Applications in Drug Discovery and Genomics. *Advanced Materials* **2001**, *13*, 975–979.

(37) Chan, W. C. W.; Maxwell, D. J.; Gao, X.; Bailey, R. E.; Han, M.; Nie, S. Luminescent quantum dots for multiplexed biological detection and imaging. *Current opinion in biotechnology* **2002**, *13*, 40–6.

(38) Wang, D.; Rogach, A. L.; Caruso, F. Semiconductor Quantum Dot-Labeled Microsphere Bioconjugates Prepared by Stepwise Self-Assembly. *Nano Letters* **2002**, *2*, 857–861.

(39) Wang, L.; Tan, W. Multicolor FRET silica nanoparticles by single wavelength excitation. *Nano letters* **2006**, *6*, 84–8.

(40) Li, Y.; Cu, Y. T. H.; Luo, D. Multiplexed detection of pathogen DNA with DNA-based fluorescence nanobarcodes. *Nature biotechnology* **2005**, *23*, 885–9.

(41) Wu, W.-B.; Wang, M.-L.; Sun, Y.-M.; Huang, W.; Cui, Y.-P.; Xu, C.-X. Color-tuned FRET polystyrene microspheres by single wavelength excitation. *Optical Materials* **2008**, *30*, 1803–1809.

(42) Marcon, L.; Spriet, C.; Meehan, T. D.; Battersby, B. J.; Lawrie, G. a; Héliot, L.; Trau, M. Synthesis and application of FRET nanoparticles in the profiling of a protease. *Small (Weinheim an der Bergstrasse, Germany)* **2009**, *5*, 2053–6.

(43) Xu, J.; Liang, J.; Li, J.; Yang, W. Multicolor dye-doped silica nanoparticles independent of FRET. *Langmuir : the ACS journal of surfaces and colloids* **2010**, *26*, 15722–5.

(44) Ehlert, O.; Thomann, R.; Darbandi, M.; Nann, T. A four-color colloidal multiplexing nanoparticle system. *ACS nano* **2008**, *2*, 120–4.

(45) Schulte-Ladbeck, R.; Kolla, P.; Karst, U. Trace analysis of peroxide-based explosives. *Analytical chemistry* **2003**, *75*, 731–5.

(46) Lim, S. D.; Sun, C.; Lambeth, J. D.; Marshall, F.; Amin, M.; Chung, L.; Petros, J. a; Arnold, R. S. Increased Nox1 and hydrogen peroxide in prostate cancer. *The Prostate* **2005**, *62*, 200–7.

(47) Chang, M. C. Y.; Pralle, A.; Isacoff, E. Y.; Chang, C. J. A selective, cell-permeable optical probe for hydrogen peroxide in living cells. *Journal of the American Chemical Society* **2004**, *126*, 15392–3.

(48) Miller, E. W.; Albers, A. E.; Pralle, A.; Isacoff, E. Y.; Chang, C. J. Boronate-based fluorescent probes for imaging cellular hydrogen peroxide. *Journal of the American Chemical Society* **2005**, *127*, 16652–9.

(49) Albers, A. E.; Okreglak, V. S.; Chang, C. J. A FRET-based approach to ratiometric fluorescence detection of hydrogen peroxide. *Journal of the American Chemical Society* **2006**, *128*, 9640–1.

(50) Rauhut, M. Chemiluminescence from concerted peroxide decomposition reactions. *Accounts of Chemical Research* **1969**, *2*, 80–87.

(51) Chandross, E. A new chemiluminescent system. *Tetrahedron Letters* **1963**, 761–765.

(52) Lee, D.; Khaja, S.; Velasquez-Castano, J. C.; Dasari, M.; Sun, C.; Petros, J.; Taylor, W. R.; Murthy, N. In vivo imaging of hydrogen peroxide with chemiluminescent nanoparticles. *Nature materials* **2007**, *6*, 765–9.

(53) Lee, D.; Erigala, V. R.; Dasari, M.; Yu, J.; Dickson, R. M.; Murthy, N. Detection of hydrogen peroxide with chemiluminescent micelles. *International journal of nanomedicine* **2008**, *3*, 471–6.

(54) Dasari, M.; Lee, D.; Erigala, V. R.; Murthy, N. Chemiluminescent PEG-PCL micelles for imaging hydrogen peroxide. *Journal of Biomedical Materials Research Part A* **2009**, *89A*, 561–566.

(55) Lim, C.-K.; Lee, Y.-D.; Na, J.; Oh, J. M.; Her, S.; Kim, K.; Choi, K.; Kim, S.; Kwon, I. C. Chemiluminescence-Generating Nanoreactor Formulation for Near-Infrared Imaging of Hydrogen Peroxide and Glucose Level in vivo. *Advanced Functional Materials* **2010**, *20*, 2644–2648.

(56) Iyer, S. K.; Sarakune, K.; Johnson, K.; Huettner, S.; Wiesner, U. B. Synthesis of Bright Dye Incorporated Silica Nanoparticles as Chemicluminescent Probes for Hydrogen Peroxide Sensing. *in preparation*.

CHAPTER 2

Multicolor Fluorescent Core-Shell Silica Nanoparticles for Multiplexed and Multicolor Intra-cellular Imaging *

2.0 Abstract

Bright multicolor fluorescent silica nanoparticles with surface PEG coatings were synthesized to sizes below 100 nm to facilitate cellular uptake and encapsulating three spectrally distinct dyes based on RGB color mixing scheme at three intensity levels. The particle architecture was designed to precisely control the number of dyes per color and to minimize energy transfer between dyes for maximum brightness, resulting in twenty-six distinguishable particles based on wavelength and fluorescence intensity. Individual particles have onion-type structures with up to twenty-four distinct layers around a dyed core. High level of precision in dye encapsulation was enabled by a combination of fluorescence correlation spectroscopy (FCS) and steady-state optical spectroscopy. As a proof of concept these particles were taken up by cells to demonstrate fluorescence multiplexing capabilities. We expect this multicolor nanoparticle platform to open new avenues towards intracellular bioimaging, high throughput screening and medical diagnostic applications.

* Prepared for submission as: Srikant K Iyer, Teresa Kao, Marcus Wilkes, Roy Cohen, Ulrich Wiesner, Barbara Baird. "Multicolor Fluorescent Core-Shell Silica Nanoparticles for Multiplexed and Multicolor Intra-cellular Imaging"

2.1 Introduction

Drug discovery, drug screening, gene expression, and identification of proteins as vaccine targets are based on carrying out high throughput screening (HTS) assays involving large numbers of molecules. This requires screening large chemical libraries for particular target molecules such as proteins, antibodies, nucleotides or peptides.[1,2,3,4] Screening large libraries or biological multiplexing accelerates the development of tools for therapeutic and diagnostic applications. Biological multiplexing involves conducting multiple assays simultaneously without compromising on sensitivity and specificity. Advancement towards miniaturized HTS has led towards screening over thousands of compounds a day. Top to bottom two dimensional array fabrication technology has led to development of DNA chips, microarrays and bioMEMS.[2,3,5] Positional encoding based pattern recognition has further helped identifying specific molecular finger prints. Some of the major drawbacks with these technologies are that they are expensive in terms of equipment set-up and reagents and complex in terms of sample preparation and array fabrication. Furthermore, variability in measurements due to cross-reactivity and reproducibility has made these methodologies difficult for large scale analysis.[6,7]

Miniaturization has led to designing and synthesizing micro and nanomaterials often in the form of particles that act as carriers and labels for molecules with built-in codes for identification.[4,8] Each distinguishable particle is analogous to a single well or array in the 2-D array technology. Hence multiplexing is not restricted to the number of wells or arrays, but the number of distinguishable particles.[9,10,11] It has been demonstrated that particles with sizes below 100 nm are particularly suited for cellular

uptake, and thus are desirable for intracellular imaging applications.[12–16] In this report we thus focus our attention on developing bright and optically encoded fluorescent core-shell silica nanoparticles referred to as *multicolor* Cornell dots or simply *mc*C dots with sizes below 100 nm for high throughput screening and applying them to intracellular bioimaging using fluorescence multiplexing. These nanoparticles are encoded with three spectrally distinct organic fluorophores, i.e. N-(7-dimethylamino-4-methylcoumarin-3-yl)maleimide *(DACm,* λ_{abs} = 395 nm, λ_{em} = 450 nm), tetramethylrhodamine-5-maleimide (TMRm , λ_{abs} = 540 nm, λ_{em} = 570 nm) and Cy5-maleimide (Cy5m, λ_{abs} = 640 nm, λ_{em} = 670 nm), with three precisely controlled numbers of dyes, i.e. 0, 5 and 20, respectively, per particle, resulting in 26 optically distinguishable nanoparticles as shown in Figure 2.1. The dyes were chosen based on commonly available excitation laser sources (λ_{exc} = 405 nm, 540 nm and 633 nm) used in confocal microscopy or in high throughput screening techniques like flow cytometry, thus rendering *mc*C dots useful for standard fluorescence instrumentation. The particle architecture is designed such that the dyes are added to a dye doped particle core in a layer-by-layer fashion and each spectrally distinct dye is spatially separated by a pure silica shell in order to reduce energy transfer between the dyes (Figure 2.1). This assures maximum brightness levels and thus maximum signal-to-noise ratios in imaging.

In addition to providing distinct fluorescent signatures for identification, development of optically encoded fluorescent particles for screening assays requires choosing a material that can be easily surface modified with biomolecular probes such as oligonucleotides or peptides. The versatility of silica surface chemistry makes it an

appropriate choice. The number of fluorescent optical codes 'C' that can be generated from silica based *mc*C dots depends on two parameters, the number of dye colors, 'm', and the number of fluorescence intensity levels, 'N', associated with each color. For intensity levels ranging from 0 to infinity the number of codes is defined as $C = N^m - 1$.[17] The present case of three intensity levels, N = 3, of three colors, m = 3, thus leads to 26 color codes. The potential of multiplex coding using color rationing based bead technology has been explored by other researchers. Fulton *et al.* used two organic dyes to encode a 5.5 μm polystyrene bead at 8 different intensity levels for multiplexed assays.[18] Nie *et al.*, synthesized 1.2 μm polystyrene beads encoded with six spectrally distinguishable CdSe/ZnS core-shell quantum dot nanoparticles at six different intensity levels in different ratios by swelling the polymer in an appropriate solvent mixture.[17] The fluorescent species in the above cases were all physically incorporated into micron sized polystyrene particles and because of their large size could not easily be applied for multiplexed *in-vivo* or intracellular bioimaging. Luo *et al.* developed dendrimer like DNA (DL-DNA) based fluorescent nanobarcodes by precisely tagging the DL-DNA with two organic fluorophores in different ratios based on the number of available reactive sites.[19] In order to amplify the fluorescence signal from these nanobarcodes, again microbeads were used as support for imaging and molecular detection. Similarly, Tan *et al.* synthesized 70 nm Förster resonance energy transfer (FRET) based silica nanoparticles encoding dyes with different dye ratios and loaded them on 10 μm streptavidin coated microspheres.[20] Trau *et al.* extended the work and applied it to optical encoding in combinatorial chemistry by developing > 100 nm (FRET) based silica particles encoding dyes with different dye ratios that were then

loaded onto 10 μm polystyrene microspheres as substrates for multiplexing.[21] The dye ratios encoded in these FRET based particles were quantified based on the dyes dosed into the reaction mixture and assuming all dyes were incorporated. Because of the large sizes of the final beads (> 1 μm) in none of these cases was intracellular imaging demonstrated.

2.2 Multicolor Particle Design and Synthesis

In order to carry out the synthesis of *mc*C dots three key issues had to be addressed: (1) identification of the appropriate fluorescent dyes, 'm', based on commonly available excitation laser line sources; (2) identification of the appropriate numbers of dyes that can be reproducibly incorporated into the particles in order to generate distinguishable fluorescence intensity levels, 'N', and (3) spatial separation of the spectrally distinct dyes within the particle to minimize energy transfer and hence fluorescence quenching in order to achieve maximum brightness levels. The three dyes chosen for developing *mc*C dots were DACm, TMRm and Cy5m, *vide supra*. The fluorescence intensity measured for a single particle and single color depends on the number of dyes incorporated in it.[22] Assuming that in a typical *mc*C dots synthesis batch the number of dyes of a specific color is Poisson distributed (thus assuming that dye encapsulation is a purely stochastic process), in order to distinguish different intensity levels of different *mc*C dots the mean values of these Poisson distributions were chosen such that there is minimum overlap between the wings of the distributions (see Figure 2.2a). It is thus desirable to precisely control the dye incorporation in the particle and to have minimum energy transfer between dyes on increasing their encapsulation numbers in order to avoid fluorescence quenching. For

a given core size on increasing the number of dye molecules, based on spatial proximity dyes tend to show energy transfer.[23] Hence to minimize cross talk between the dyes here a layer-by-layer approach was used to construct particles with high dye encapsulation numbers. Previous C dots synthesis work revealed that 20-30 nm diameter core-shell silica nanoparticles typically incorporated about 5-7 dyes per particle core for a given dye concentration.[24] Assuming dye incorporation is Poisson distributed, for particles with mean dye numbers per particle of 10 and 15, respectively, an overlap of ~ 45% and ~ 25%, respectively, with 5 dyes per particle batches are expected as shown in Figure 2.2a. In contrast particles with a mean number of 20 dyes per particle only show ~ 3% overlap with a 5 dyes per particle batch. A similarly small overlap is expected for the Poisson distribution of a 5 dyes per particle batch with a particle batch that contains zero dyes of that color (Figure 2.2a). Based on these considerations we chose the three distinct levels of 0, 5, and 20 dyes per particles, respectively, to distinguish different intensity levels of the same color in *mc*C dots.

Figure 2.2b-i shows a schematic of the various layer-by-layer particle synthesis routes leading to the 26 distinct *mc*C dots. The notation we have adopted in the following to distinguish *mc*C dot color codes contains lower case letters to denote fluorescence intensity levels (m/h for medium/high, i.e. ~5/20 dyes per particle) and capital letters to denote fluorescence colors (G/R/B for green/red/blue emission, respectively). Each sequence moves from the core to the outer shell. For example, a mGhRmB *mc*C dot has a medium green (~5 dyes) core, followed by a high red (~20 dyes) inner shell, followed by a medium blue (~5 dyes) outer shell. A color not present

(i.e. zero dyes of that color) in a *mc*C dot is denoted simply by omitting its notation. For example, a hGhB *mc*C dot has a high green (~20 dyes) core, no red (i.e. zero red dyes), and a high blue (~20 dyes) outer shell. Particle synthesis was carried out (see Appendix A for details) by first conjugating commercially available maleimide activated dye (TMRm, Cy5m, or DACm) to 3-mercaptopropyl-trimethoxysilane (MPTMS) using the maleimide-thiol bioconjugation reaction to form dye conjugate (Figure 2.2b).[25] Three single color particles containing medium dye loadings (mG, mR, or mB, respectively, see Figure 2.2c-e) were first synthesized via a modified Stöber-type silica condensation, by co-condensing the dye conjugate with TEOS at appropriate ammonia and water concentrations in alcohol.[26] To this a thin silica shell was added by dosing the reaction solution with TEOS at concentrations below the nucleation threshold to avoid any secondary nucleation.[27,28] A specific volume was removed from each reaction solution and these particles were set aside as particles with medium dye loadings. In order to get to the three single color particles with high dye loadings (hG, hR, or hB, respectively, see Figure 2.2c-e), to the remainder of the reaction solutions, dye conjugate was added to co-condense with the silanol groups on the surface of the core-shell silica nanoparticles. Following this step a thin silica shell was again added as described above. This alternating dye layer-silica shell procedure was carried out until the appropriate high dye loading with ~ 20 dyes per particle was obtained. Figure 2.2c-e shows a schematic of the resulting onion-like structures for high green (TMRm), high red (Cy5m) and high blue (DACm) single color C dot particles. The necessary numbers of additional dye and silica shell layers on the core

per particle to achieve high intensity emission were four for high green (TMRm) and high blue (DACm), and three for high red (Cy5m) particles.

Following the development of synthesis protocols to precisely control the number of dyes per particle for the three distinct dye systems we carefully devised particle architectures to incorporate all three dyes in the same particle with different dye loading levels for each dye. These particles were synthesized such that the three dyes were added in a layer-by-layer fashion with TMRm dye (green) in the core followed by Cy5m dye conjugate (red) in an inner shell followed by DACm dye conjugate (blue) added as the final dye layer (see center particle in Figure 2.1a). Organic fluorophores have relatively broad absorption and emission spectra. Depending on the spectral and spatial proximity of the various dyes in our particles, Förster resonance energy transfer is expected to occur.[29] Such non-radiative energy transfer is the result of spectral overlap between the emission of a donor dye with the absorption spectrum of an acceptor dye. The efficiency of energy transfer between two dyes is determined by the Förster radius which is the distance at which 50% efficient energy transfer occurs between the donor and the acceptor.[29] The calculated Förster radius for the pair DACm-TMRm is ~ 40 Å (4.0 nm), while that of the pair TMRm-Cy5m is ~ 45 Å (4.5 nm). Since DACm and Cy5m are on the extreme ends of the visible spectrum, with 15 Å (1.5 nm) the Förster radius of this pair is the smallest. The efficiency of energy transfer drops dramatically, as $1/r^6$, with separation distance, r, between the donor and the acceptor molecules.[29] In order to effectively suppress energy transfer the TMRm and Cy5m dye layers in our particles were separated by a 10-12 nm thick silica shell (e.g. see Figure 2.2f). For particles containing no Cy5m

dye, a silica shell thickness of 10-12 nm was grown on TMRm containing particle cores prior to DACm dye addition (e.g. see Figure 2.2g). For the first DACm dye layer addition to particles containing TMRm and Cy5m layers, a pure silica shell of 6-8 nm thickness was first grown (e.g. see Figure 2.2i). Hence, dye layers of different colors were spatially separated by thick enough silica shells to expect effective suppression of energy transfer.

Since TMRm was the dye chosen to be in the center, to maintain consistency in the synthesis of different *mc*C dots, a large batch of medium and high dye loaded TMRm particles were synthesized. The next step to obtain dual-color C dots was to grow a 10-12 nm thick silica separation shell on these nanoparticles followed by the addition of Cy5m dye conjugate (Figure 2.2f). After adding a final silica shell, this accounted for particles with medium Cy5m (mR) dye loadings. Following this step, two additional Cy5m dye layers plus their silica shells were added to obtain high Cy5m (hR) dye loaded particles. Please note that the reduction in additional layers to reach high dye loadings in larger *multicolor* C dots is due to their increased size relative to single color C dots providing more surface area per particle for additional dye attachment. Syntheses following these protocols provided the following four dual-color C dots with zero DACm dyes per particle: mGmR, mGhR, hGmR and hGhR. In order to obtain dual-color particles with zero Cy5m dyes per particle, DACm dye conjugate was added to mG and hG particles with a silica separation layer of 10-12 nm thickness to separate the TMRm and DACm dye layers (Figure 2.2g). This accounted for particles with medium DACm (mB) dye loadings. Three additional DACm dye layers and their silica shells were added to mGmB and hGmB particles in order to

obtain high DACm (hB) dye loadings. Syntheses following these protocols provided the following four dual-color C dots with zero DACm dyes per particle: mGmB, mGhB, hGmB and hGhB.

Dual-color C dots with zero TMRm dyes per particle were synthesized using Cy5m core-shell particles as the template (Figure 2.2h). To that end a large batch of medium Cy5m doped particles was synthesized which was split into two portions, leaving one batch as particles with medium Cy5m (mR) dye loading, while to the other batch three alternating Cy5m dye and silica shell layers were added to obtain high Cy5m (hR) dye loaded particles (Figure 2.2d). A silica separation shell of 6-8 nm thickness was grown on these mR/hR nanoparticles followed by the addition of DACm dye conjugate (Figure 2.2h). Together with a final silica shell this accounted for particles with medium DACm (mB) dye loadings. Three alternating DACm dye and silica shell layers were subsequently added to obtain high DACm (hB) dye loadings. Syntheses following these protocols provided the final four dual-color C dots with zero TMRm dyes per particle: mRmB, mRhB, hRmB and hRhB.

Finally, in order to obtain triple color particles with all three dyes incorporated, a 6-8 nm thick silica shell was grown on mGmR, mGhR, hGmR and hGhR particles, followed by the addition of a DACm dye layer with silica shell. To the resulting mGmRmB, mGhRmB, hGmRmB and hGhRmB particles three additional DACm dye and silica shell layers were added to obtain high dye doped DACm (hB) particles (Figure 2.2i). Syntheses following these protocols provided the following eight triple color *mc*C dots: mGmRmB, hGmRmB, mGhRmB, hGhRmB, mGmRhB, hGmRhB, mGhRhB and hGhRhB.

The ability to precisely tune the dye numbers in such multicolor fluorescent silica nanoparticles comes with a considerable amount of architectural complexity. For example, triple color C dots with high dye loadings for TMRm, Cy5m and DACm (hGhRhB) contain four TMRm dye and four silica shell layers added to the medium TMRm dye loaded core-shell particle (adding up to nine layers around the TMRm core), followed by three dye and three silica shell layers to obtain the high Cy5m dye loading, followed by four dye and four silica shell layers to obtain the high DACm dye loading. All particles were finally surface coated with a polyethylene glycol (PEG) layer (see Appendix A for details) to provide steric stabilization in buffer solutions and to render them more biocompatible. The result is onion-type architecture with 24 distinct layers (including the PEG layer) around a dyed core, of which 11 are dye layers and 12 are pure silica shell layers. Based on the various dye per particle combinations 26 spectroscopically distinguishable particles were synthesized as shown in Figure 2.1. Figure 2.1a displays color renderings of these 26 particles assembled in a way reflecting the synthesis pathways described above. Figure 2.1b depicts a photo of the 26 particles in aqueous solutions in cuvettes under ambient light. Cuvettes are organized according to green TMRm dye loadings, with particles containing no, medium, and high TMRm dye loadings sitting in the bottom, middle, and upper rows, respectively (see Figure 2.4b for specific assignments). Please note that for comparison the 27^{th} cuvette on the bottom left of Figure 2.1b is filled with non-dyed PEGylated silica nanoparticles.

2.3 Particle Characterization and Discussion

All resulting particles were PEGylated using 5k molar mass poly(ethylene glycol)-silane before carrying out any spectroscopic measurements (see Appendix A). Since a description of the full spectroscopic characterization of all 26 particle species is beyond the scope of this paper, here only representative examples for specific *mc*C dots are provided, together with a summary of the spectroscopic measurements of brightness levels of all colors in all 26 particles, see Figures 3 and 4. In order to characterize the nanoparticles and understand their fluorescent properties, first aqueous solutions of the medium and high DACm, TMRm, and Cy5m dye loaded single color nanoparticles were absorbance matched to those of the respective parent free dyes. Figure 2.3a-c shows the resulting absorbance and emission spectra. No significant spectral shifts between free dyes and particles were observed, suggesting that the electronic structure of the dyes were preserved upon encapsulation. The medium and high DACm, TMRm and Cy5m dye doped nanoparticles show an enhancement of ~ 6.0, ~1.3, and ~1.5, respectively, relative to free dye. For all three systems dye encapsulation into the rigid silica environment thus leads to significant brightness enhancements relative to free dye in aqueous solution, consistent with earlier studies and suggesting that under these conditions the dyes don't exhibit fluorescence quenching even at the high loading levels demonstrated here.[24,27]

The number of dyes incorporated into the particles was quantified using fluorescence correlation spectroscopy (FCS) in combination with absorbance measurements.[24] The FCS experimental set up was equipped to excite dyes at λ = 405nm, 543 nm and 633 nm, respectively (see Appendix A). FCS is a diffusion based

spectroscopy technique using the fluorescence of the diffusing moiety to generate an autocorrelation curve. Similar to dynamic light scattering (DLS), the time scale on which the correlation decays can be related to a diffusion coefficient which in turn can be related to a hydrodynamic radius/diameter of the diffusing moiety.[24] Figure 2.3d-f compares the autocorrelation curves of the three parent dyes (solid lines) with those of the six single color C dots (mG, mR, and mB, open symbols; hG, hR, and hB, closed symbols) derived from the three dyes/colors at medium and high dye loadings, respectively. Dye incorporated nanoparticles diffuse much slower than the parent free dyes, confirming a significant increase in hydrodynamic radius from free dye to particle. Furthermore, medium and high dye level containing particles show very similar correlation curves revealing the high control over the final targeted particle size. Analysis of the autocorrelation curves for the DACm, TMRm and Cy5m systems reveals diameters of 1.3 nm, 1.4 nm and 1.4 nm, respectively, for the free dyes, as well as 40 nm, 45 nm and 35 nm, respectively, for both medium and high dye loaded nanoparticles.

From the amplitude, G(0), of the FCS autocorrelation curve one can obtain the number of fluorescent moieties in the focal volume from which their concentration can be deduced.[24] Using this particle concentration along with the concentration of dyes obtained from the absorbance measurements one can calculate the number of dyes per particle. This is a key piece of information which allowed quantitative assessments of dyes per particle numbers in the synthesis of *multicolor* C dots (*mc*C dots) and was used as feedback to optimize synthesis protocols to achieve the necessary levels of control described herein. Based on these measurements we calculated the number of

dyes per particle for medium and high dye loaded particles to be 6/27, 6/22 and 6/24 for TMRm, Cy5m and DACm dye loadings. Furthermore, from the product of the fluorescence enhancement of a dye encapsulated in the particle over free dye in aqueous solution and the number of dyes per particle, a brightness factor for each dye-particle system can be calculated. This factor describes how much brighter the particles are relative to a single free dye in aqueous solution.[24] The respective brightness factors determined in this way were: 9.1/35 for the medium/high TMRm particles, 9/33 for the medium/high Cy5m particles, and 36/144 for the medium/high DACm particles. These results suggest that the particles should be one to two orders of magnitude brighter than the parent free dyes. Besides their multiplexing properties, these very high brightness levels will make *mc*C dots very attractive for bioimaging applications. The calculated brightness factors can be compared to the experimental brightness of the dyes and particles as measured by the count rates of the individual diffusing species on the optical FCS detector. This provides a direct measure of the brightness of the free dyes and particles, respectively. Figure 2.3g-i show the results of these measurements. Figure 2.3g shows that medium/high TMRm loaded particles are 6.6 (± 0.1)/32 (± 0.4) times brighter than parent TMRm free dye, while for the Cy5m system, Figure 2.3h shows that medium/high Cy5m loaded particles are 5.3 (± 0.2)/27.6 (± 0.4) times brighter than the parent Cy5m free dye. Figure 2.3i compares the brightness for the DACm particle system and shows medium/high DACm loaded particles to be 24 (± 3.0)/105 (± 10) times brighter than parent DACm free dye, respectively. These direct brightness measurements confirm that as targeted, individual brightness levels are apart from one another by a factor of 4-6. Consistent

with similar observations in earlier studies, the calculated brightness factors systematically overestimate the values obtained from FCS measurements.[24] This may be due to an error in the determination of dye equivalents, which e.g. assumed no change in absorption cross section between free and encapsulated dyes. It may further be due to the fact that FCS measurements were carried out with polarized light, which possibly only excited sub-sets of the dyes in the particles, in turn leading to smaller counts per particle than expected from the brightness factor.

Previous work by Trau *et al.* on fluorescent multi-shell nanoparticles with sizes > 3 μm revealed that the fluorescence intensity of the particles decreased on increasing the number of shell layers, due to changes in refractive index causing scattering of the emitted light.[30] We checked whether the same effect applied to the present particles by comparing the ratios of the number of dyes per particle to the brightness per particle for medium and high dye loaded particles. Our results showed that for medium and high DACm loaded particles the ratio was 4.0/4.3, for medium and high TMRm loaded particles the ratio was 4.5/4.8, and for medium and high Cy5m loaded particles the ratio was 3.66/3.69. These results reveal that in contrast to the results of Trau *et al.* in our system moving from medium to high dye loadings by incorporating additional silica shells does not decrease the relative fluorescence emission.

Figure 2.4a shows representative FCS curves of specific particles moving towards triple color *mc*C dots covering the entire synthetic scheme starting from medium/high TMRm dye loaded single color C dots (mG, hollow circles/hG, full circles) via medium/high Cy5m dye loaded dual-color C dots (hGmR, hollow circles/hGhR, full circles) to the final triple color *mc*C dots with medium/high DACm

dye loadings (hGhRmB, hollow circles/hGhRhB, full circles). Please note that all particles in this plot were terminated using a PEGylation step, although they were not grown to the same size of ~ 85 nm. Results clearly indicate the increase in the particle size as reflected in a shift of the correlation curves to longer times on starting from medium TMRm dye loaded particles to particles that contain all three dyes at high dye loadings. FCS curves of green fluorescent particles show pronounced contributions from triplet states at short times, which was accounted for by the fitting procedure (see Appendix A). Medium TMRm loaded core shell particle synthesis (mG, hollow green circles), resulted in particles of 15 nm (± 0.5) diameter (including the PEG layer). Addition of four TMRm dye and silica shell layers resulted in 28 nm (± 0.6) diameter (including the PEG layer) high TMRm dye loaded particles (hG, solid green circles). Each of the four alternating dye and silica shell layers contributed 1.2-1.5 nm to the shell thickness (or 2.4-3 nm to the particle diameter). Dual-color particles with medium Cy5m dye loading first had a 10-12 nm thick silica shell (increasing the particle diameter by 20-24 nm) grafted onto the 28 nm diameter hG particles followed by the addition of one alternating Cy5m dye and silica shell layer (hGmR, hollow red circles). Comparison of the autocorrelation curves for hG and hGmR particles reveals a large difference in particle size as the hGmR curve is shifted significantly to the right of the hG curve. Analysis reveals a diameter of 53 nm (± 2.0) for the dual-color C dots. Particles with high Cy5m dye loading with two additional alternating Cy5m dye and silica shell layers on the hGmR particle resulted in 57 nm (± 2.2) diameter dual-color C dots (hGhR, solid red circles). Each additional Cy5m dye and silica shell layer increased the thickness of the particle by ~ 1.0-1.1 nm (increasing the particle

diameter by 2.0-2.2 nm). Finally, particles containing the third, DACm dye had a 6-8 nm thick silica separator shell (increasing the particle diameter by 12-16 nm) grown onto the 57 nm (± 2.2) hGhR particles followed by the addition of a single alternating DACm dye and silica shell layer, producing triple color C dots (hGhRmB, hollow blue circles) with a particle diameter of ~ 72 nm (± 4.1). The increase in the particle size is noticeable when comparing the FCS curves of hGhR and hGhRmB. The final FCS curve in Figure 2.4a is from triple color C dots with high loadings of all three dyes (hGhRhB, solid blue circles) with three additional alternating DACm dye and silica shell layers plus a PEG surface layer, added to the hGhRmB particles resulting in a final particle diameter of 85 nm (± 4.6).

The absence of significant energy transfer between dyes of different color in the same particle, i.e. the efficiency of the pure silica layer to suppress Förster resonance energy transfer (FRET), is highlighted in Figure 2.4b showing six fluorescence emission spectra of solutions of four particles (hGhRhB, hGhRmB, mGhRhB and hGmRhB) each containing all three dyes/colors. For the spectra on the left and right (blue and red emission, respectively,) solutions were absorbance matched in the green, while for the spectra in the middle (green emission) solutions were absorbance matched in the red. Figure 2.4b compares emission profiles from excitations at 405 nm, 540 nm, and 633 nm, respectively, of medium and high DACm (mB/hB), TMRm (mG/hG), and Cy5m (mR/hR) containing triple color particles. Particles with high DACm dye loading (hGhRhB) were ~3.8 times brighter than with medium DACm loading (hGhRmB) when excited at 405 nm. Particles with high TMRm dye loading (hGhRhB) were ~3.5 times brighter than with medium TMRm

loading (mGhRhB) when excited at 540 nm. On excitation at 633 nm, particles with high Cy5m loading (hGhRhB) were ~4.0 times brighter than with medium loading (hGmRhB). The very different emission levels confirm that particles containing medium and high dye loading for each color can clearly be spectroscopically differentiated. Furthermore, none of the spectra with blue or green emission show spectroscopic evidence for FRET. For example, on exciting samples hGhRmB or hGhRhB at 405 nm (in the blue) no significant energy transfer from DACm to TMRm or Cy5m is evident via green or red emission, respectively. Similarly, when exciting hGhRhB or mGhRhB particles at 540 nm, no significant energy transfer from TMRm to Cy5m is observed via red emission. We conclude that the thick silica shells used to spatially separate layers of different color dyes clearly suppress FRET that would otherwise be observed in the spectra.

Figure 2.4c summarizes the spectroscopic brightness levels of all colors in all 26 particles in the form of bar graphs positioned in the identical way to the cuvettes in Figure 2.1b filled with particle solutions. Brightness levels were measured as the respective fluorescence emission maxima for each color of each particle as exemplified in Figure 2.4b. The height of the bars for each color was normalized to the brightness of particles with medium dye loading. On going from top to bottom, in analogy to the photo in Figure 2.1b, we have separated the display into three families/rows with decreasing number of green TMRm dyes (green bars) with ~20 (top row), ~5 (middle row), and 0 dyes (bottom row) per particle in the core of the particles. From these bar graphs, the particles with high TMRm dye loading were ~ 3.5 times brighter than the medium dye loaded TMRm particles. On going across the

figure from left to right we compare the fluorescence brightness levels in each of these "green" families/rows for particles containing different amounts of Cy5m (red bars) and DACm dyes (blue bars). From the results, as targeted in the design (*vide supra*) particles with high Cy5m dye loading were ~ 4-4.3 times brighter than particles containing medium Cy5m dye levels, whereas the high DACm loaded particles were about ~ 3.8-4.2 times brighter than the medium DACm loaded particles. Measured particle brightness levels as revealed in Figure 2.4c for the three colors of *mc*C dots are thus solely due to the number of dyes of that color in the particle. This allows predictions of brightness levels based on synthesis protocols and renders identification of specific color codes more manageable.

2.4 Biological Multiplexing in Cell Assemblies

Following the characterization of *mc*C dots, fluorescence multiplexing was carried out to demonstrate multicolor intra-cellular imaging. Individual cell solutions were electroporated with one type of particle solution (see Appendix A), following this the cells were mixed and differentiated based on the RGB color mixing scheme using confocal imaging. Rat basophilic leukemia mast cells (RBL-2H3) were used for these measurements and the cell surface was labeled with Alexa488-Cholera toxin subunit B (λ_{abs} = 488 nm, λ_{em} = 515 nm, a wavelength not utilized in *mc*C dot syntheses) to identify the cell periphery.

Representative nanoparticles were used as a proof of concept to demonstrate cellular uptake of nanoparticles. Figure 2.5 shows confocal fluorescence microscopy images of mixture of cells, containing hB, hGhB, hGhR and hGhRmB particles, respectively. Figure 2.5 (a-d) show cell images as obtained in green, red, blue and

yellow channels, upon exciting the cells at 560 nm, 633 nm, 405 nm and 488 nm, respectively. These images show emission for each color channel corresponding to photons emitted from each dye color present in the nanoparticle. RBL-2H3 cells show autofluorescence in the green (Figure 2.5a) and blue (Figure 2.5b) channel, however since the particles are bright, the high signal to noise ratio makes it possible to identify nanoparticles internalized in cells. Figure 2.5e, shows the overlaid image of the four channels, where cells labeled with hB particles (blue circles) show emission only in the blue channel, with no emission in green or red channel, whereas cells labeled with hGhRmB (magenta circle) show emission in red, green and blue channels. Cells containing dual color particles, hGhB (yellow circle) and hGhR (red circle) show no contribution in the red and blue channels, respectively. Figure 2.5f shows the bright-field image of the cells showing that the morphology of these RBL-2H3 cells were intact after electroporation, thus making it possible to carry out cell imaging. Based on this figure we show that the *mc*C dots are internalized and from co-localizing the emission contribution from each channel, the nanoparticle stained cells can be distinguished from each other. These initial experiments show the potential for *mc*C dots as intracellular fluorescent markers for multiplexing applications and differentiating cells.

2.5 Conclusion and Outlook

This is the first demonstration of intracellular fluorescence multiplexing utilizing multicolor silica nanoparticles. These bright *mc*C dots provide a platform to differentiate targets based on the simple RGB color code. This platform can be further expanded by adding an additional dye color that is spectrally distinct, thus

geometrically increasing the number of possible color combinations. It is expected that with the appropriate nanoparticle surface functionalization these layer-by-layer particle architectures will provide as a powerful tool towards *in vitro* and intracellular applications in fundamental biology, cell signaling, biomedicine and high throughput cellular and pharmaceutical screening.

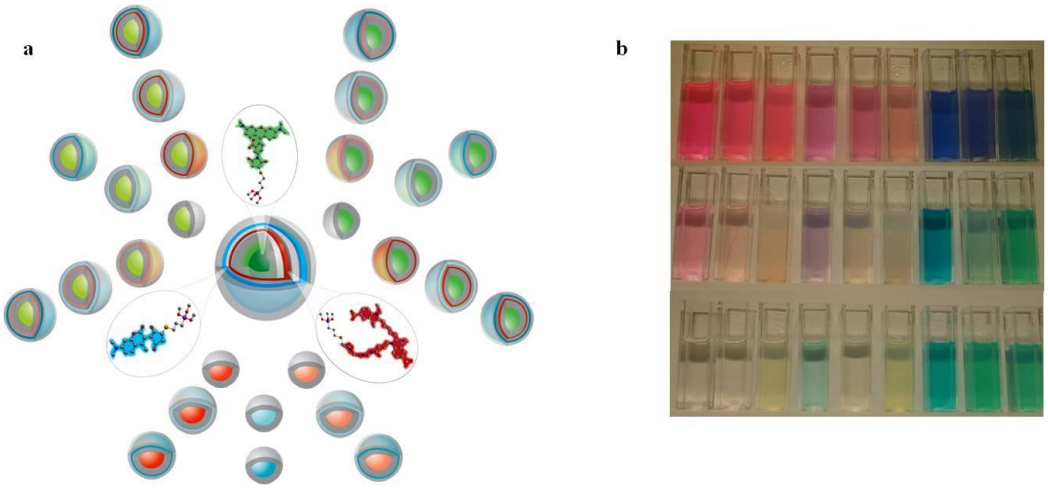

Figure 2.1.(a) Schematic illustration of layer-by-layer approach for incorporating the three dyes TMRm (green), Cy5m (red) and DACm (blue) in silica nanoparticles (center) and the possible combinations based on the encapsulation levels for each dye (0, 5, 20 dyes, respectively). For simplicity, particles with medium/high dye loading (~ 5/20 dyes per particle) are shown with a lighter/darker shade of green, red and blue. (b) Photo taken of the 26 synthesized core-shell multicolor fluorescent nanoparticles in water arranged in different rows as particles with no TMRm (bottom row), particles with ~ 5 TMRm (middle row) and particles with ~ 20 TMRm dyes in the core (top row). Note that the 27th cuvette on the left of the lowest row depicts a solution of pure silica particles without any dye, i.e. with color combination 0, 0, 0.

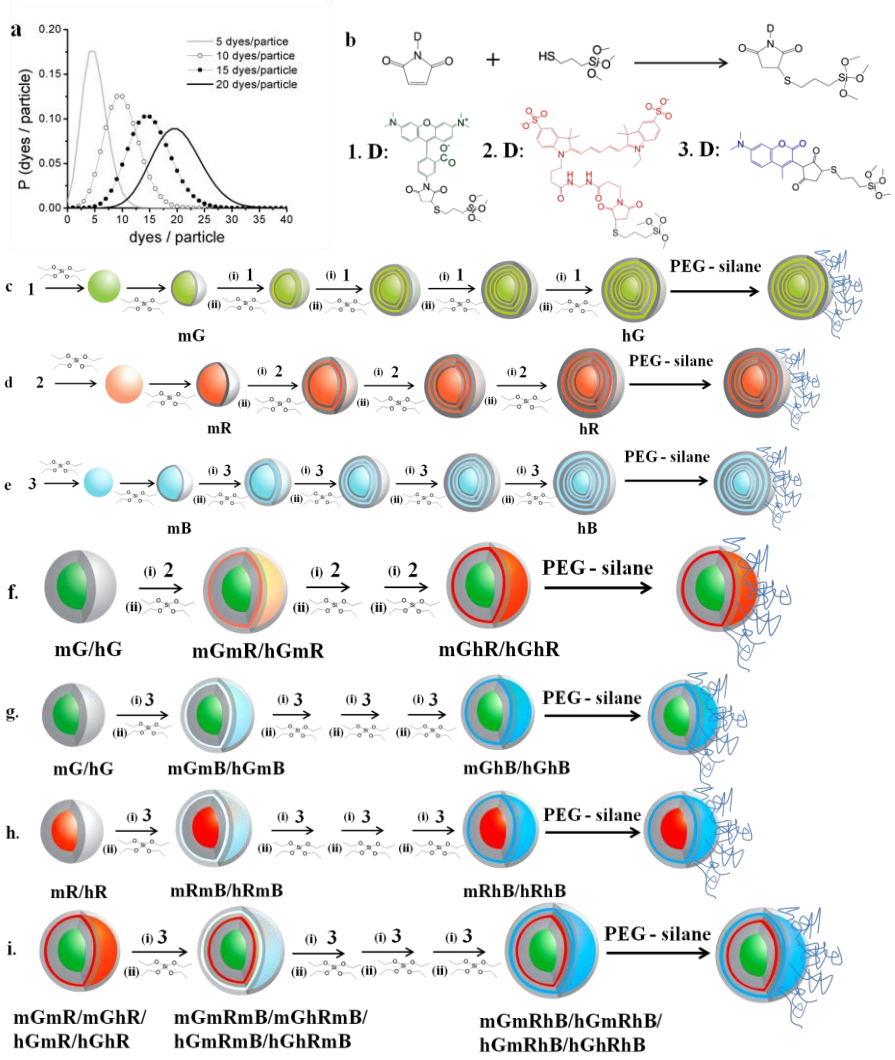

Figure 2.2. Schematics of *multicolor*C dots (*mc*C dots) synthesis: (a) Plot comparing the overlap between Poisson distributions for synthesis batches with different average numbers of dyes per particle, see legend. (b) Generalized reaction schematic of maleimide derivative of the three dyes TMRm (1), Cy5m (2) and DACm (3) with (3-mercaptopropyl)-trimethoxysilane to give the respective dye-silane conjugate. (c-e) Layer-by-layer dye addition for single color C dots: TMRm particles (G), Cy5m particles (R) and DACm particles (B), followed by the addition of a 5k molar mass polyethylene glycol silane (PEG-silane) as the final layer; (f-h) layer-by-layer approach to dual color *mc*C dots with different brightness levels for (f) G and R, (g) G and B and (h) R and B combinations starting from G and R single color C dots, followed by capping with PEG-silane; (i) layer-by-layer approach to triple color C dots capped with PEG-silane starting from G and R containing dual color C dots.

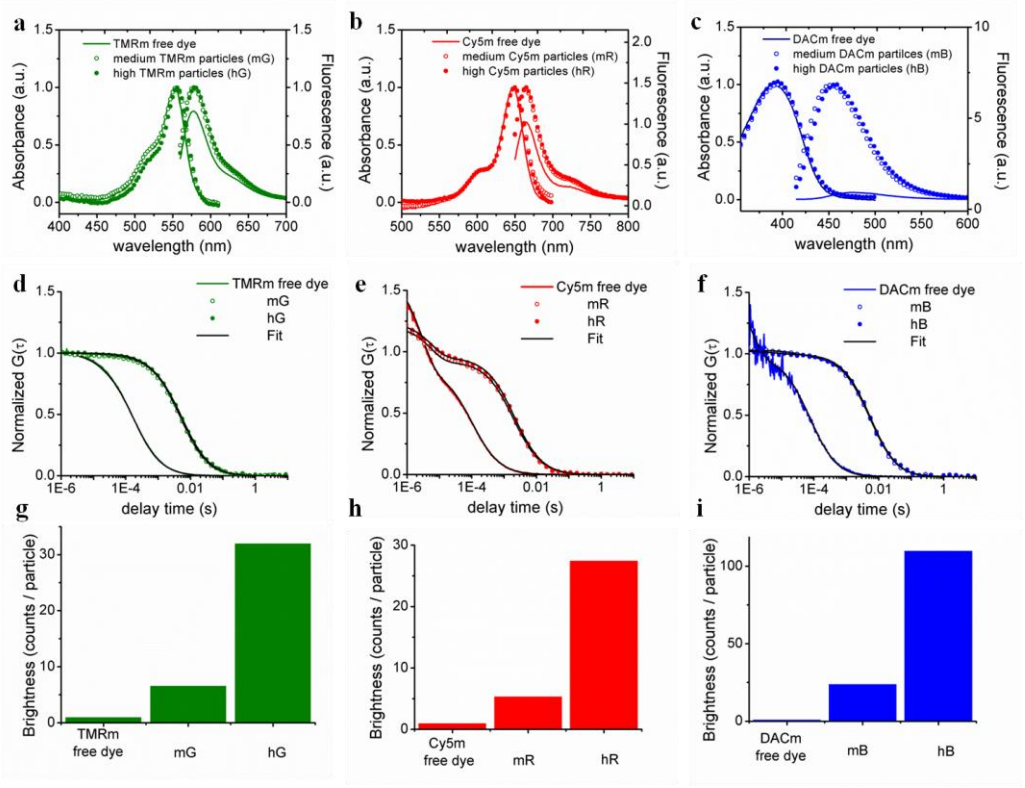

Figure 2.3. Characterization of single color C dots. Panels (a-c) compare the absorbance and fluorescence spectra of medium and high dye loaded nanoparticles to the parent free dye for (a) TMRm, (b) Cy5m and (c) DACm. Solutions of free dye and particles were absorbance matched before these measurements. Panels (d-f) compare the FCS autocorrelation curves of the free dyes (solid lines) with those of medium (hollow circles) and high (solid circles) dye loaded nanoparticles in solutions: (d) TMRm, (e) Cy5m and (f) DACm. Panels (g-i) compare the brightness per fluorescent species (dyes vs particles) as measured from FCS detector data sets for (g) TMRm system, (h) Cy5m system and (i) DACm system.

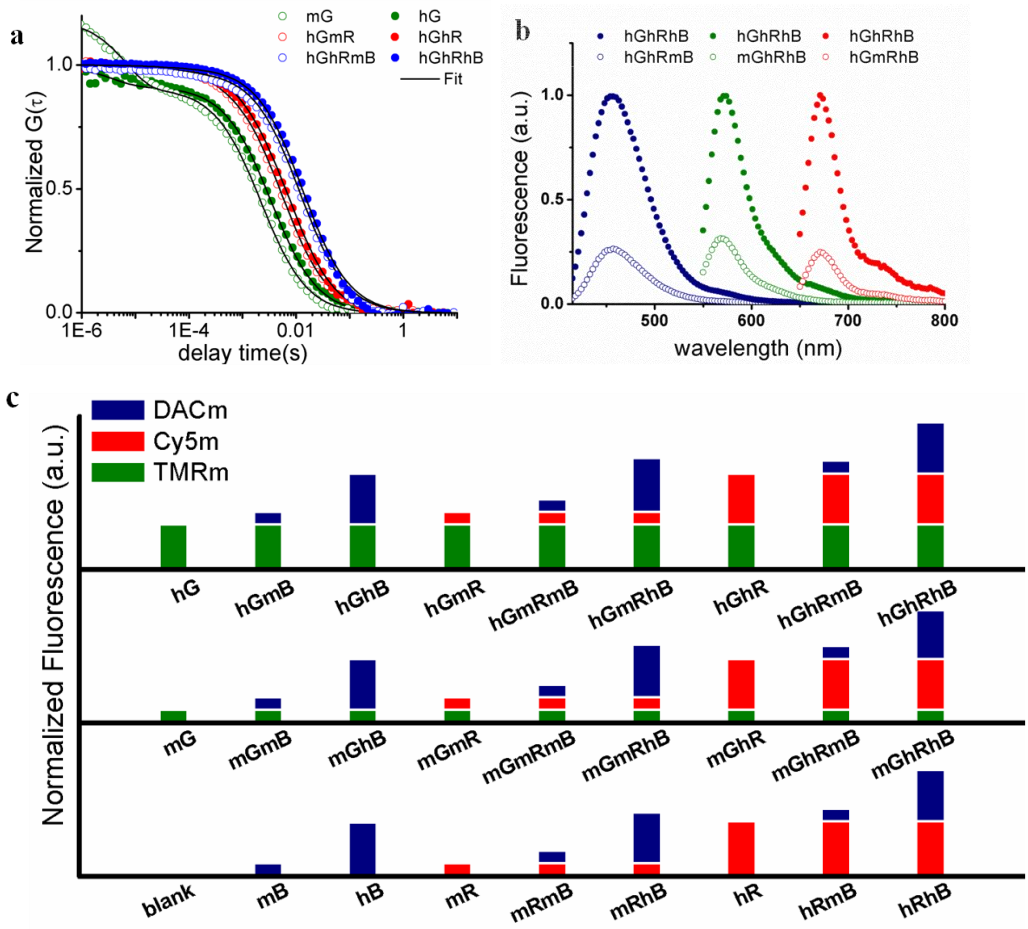

Figure 2.4. Characterization of *mc*C dots (a) Representative FCS curves of specific particle intermediates in solution moving towards triple color C dots covering the entire synthetic scheme starting from medium/high TMRm dye loaded single color C dots (mG, hollow green circles/hG, solid green circles) via medium/high Cy5m dye loaded dual-color C dots (hGmR, hollow red circles/hGhR, solid red circles) to the final triple color C dots with medium/high DACm dye loadings (hGhRmB, hollow blue circles/hGhRhB, solid blue circles). (b) Representative fluorescence emission spactra of triple color C dots as obtained by excitation in the blue (left), green (middle) and red (right). (c) Summary of experimental intensity profiles for each of the 26 fluorescent silica nanoparticles as measured by steady-state fluorescence emission spectra. Green bars represent emission from TMRm, red bars from Cy5m and blue bars from DACm. Bar heights represent emission intensity levels.

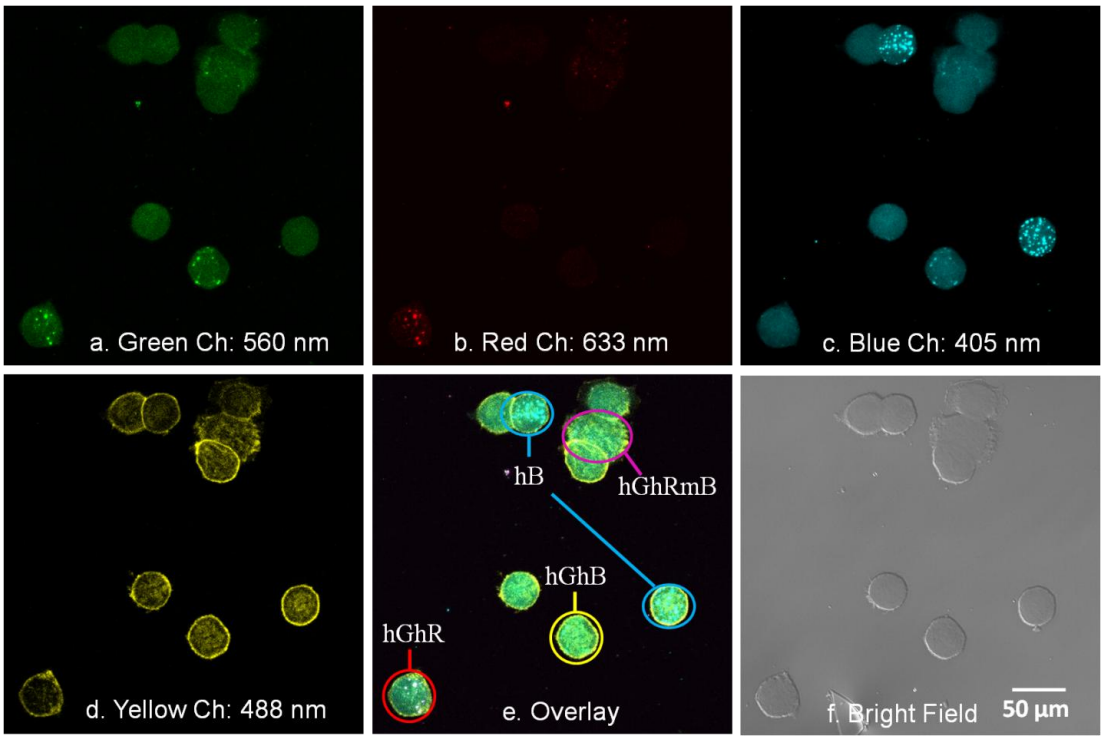

Figure 2.5. Confocal fluorescence microscopy images of *mc*C dots in RBL-2H3 mast cells showing channel, (a) Green Ch: 560 nm, (b) Red Ch: 633 nm, (c) Blue Ch: 405 nm, (d) Yellow Ch: 488 nm; (e) overlaid images of (a,b,c and d) (f) bright-field image.

REFERENCES

(1) Ferguson, J. A.; Boles, T. C.; Adams, C. P.; Walt, D. R. A fiber-optic DNA biosensor microarray for the analysis of gene expression. *Nature biotechnology* **1996**, *14*, 1681–4.

(2) Lockhart, D. J.; Winzeler, E. a Genomics, gene expression and DNA arrays. *Nature* **2000**, *405*, 827–36.

(3) Fodor, S.; Read, J.; Pirrung, M.; Stryer, L.; Lu, A.; Solas, D. Light-directed, spatially addressable parallel chemical synthesis. *Science* **1991**, *251*, 767–773.

(4) Braeckmans, K.; De Smedt, S. C.; Leblans, M.; Pauwels, R.; Demeester, J. Encoding microcarriers: present and future technologies. *Nature reviews. Drug discovery* **2002**, *1*, 447–56.

(5) Woolley, A. T.; Mathies, R. A. Ultra-high-speed DNA fragment separations using microfabricated capillary array electrophoresis chips. **1994**, *91*, 11348–11352.

(6) Knight, J. When the chips are down. *Nature* **2001**, *410*, 860–1.

(7) Ramakrishnan, R. An assessment of Motorola CodeLinkTM microarray performance for gene expression profiling applications. *Nucleic Acids Research* **2002**, *30*, 30e–30.

(8) Wilson, R.; Cossins, A. R.; Spiller, D. G. Encoded microcarriers for high-throughput multiplexed detection. *Angewandte Chemie (International ed. in English)* **2006**, *45*, 6104–17.

(9) Fenniri, H.; Ding, L.; Ribbe, A. E.; Zyrianov, Y. Barcoded Resins: A New Concept for Polymer-Supported Combinatorial Library Self-Deconvolution. *Journal of the American Chemical Society* **2001**, *123*, 8151–8152.

(10) Nam, J.-M.; Thaxton, C. S.; Mirkin, C. a Nanoparticle-based bio-bar codes for the ultrasensitive detection of proteins. *Science (New York, N.Y.)* **2003**, *301*, 1884–6.

(11) Wu, C.; Zheng, J.; Huang, C.; Lai, J.; Li, S.; Chen, C.; Zhao, Y. Hybrid silica-nanocrystal-organic dye superstructures as post-encoding fluorescent probes. *Angewandte Chemie (International ed. in English)* **2007**, *46*, 5393–6.

(12) Osaki, F.; Kanamori, T.; Sando, S.; Sera, T.; Aoyama, Y. A quantum dot conjugated sugar ball and its cellular uptake. On the size effects of endocytosis

in the subviral region. *Journal of the American Chemical Society* **2004**, *126*, 6520–1.

(13) Howarth, M.; Takao, K.; Hayashi, Y.; Ting, A. Y. Targeting quantum dots to surface proteins in living cells with biotin ligase. *Proceedings of the National Academy of Sciences of the United States of America* **2005**, *102*, 7583–8.

(14) Chithrani, B. D.; Ghazani, A. a; Chan, W. C. W. Determining the size and shape dependence of gold nanoparticle uptake into mammalian cells. *Nano letters* **2006**, *6*, 662–8.

(15) Jiang, W.; Kim, B. Y. S.; Rutka, J. T.; Chan, W. C. W. Nanoparticle-mediated cellular response is size-dependent. *Nature nanotechnology* **2008**, *3*, 145–50.

(16) Lu, F.; Wu, S.-H.; Hung, Y.; Mou, C.-Y. Size effect on cell uptake in well-suspended, uniform mesoporous silica nanoparticles. *Small (Weinheim an der Bergstrasse, Germany)* **2009**, *5*, 1408–13.

(17) Han, M.; Gao, X.; Su, J. Z.; Nie, S. Quantum-dot-tagged microbeads for multiplexed optical coding of biomolecules. *Nature biotechnology* **2001**, *19*, 631–5.

(18) Fulton, R. J.; McDade, R. L.; Smith, P. L.; Kienker, L. J.; Kettman, J. R. Advanced multiplexed analysis with the FlowMetrix system. *Clinical chemistry* **1997**, *43*, 1749–56.

(19) Li, Y.; Cu, Y. T. H.; Luo, D. Multiplexed detection of pathogen DNA with DNA-based fluorescence nanobarcodes. *Nature biotechnology* **2005**, *23*, 885–9.

(20) Wang, L.; Tan, W. Multicolor FRET silica nanoparticles by single wavelength excitation. *Nano letters* **2006**, *6*, 84–8.

(21) Marcon, L.; Spriet, C.; Meehan, T. D.; Battersby, B. J.; Lawrie, G. a; Héliot, L.; Trau, M. Synthesis and application of FRET nanoparticles in the profiling of a protease. *Small (Weinheim an der Bergstrasse, Germany)* **2009**, *5*, 2053–6.

(22) Ries, J.; Schwille, P. Fluorescence correlation spectroscopy. *BioEssays : news and reviews in molecular, cellular and developmental biology* **2012**, *34*, 361–8.

(23) Cohen, B.; Martin, C.; Iyer, S. K.; Wiesner, U.; Douhal, A. Single Dye Molecule Behavior in Fluorescent Core–Shell Silica Nanoparticles. *Chemistry of Materials* **2012**, *24*, 361–372.

(24) Larson, D. R.; Ow, H.; Vishwasrao, H. D.; Heikal, A. a.; Wiesner, U.; Webb, W. W. Silica Nanoparticle Architecture Determines Radiative Properties of Encapsulated Fluorophores. *Chemistry of Materials* **2008**, *20*, 2677–2684.

(25) Burns, A. A.; Vider, J.; Ow, H.; Herz, E.; Penate-Medina, O.; Baumgart, M.; Larson, S. M.; Wiesner, U.; Bradbury, M. Fluorescent silica nanoparticles with efficient urinary excretion for nanomedicine. *Nano letters* **2009**, *9*, 442–8.

(26) Stöber, W.; Fink, A.; Bohn, E. Controlled growth of monodisperse silica spheres in the micron size range. *Journal of colloid and interface science* **1968**, *69*, 62–69.

(27) Ow, H.; Larson, D. R.; Srivastava, M.; Baird, B. a; Webb, W. W.; Wiesner, U. Bright and stable core-shell fluorescent silica nanoparticles. *Nano letters* **2005**, *5*, 113–7.

(28) Van Blaaderen, A.; Vrij, A. Synthesis and characterization of colloidal dispersions of fluorescent, monodisperse silica spheres. *Langmuir* **1992**, *8*, 2921–2931.

(29) Clegg, R. M. Fluorescence resonance energy transfer. *Current opinion in biotechnology* **1995**, *6*, 103–10.

(30) Lawrie, G. a.; Battersby, B. J.; Trau, M. Synthesis of Optically Complex Core–Shell Colloidal Suspensions: Pathways to Multiplexed Biological Screening. *Advanced Functional Materials* **2003**, *13*, 887–896.

CHAPTER 3

Synthesis and characterization of bright multicolor fluorescent core-shell silica nanoparticles based on layer-by-layer particle architecture approach *

3.0 Abstract

Multicolor fluorescent particles have been developed to carry out multiplex assays and high throughput screening. Studies to date have either used quantum dots which are cytotoxic or organic dyes that cater towards utilizing Förster resonance energy transfer (FRET) which compromises on particle brightness. Here we provide a full account of the layer-by-layer (LbL) synthesis and characterization of bright multicolor fluorescent core-shell silica nanoparticles incorporating three different fluorescent dyes (green, red and blue) at three distinct dye concentrations (0, ~5 and ~20 dyes per particle). The LbL particle architecture has been devised such that the added dye layers show little to no energy transfer as quantified in detail in this report. The resulting single, dual and triple color particles have been characterized by a combination of fluorescence correlation spectroscopy (FCS), dynamic light scattering (DLS) and steady-state spectroscopy.

* Prepared for submission as: Srikant K Iyer, Ulrich Wiesner. "Synthesis and characterization of bright multicolor fluorescent core-shell silica nanoparticles based on layer-by-layer particle architecture approach"

3.1 Introduction

High throughput screening (HTS) and assays of biomarkers and compounds have great potential for clinical analysis and medical diagnostic applications. HTS techniques play a crucial role in identifying the expression levels of biomarkers for early disease detection, diagnosis and therapy.[1–7] This requires developing assays to screen chemical libraries for compounds or molecules of interest and target analytes like antigens, antibodies, peptides, nucleotides, enzymes etc.[8] Since thousands of molecules or reactions need to be traced, 'multiplex technologies' need to be developed to carry out multiple assays simultaneously and provide reliable and reproducible detection.[9] In order to carry out reliable and reproducible HTS assay development, chemical library management and screening operations need to develop simultaneously for rapid measurements.[3] The development of such assays depends on identifying the appropriate material that acts as the substrate or the carrier ensuring sensitivity and specificity to molecules of interest and in the process tracking these molecules. Chip-based technology has provided a suitable platform for carrying out multiplex assays via miniaturization and low consumption of samples by physically separating the molecules in wells or arrays on a 2-D plate, e.g. in high density DNA arrays or microchips.[10–12] Bead based technologies, on the other hand, rely on particles that are encoded or labeled with appropriate tags that are used to detect the target, and the appropriate surface functionalization provides the required sensitivity in binding to target analytes. Various strategies have been developed and demonstrated for encoding the beads, including chemical encoding, electronic encoding, graphical encoding and spectrometric encoding.[13–20] Optically encoded fluorescent beads have been widely

used and applied for detection owing to facile visualization and quantification of target molecules, facile access to existing technologies for detection (e.g. flow cytometry, spectroscopy) and relatively facile surface modification for the appropriate analyte of interest.

By choosing the number of intensity levels (or dyes per particle) 'N' and number of dyes/colors 'd', the number of combinations increases geometrically by the equation 'N^d-1'.[13] Thus theoretically a large library of fluorescently labeled beads can be synthesized for large scale analyte detection. Researchers and companies have developed different strategies to synthesize multicolor based beads using fluorescent species in the form of inorganic materials (quantum dots and lanthanides) and organic fluorophores.[13,15–17,21–27]

In order to explore applications like intra-cellular imaging and multiplexing, it is essential to develop bright nano-scale probes. Wiesner *et al.* have developed 5.0 nm to 70 nm Cornell dots or C dots which are bright fluorescent silica based nanoparticles incorporating organic dyes that show emission throughout the visible and near-infrared spectrum.[28–32] The rigid silica matrix around the covalently linked organic dyes reduces the non-radiative rates of decay while simultaneously increasing the radiative rates leading to significant per dye enhancements in fluorescence.[33] In a recent paper, we have developed sub 100 nm bright and optically encoded fluorescent dye based *multicolor* C dots (*mc*C dots).[34] We use three intensity or number-of-dyes-per-particle levels, N = 3 (0, 5, 20), and three dyes (RGB code, tetramethylrhodamine-5-maleimide (TMRm), Cy5-maleimide (Cy5m) and N-(7-dimethylamino-4-methylcoumarin-3-yl)-maleimide (DACm)), d = 3, to generate 26 distinguishable

encoded nanoparticles. The dye colors used for the particle synthesis were chosen based on commonly available laser lines e.g. used for flow cytometry and confocal imaging. Because of their small size < 100 nm, the *mc*C dots provide a platform to extend applications from assay development to bioimaging at the cellular level. In the present paper we describe more detailed characterizations of *mc*C dots based on steady-state measurements and single particle FCS measurements to reveal the photophysical properties of these particles.

3.2 *mc*C dot Nanoparticle Syntheses

The detailed syntheses of *mc*C dots have been described in previous work.[34] As a first step, commercially available maleimide derivatives of TMRm (1, green), Cy5m (2, red) and DACm (3, blue) were covalently conjugated with 3-mercaptopropyltrimethoxysilane (MPTMS) in a 1:25 molar ratio (Figure 3.1a). We synthesized medium and high dye loaded particles for single color dots with TMRm, Cy5m and DACm dyes for green (G), red (R) and blue (B) color coding, respectively. Medium dye loaded core-shell particles with ~5 dyes per particle were synthesized via a modified Stöber method.[29,35] High dye loaded particles with ~20 dyes per particle were synthesized by adding four TMRm/DACm dye layer-silica shells on the medium TMRm/DACm core-shell particles, and three Cy5m dye layer-silica shells were added on medium Cy5m core-shell particles. Following this layer-by-layer (LbL) synthesis of single color particles we further developed the particle architecture with two or three different dyes incorporated in a LbL-fashion as summarized in Figure 3.1. For simplicity each color layer in Figure 3.1 is depicted as a solid layer. In reality, similar

to the description above of the single color dots, for high dye numbers multiple dye layer-silica shell synthesis steps were used.[34]

The synthesis of *mc*C dots was designed such that TMRm (1) was encapsulated in the core as the first dye, followed by a thick silica shell that was grown to obtain TMRm incorporated core-shell nanoparticles (G). Cy5m (2) was added as the second dye layer to the TMRm doped core-shell nanoparticles to obtain dual color particles (G-R). Another thick silica shell was grown on the dual color particles and as a final step, DACm (3) was added followed by a silica shell to obtain core-shell particles containing all three dyes (G-R-B).

In order to distinguish *mc*C dot color codes we devised the following nomenclature for these particles: To denote fluorescence intensity levels we use lower case letters (m/h for medium/high, i.e. ~5/20 dyes per particle) and to denote fluorescence colors we use capital letters (G/R/B for green/red/blue emission, respectively). Each particle is named based on the sequence in which each color was added, moving from the core to the outer shell. For example, mGmRhB *mc*C dot has a medium green (~5 dyes) core, followed by a medium red (~5 dyes) inner shell, followed by a high blue (~20 dyes) outer shell. A missing color (i.e. zero dyes of that color) in a *mc*C dot is denoted by omitting its notation. For example, a hRmB *mc*C dot has no green (i.e. zero green dyes), a high red (~20 dyes) core, and a medium blue (~5 dyes) outer shell. In order to maximize brightness for this complex LbL particle architecture, it was important to identify the necessary silica shell thickness between layers of two different colors in order to minimize energy transfer between different dyes (which can act as donor and acceptor dye molecules).

3.3 Brightness per particle on increasing the number of dyes per particle

Fluorescence correlation spectroscopy (FCS) is a diffusion based measurement of fluorescent species in a defined focal volume. FCS derived autocorrelation data provide the diffusion time of these species which is related to their hydrodynamic radius/diameter.[36] The amplitude of the autocorrelation curve, $G(\tau)$, at $\tau = 0$, $G(0)$, provides the number of particles in the effective focal volume, while the associated average count rate measured by the optical detector can be used to determine the number of photons emitted per diffusing fluorescent moiety. Based on this information together with steady-state absorption measurements on free dyes and particles, the number of dyes per particle and the brightness per particle can be quantified as has been described in detail elsewhere.[33] Figure 3.2a shows the FCS detector derived brightness per particle for five TMRm particles of diameter ~ 25 nm, containing ~ 6, 10, 15, 18 and 27 dyes per particles. Figure 3.2b shows the same plot for four ~ 30 nm diameter Cy5m particles containing ~5, 11, 15 and 22 dyes per particle. All data points for the green and red particles, respectively, lie on a straight line thus indicating that the particles do not show any significant fluorescence quenching upon increasing the number of dyes up to high dye loadings (i.e. hG, hR). The brightness per particle or brightness factor can be defined as the product of the number of dye equivalents with the quantum efficiency enhancement per dye over that of free dye in aqueous solution.[33] On fitting the data points to a straight line, the slope values or quantum efficiency enhancements per dye over free dye calculated for TMRm and Cy5m particle systems were 1.18 (± 0.02) and 1.22 (± 0.02), respectively. These values are in close agreement to enhancement values of 1.32 and 1.47 for TMRm and Cy5m,

respectively, as obtained from steady-state fluorescence measurements of absorbance matched free dye and the corresponding dye incorporated nanoparticles.[34] Thus to obtain maximum brightness nanoparticles of high dye loadings, adding dye conjugates in a LbL-fashion worked well. The slight difference in the values obtained from the two independent measurements could be due to the fact that in FCS measurements only a sub-set of the dyes in the particles were excited as the measurements were carried out with polarized light, which in turn leads to smaller counts per particle. After synthesizing particles with medium (~ 5 dyes per particle) and high (~ 20 dyes per particle) dye loadings for TMRm and Cy5m systems, we focused our attention on adding spectrally distinct dye conjugates to the same particle for multicolor particle synthesis.

3.4 Energy transfer with increasing shell thickness

Organic fluorophores have broad absorbance and emission profiles, and depending on the spectral and spatial proximity show energy transfer. Förster resonance energy transfer (FRET) efficiency decreases as $1/r^6$, where 'r' is the separation distance between donor and acceptor dye pairs.[37] The Förster radius is the separation distance between donor and acceptor dyes at which 50% energy transfer is observed. Multicolor colloidal particles have been synthesized based on FRET, where the emission from a donor dye is the source of excitation for the acceptor dye.[15,17] Brightness of multicolor FRET based particles thus depends on the proximity of the dyes. An advantage of this approach is that it only requires a single laser source to excite the donor dye species and with it all other dyes (colors). In multicolor FRET based particles the more dye colors are used, however, the more does the photon

emission from donor dyes drop. Furthermore, the farther donor and acceptor dyes are separated, the more the process becomes inefficient. Both effects significantly compromise particle brightness and thus the number of distinguishable codes. To circumvent these issues we developed a particle architecture that would utilize maximum emission from every dye incorporated, yielding fluorescent multicolor particles with maximized brightness.

Based on the different dyes used for synthesis of *mc*C dots, appropriate shell thicknesses were grown to reduce energy transfer between them. TMRm dye being in the center of the spectrum would have the most spectral overlap as an acceptor with DACm dye and as a donor with Cy5m dye. The Förster radius (R_o) between the donor and the acceptor species for parent free dye pairs of DACm/TMRm and TMRm/Cy5m were calculated as 4.0 nm and 4.5 nm, respectively.[34] Since, Cy5m and DACm are on the extreme ends of the visible spectrum we expect very little energy transfer between these two dyes. As expected this pair thus shows a R_o value of only 1.5 nm. In order to identify the appropriate shell thickness at which the least energy transfer is observed varied silica shell thicknesses were grown on 10 nm diameter TMRm core particles and quantified by dynamic light scattering (DLS). Figure 3.3a shows a shift in the peak maxima of the DLS curves to the right with increasing nanoparticle size. As measured from DLS, on a 10 nm TMRm core particle silica-shell thicknesses of 6.5 nm, 9 nm and 12.0 nm were grown. To each of the differently sized TMRm core-shell particles, Cy5m and DACm dye conjugates were subsequently co-condensed to obtain TMRm-Cy5m and TMRm-DACm dual color particles, respectively. All particles involved in this particular part of our study were particles with medium dye loadings.

The extent of energy transfer between donor and acceptor dyes for the various particles was studied using steady-state spectroscopic methods. Aqueous particle solutions were absorbance matched to the donor peak and the fluorescence emission profiles of the donor/acceptor dyes were monitored. For example, particles containing TMRm (donor) and Cy5m (acceptor) were absorbance matched at the TMRm peak and excited at the TMRm absorption peak maximum wavelength of 560 nm (Figure 3.3a), while particles containing DACm (donor) and TMRm (acceptor) were absorbance matched at the DACm peak and excited at the DACm absorption peak maximum of 405 nm (Figure 3.3b). The fluorescence spectra were all normalized to the donor emission peak to monitor the magnitude of energy transfer to the acceptor by studying the emission of the acceptor dyes as a function of silica shell thickness between donors and acceptors.

Particles containing TMRm and Cy5m (Figure 3.3b) show a clear decrease in energy transfer with increasing spatial separation between the two dye layers. For shell thicknesses of 6.5 and 9.0 nm we see a considerable energy transfer via Cy5m emission, whereas for a shell thickness of 12.0 nm, all emission contributions from Cy5m have disappeared. Particles containing TMRm and DACm when excited at 405 nm (Figure 3.3c), showed a similar trend. At shell thicknesses of 6.5 nm and 9.0 nm, considerable energy transfer was noticed via TMRm emission. At a spatial separation of 12.0 nm TMRm fluorescence has disappeared from the spectrum.

In the case of particles containing only DACm and Cy5m very little energy transfer is expected between the two dyes at a shell thickness greater than 6-8 nm. Figure 3.4a shows representative FCS autocorrelation curves of medium Cy5m loaded

(mR) and medium Cy5m and DACm loaded (mRmB) particles. Both curves show a considerable triplet state contribution at short times which was accounted for in the fitting procedure (see experimental section). From analysis of these results, the particle diameter increases from 20 nm for mR particles to 36 nm for mRmB particles showing an increase in particle size of 16 nm or a silica separation of 8 nm between the Cy5m core particles and the DACm dye layer. Please note, since a 630 nm laser light source was used in the DLS instrument, scattering measurements could not be carried out on particles containing Cy5m. Figure 3.4b shows three representative FCS autocorrelation curves reflecting an increase in particle size as additional silica and dye layers are grown around a medium green core particle on the way to a triple color C dot. From the FCS fits, we extracted diffusion times and calculated diameters of the three particles. Fitting medium TMRm loaded core-shell particle (mG) data resulted in a particle diameter of 12 nm. The autocorrelation curves of particles containing medium TMRm and Cy5m (mGmR), suggested a particle diameter of 36 nm, indicating a 24 nm increase in particle size or a spatial separation of 12 nm between core-shell TMRm particles and Cy5m dye layer. Finally, the autocorrelation curve for triple color particles containing all three dyes with medium dye loadings (mGmRmB), gave a particle diameter of ~ 52 nm, equating to a size increase of about 16 nm or a spatial separation of 8 nm between the Cy5m and DACm dye layers. Figure 3.4c shows the fluorescence emission of absorbance matched single color (mB), dual color (mRmB) and triple color (mGmRmB) particles when excited at 405 nm. The dual color mRmB particles do not show emission in the red part of the spectrum and no emission is observed in the red or the green range of the spectrum for mGmRmB

particles. Furthermore, when compared to mB particles the dual and triple color particles show no drop in blue fluorescence corroborating the absence of energy transfer.

Based on the above studies a silica separation layer of at least 10-12.0 nm was grown on the core particles containing medium or high TMRm dye loadings (mG or hG) before co-condensing it with Cy5m or DACm dye conjugate in order to synthesize dual color C dots. A 6-8 nm silica shell was grown to separate both, the medium or high Cy5m loaded core particles (mR and hR) from a DACm dye layer to get dual color particles (no TMRm) as well as medium or high Cy5m loaded dual color particles (mGmR, mGhR, hGmR and hGhR) from a DACm dye layer to obtain triple color particles with medium and high dye loadings for each dye color.

3.5 Quantification of energy transfer for *mc*C dots

In our previous publication we outlined that based on steady-state spectroscopic studies the medium and high dye loaded *mc*C dots can be differentiated based on fluorescence intensities and that no significant energy transfer is observed between dyes in the same particle.[34] Here we discuss in detail measurements carried out to further quantify energy transfer in these particles. Steady-state measurements were performed on particles with donor and acceptor dyes. To this end particles containing donor-acceptor dye pairs were first absorbance matched to particles containing only donor dyes. Next, the fluorescence of the donor dye was measured for particles containing only the donor dye (F_D) and the particles containing donor-acceptor dye pairs (F_{DA}). Energy transfer was finally calculated from these quantities as shown in equation 1.[37]

$$percent\ energy\ transfer = \left(1 - \frac{F_{DA}}{F_D}\right) \times 100 \qquad (1)$$

For example, to calculate the energy transfer for dual color hGhR dots, hG particles were absorbance matched to hGhR particles using the TMRm signal. Subsequently, the fluorescence intensity of TMRm was measured and compared for both particles by exciting at 560 nm. Dual color hGhB or hRhB particles were absorbance matched in the blue spectrum for DACm absorption to single color hB dots and the fluorescence intensity compared by exciting the particles at 405 nm.

As shown in Figure 3.5a, mGmR and mGhR particles showed no energy transfer when compared to mG particles. This is expected due to spatial separation of 12 nm between the green and red dye layers. However, on comparing hGmR and hGhR to hG particles a small emission contribution from Cy5m is observed in the red part of the spectrum (Figure 3.5b). On comparing the fluorescence to hG we calculated a 15 % energy transfer between high TMRm loaded dyes and Cy5m dyes.

Similar measurements were carried out to quantify the energy transfer for DACm loaded particles. DACm dye conjugate is the final dye layer in blue color containing dual and triple color particles. Particles containing medium DACm dye loadings (mRmB, hRmB, mGmB, mGmRmB, mGhRmB, hGmB, hGmRmB, hGhRmB) were absorbance matched to particles containing only mB. Particles with high DACm dye loading (mRhB, hRhB, mGhB, mGmRhB, mGhRhB, hGhB, hGmRhB, hGhRhB) were absorbance matched to particles with only high DACm (hB) dye loading. The particle solutions were then excited at 405 nm and the resulting fluorescence emission was used to quantify energy transfer. Figure 3.5c compares

representative multicolor particles containing mB to particles with only mB. A small contribution in the green spectrum is observed for hGmB particles, showing a 14% energy transfer from blue to green. The hRmB and hGhRmB particles showed a 5% energy transfer, visible via a slight contribution in the red emission spectrum. Since the blue layer is separated from TMRm by a spatial separation of about 20 nm, no emission in the green spectrum is observed. Similar results were obtained for particles containing high DACm dye loadings (Figure 3.5d). The hGhB particles showed a 15 % energy transfer between blue and green dyes, whereas hRhB and hGhRhB particles only showed a 7 % energy transfer between blue and red dyes.

From these results we conclude that a small but finite amount of FRET does take place in these *mc*C dots. At first sight this is surprising as special care was taken in the particle design in the form of thicker silica shells between layers of different dyes to completely exclude this effect. In order to understand why FRET occurs despite this design it is instructive to take a closer look at the dye incorporation efficiencies during synthesis. We estimated dye incorporation efficiency for TMRm dye to be ~35%, whereas for Cy5m dye incorporation was calculated to be only ~18%. Since dye incorporation into the particles is not complete, during synthesis, in particular of high TMRm dye loaded particles, we expect unreacted dye conjugate to be present in the reaction mixture at all times subsequent to TMRm dye conjugate addition. On addition of subsequent silica shells, there is thus always a possibility that the unreacted TMRm dye conjugate gets trapped in the silica matrix. On addition of new dye layers, donor-acceptor dye pairs can get close to each other hence causing energy transfer. These contributions are consistent with the observation of the highest

energy transfer in hGhR and hGhB containing particles as these combinations from their synthesis have the highest probability of leading to donor-acceptor pairs with close proximity.

3.6 FCS based particle characterization of *mc*C dots

Since a LbL-approach was used for the synthesis of *mc*C dots, FCS measurements were carried out to quantify the increase in nanoparticle size as new dye layer-silica shells were added. All particles measured had a silica shell grown over the particle after the final dye layer addition. FCS measurements could not clearly resolve an increase in diameter upon the addition of only dye layer to the particles. Figure 3.6a shows FCS curves of single color particles containing Cy5m dye. To 20 nm diameter medium Cy5m loaded core-shell particles (mR) three Cy5m dye layer-silica shells were added resulting in 24 nm diameter high Cy5m dye loaded particles (hR). Both these curves show contributions from triplet states at short times which was accounted for in the fit of the autocorrelation curves. The 3 dye layers and 4 pure silica shells that were added to the primary core thus account for 7 distinct layers. As a final step an additional silica shell was added to hR single color particles followed by a PEG layer resulting in a final particle diameter of 75 nm for high Cy5m PEGylated (hR PEG) particles.

Following the synthesis of single color Cy5m loaded particles, DACm dye layer-silica shells were added to obtain dual color particles with no TMRm. Figure 3.6b shows the shift of FCS curves towards longer correlation times starting from mR to hR followed by addition of DACm dye layer-silica shells on hR particles resulting in dual color particles (hRmB, hRhB). To this end, on 24 nm diameter hR

nanoparticles a thick silica shell of about 8 nm was grown followed by the addition of a DACm dye conjugate-silica shell resulting in 40 nm diameter hRmB particles. Additional three DACm dye layer-silica shells resulted in 51 nm diameter hRhB particles. On synthesizing high DACm loaded particles from medium DACm particles the particle diameter thus showed an increase of 11 nm, compared to Cy5m particles, which showed a 4 nm increase in diameter for particles with high Cy5m loadings derived from medium Cy5m particles, *vide supra*. This is because for synthesis of DACm loaded particles, the TEOS concentration dosed for silica shell formation was 1.4 times higher as compared to dose concentrations for Cy5m loaded particles. The TEOS dose concentration for DACm loaded particles had to be optimized to increase electrostatic repulsions between particles, to overcome aggregation and precipitation upon DACm dye addition. The hRhB particles accounted for a total of 15 distinct layers around the mR core, of which 7 were dye layers and 8 were pure silica shells. As a final step a silica shell was grown on the hRhB particles followed by the addition of a PEG layer resulting in a final particle diameter of 83 nm.

For TMRm containing particles, medium TMRm loaded (mG) core-shell particles of 12 nm diameter were synthesized followed by four TMRm dye layer-silica shells to obtain 25 nm diameter high TMRm loaded (hG) particles (Figure 3.7a). Figure 3.7a shows representative FCS curves of the mG/hG particles, as well as of dual color particles with DACm dye (hGmB, hGhB) loadings. A 12 nm thick silica shell was added on 25 nm diameter hG particles, followed by addition of DACm dye conjugate-silica shell resulting in a hGmB particle diameter of 49 nm. Three additional DACm dye layer-silica shells produced 59 nm diameter hGhB particles, which

accounts for 8 dye layers and 9 pure silica shells giving a total of 17 distinct layers. As a final step an additional silica shell was grown followed by a PEG layer resulting in 80 nm diameter particles.

Figure 3.7b shows representative FCS curves moving from medium TMRm and Cy5m loaded dual color nanoparticles (mGmR) via high Cy5m dye loaded dual color nanoparticles (mGhR) to triple color particles containing medium DACm (mGhRmB) and high DACm (mGhRhB) dye loadings. As is evident from the figure, the correlation curves shift accordingly to longer and longer times starting from mGmR, dual color particles to mGhRhB, triple color particles, indicating an increase in particle sizes. Analysis of the autocorrelation curves of mGmR particles resulted in a particle diameter of 36 nm, indicating a 24 nm increase in particle size or a 12 nm spatial separation between mG core-shell particle of 12 nm diameter and Cy5m dye layer. To the mGmR particles two additional Cy5m dye conjugate-silica shells were added resulting in a particle diameter of 41 nm. To the dual color mGhR particles a silica shell of 8 nm was grown before DACm dye conjugate-silica shell layer addition resulting in a particle diameter of 57 nm, equating to a size increase of about 16 nm. Finally three DACm dye layer-silica shells were added to obtain 68 nm diameter mGhRhB particles. As mentioned above, the TEOS dose concentration on going from medium DACm loaded to high DACm loaded particles was 1.4 times higher as compared to dose concentrations on going from medium Cy5m loaded to high Cy5m loaded particles. This resulted in an 11 nm increase in particle diameter for DACm loaded particles compared to a 4-5 nm increase for Cy5m loaded particles. The triple color particle is made of 15 distinct layers, of which 7 account for dye layers and 8 for

pure silica shells. As a final step, an additional silica shell was grown followed by a PEG layer resulting in a final particle of diameter 82 nm.

Figure 3.7c compares representative FCS autocorrelation curves of single, dual and triple color particles with a final PEG coating. Overlap of the three curves suggests that the three PEGylated particles were grown to about the same size. hR particles were obtained by adding 3 Cy5m dye conjugate layers and 3 silica shells. In order to get a final diameter of 75 nm, one additional thick silica shell was grown on the hR particles followed by a PEG layer, thus resulting in 8 distinct layers (including PEG layer). A total of 17 distinct layers were added on mR particles to obtain 83 nm diameter hRhB (including PEG layer) particles. In order to obtain triple color mGhRhB PEG particles of diameter 82 nm, 16 distinct layers were added to mG core particles (including PEG layer). The sizes of all the final particles with PEG layer were maintained between 75 nm to 85 nm in order to enable similar behavior independent of color code e.g. in intracellular multicolor imaging.

3.7 Conclusion

In this paper we have shown that by carefully controlling the shell thickness we can devise particle architecture to synthesize multicolor silica nanoparticles that show little to no energy transfer. This makes it possible to obtain maximum emission from each dye used in the particle synthesis, thus increasing the signal to noise ratio and hence making detection easier. Each particle was characterized for the dyes per particle and brightness measurements were carried out to distinguish particles with medium and high dye loadings.

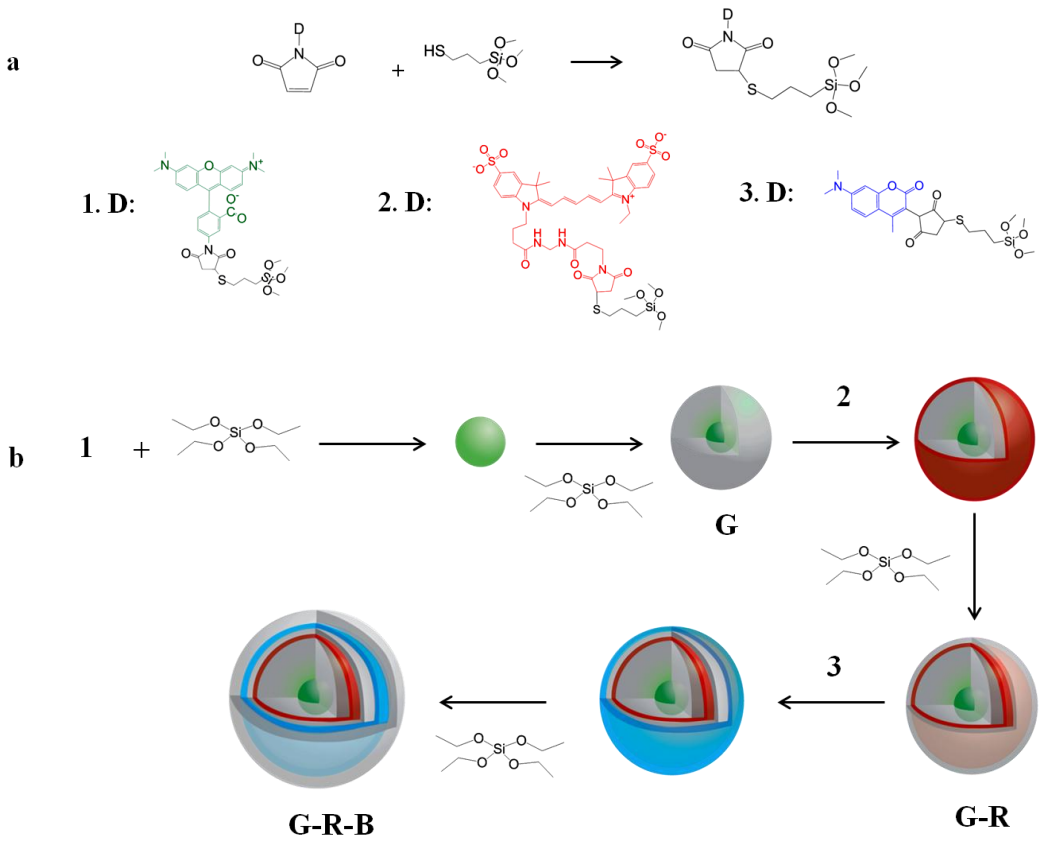

Figure 3.1. Synthesis schematic for *multicolor* C dots (*mc*C dots). (a) Dye conjugation of maleimide derivative of the three dyes TMRm (1), Cy5m (2) and DACm (3) with (3-mercaptopropyl)-trimethoxysilane. (b) Layer-by-layer approach to *mc*C dots. TMRm (green, 1) is co-condensed with tetraethoxysilane (TEOS) to form TMRm dye loaded core particles, followed by TEOS shell addition to get TMRm core-shell nanoparticles (G). Cy5m (red, 2) is added to G followed by TEOS shell addition to get dual color TMRm-Cy5m dye incorporated core-shell particles (G-R). The multicolor sequence is completed by adding DACm (blue, 3) to the G-R particles followed by TEOS shell addition to get triple color dye incorporated particles (G-R-B).

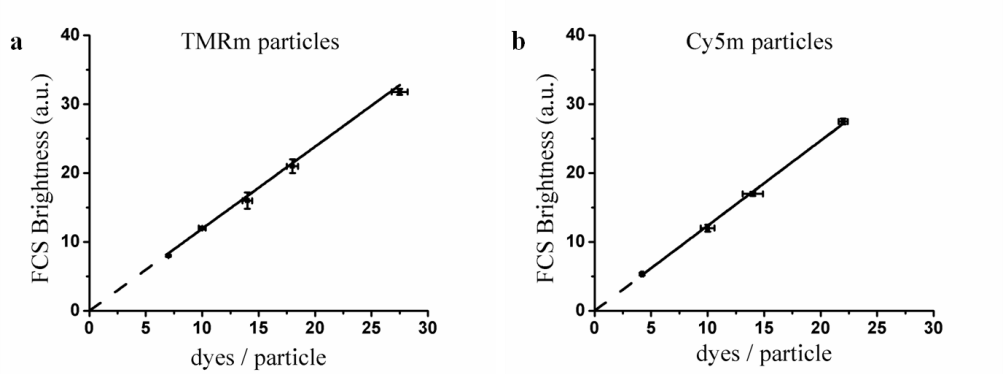

Figure 3.2. FCS brightness compared to dyes per particle for (a) dye loaded TMRm particles and (b) dye loaded Cy5m particles. Note, TMRm loaded particles were excited by 560 nm laser source while Cy5m loaded particles were excited by 633 nm laser source.

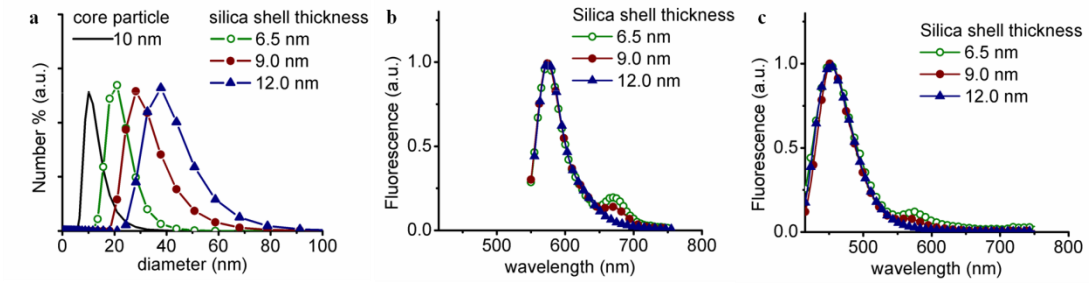

Figure 3.3. (a) DLS results on TMRm loaded particles showing an increase in particle diameter upon increasing silica shell thickness. (b, c) Effect of energy transfer with increase in shell thickness between donor-acceptor dye layers. (b) Fluorescence emission of the three TMRm (donor)-Cy5m (acceptor) dye incorporated particles when excited at 560 nm. (c) Emission of three TMRm (acceptor)-DACm (donor) dye incorporated particles when excited at 405 nm.

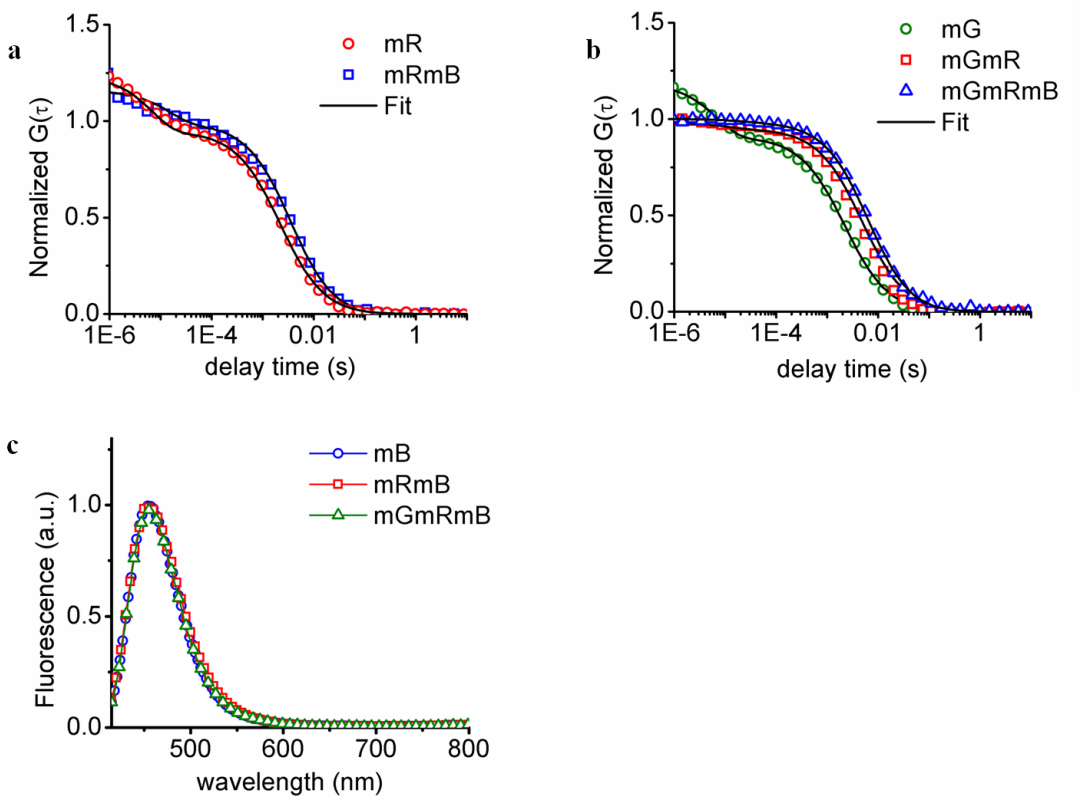

Figure 3.4. Representative FCS autocorrelation curves showing the increase in particle size with the addition of silica shell as a separation layer (a) between medium Cy5m (mR) and medium Cy5m-DACm particles (mRmB); (b) between medium TMRm (mG), medium TMRm-Cy5m dual color particles (mGmR, hollow red circles) and medium TMRm-Cy5m-DACm triple color particles (mGmRmB). (c) Fluorescence emission spectra for blue DACm containing single (mB), dual (mRmB) and triple (mGmRmB) color particles when excited at 405 nm.

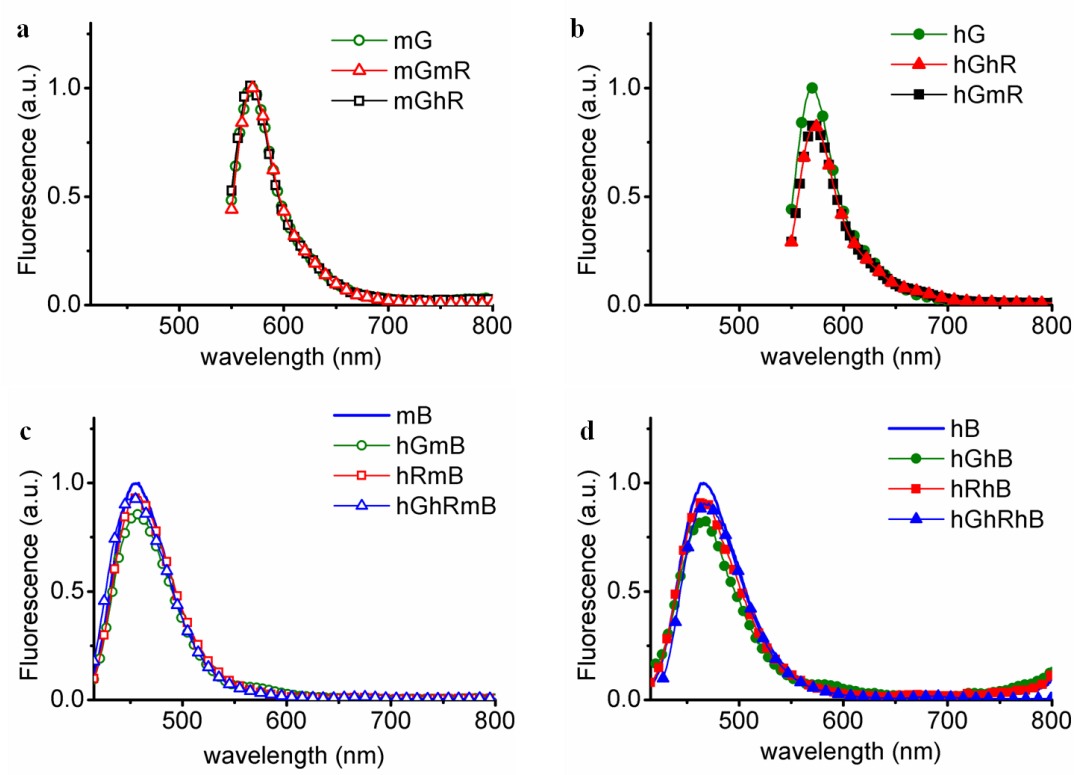

Figure 3.5. Representative fluorescence emission profiles quantifying energy transfer. (a,b) Comparison of fluorescence emission of core-shell particles containing medium and high TMRm dye loading (mG/hG) to dual color mGmR/mGhR and hGmR/hRhG particles when excited at 560 nm. (c) Comparison of the fluorescence emission of core-shell particles containing medium DACm dye loading (mB) to dual (hGmB, hRmB) and triple color (hGhRmB) particles. (d) Comparison of the fluorescence emission of core-shell particles containing high DACm dye loading (hB) to dual (hGhB, hRhB) and triple (hGhRhB) color particles. Particle solutions for (c) and (d) were excited at 405 nm.

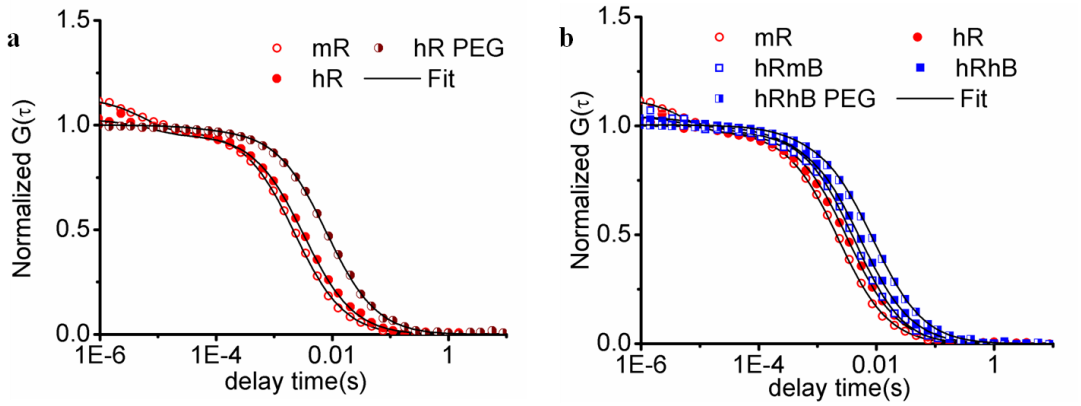

Figure 3.6. Representative FCS curves showing LbL-type dye conjugate-silica shell additions in single and dual color dots. (a) Single color Cy5m loaded particles starting from medium Cy5m (mR) to high Cy5m (hR) to high Cy5m PEGylated particles (hR PEG). (b) Dual color particles (no TMRm) starting from medium Cy5m / high Cy5m dye loaded particles (mR/hR) to medium/high DACm loaded particles (hRmB/hRhB) and adding a final, thicker silica shell as well as PEG layer (hRhB PEG).

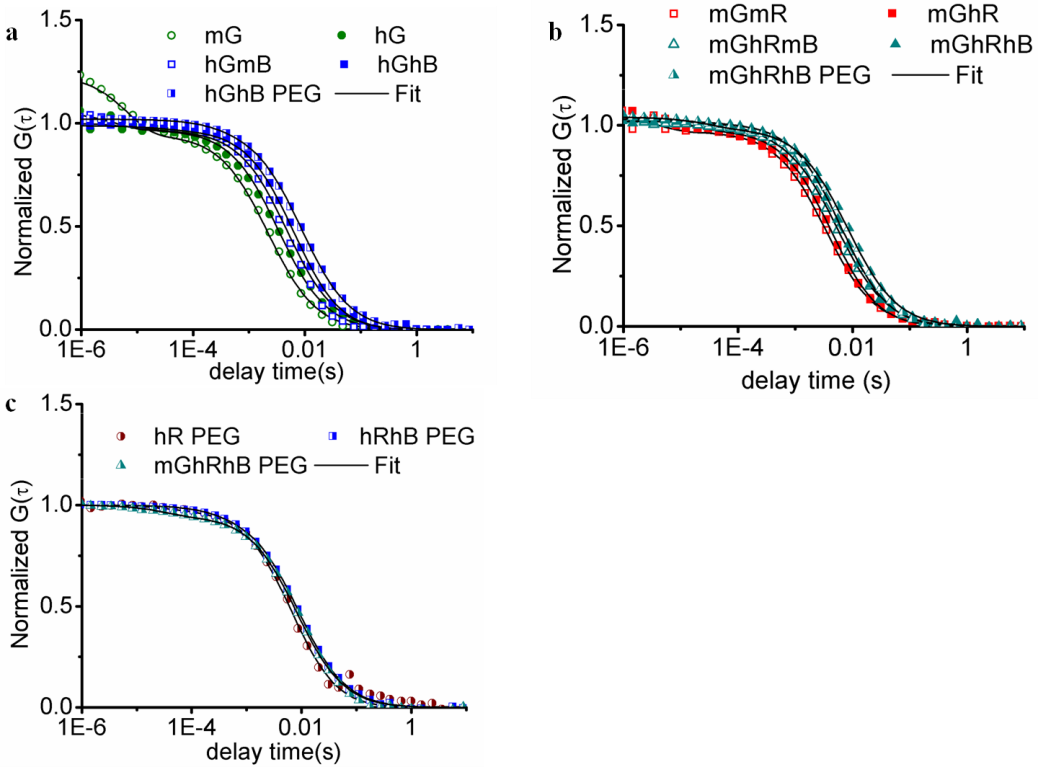

Figure 3.7. Representative FCS autocorrelation curves demonstrating growth sequences of various dual and triple color dots. (a) Dual color particles (no Cy5m) starting from medium TMRm/high TMRm dye loaded single color particles (mG/hG) via medium/high DACm loaded dual color particles (hGmB /hGhB) to thicker silica shell coated hGhB particles with PEG layer (hGhB PEG). (b) Triple color particles starting from particles containing medium TMRm dye loadings (mG) via dual color medium Cy5m/high Cy5m particles (mGmR/mGhR) to triple color medium DACm/high DACm loaded particles (mGhRmB/mGhRhB) to thicker silica shell coated mGhRhB particles with PEG layer (mGhRhB PEG). (c) FCS results comparing PEGylated single, dual, triple color particles (hR PEG/hRhB PEG/mGhRhB PEG) grown to similar sizes.

REFERENCES

(1) Ilyin, S. E.; Belkowski, S. M.; Plata-Salamán, C. R. Biomarker discovery and validation: technologies and integrative approaches. *Trends in biotechnology* **2004**, *22*, 411–6.

(2) Kingsmore, S. F. Multiplexed protein measurement: technologies and applications of protein and antibody arrays. *Nature reviews. Drug discovery* **2006**, *5*, 310–20.

(3) Hertzberg, R. P.; Pope, a J. High-throughput screening: new technology for the 21st century. *Current opinion in chemical biology* **2000**, *4*, 445–51.

(4) Lockhart, D. J.; Winzeler, E. a Genomics, gene expression and DNA arrays. *Nature* **2000**, *405*, 827–36.

(5) Fan, F.; Wood, K. V Bioluminescent assays for high-throughput screening. *Assay and drug development technologies* **2007**, *5*, 127–36.

(6) Fu, Q.; Schoenhoff, F. S.; Savage, W. J.; Zhang, P.; Van Eyk, J. E. Multiplex assays for biomarker research and clinical application: translational science coming of age. *Proteomics. Clinical applications* **2010**, *4*, 271–84.

(7) Jun, B.-H.; Kang, H.; Lee, Y.-S.; Jeong, D. H. Fluorescence-based multiplex protein detection using optically encoded microbeads. *Molecules (Basel, Switzerland)* **2012**, *17*, 2474–90.

(8) Inglese, J.; Johnson, R. L.; Simeonov, A.; Xia, M.; Zheng, W.; Austin, C. P.; Auld, D. S. High-throughput screening assays for the identification of chemical probes. *Nature chemical biology* **2007**, *3*, 466–79.

(9) Braeckmans, K.; De Smedt, S. C.; Leblans, M.; Pauwels, R.; Demeester, J. Encoding microcarriers: present and future technologies. *Nature reviews. Drug discovery* **2002**, *1*, 447–56.

(10) Fodor, S.; Read, J.; Pirrung, M.; Stryer, L.; Lu, A.; Solas, D. Light-directed, spatially addressable parallel chemical synthesis. *Science* **1991**, *251*, 767–773.

(11) Ferguson, J. A.; Boles, T. C.; Adams, C. P.; Walt, D. R. A fiber-optic DNA biosensor microarray for the analysis of gene expression. *Nature biotechnology* **1996**, *14*, 1681–4.

(12) Ferguson, J. a; Steemers, F. J.; Walt, D. R. High-density fiber-optic DNA random microsphere array. *Analytical chemistry* **2000**, *72*, 5618–24.

(13) Han, M.; Gao, X.; Su, J. Z.; Nie, S. Quantum-dot-tagged microbeads for multiplexed optical coding of biomolecules. *Nature biotechnology* **2001**, *19*, 631–5.

(14) Battersby, B. J.; Lawrie, G. a; Johnston, A. P. R.; Trau, M. Optical barcoding of colloidal suspensions: applications in genomics, proteomics and drug discovery. *Chemical communications (Cambridge, England)* **2002**, 1435–41.

(15) Wang, L.; Tan, W. Multicolor FRET silica nanoparticles by single wavelength excitation. *Nano letters* **2006**, *6*, 84–8.

(16) Wu, W.-B.; Wang, M.-L.; Sun, Y.-M.; Huang, W.; Cui, Y.-P.; Xu, C.-X. Color-tuned FRET polystyrene microspheres by single wavelength excitation. *Optical Materials* **2008**, *30*, 1803–1809.

(17) Marcon, L.; Spriet, C.; Meehan, T. D.; Battersby, B. J.; Lawrie, G. a; Héliot, L.; Trau, M. Synthesis and application of FRET nanoparticles in the profiling of a protease. *Small (Weinheim an der Bergstrasse, Germany)* **2009**, *5*, 2053–6.

(18) Xu, J.; Liang, J.; Li, J.; Yang, W. Multicolor dye-doped silica nanoparticles independent of FRET. *Langmuir : the ACS journal of surfaces and colloids* **2010**, *26*, 15722–5.

(19) Su, X.; Zhang, J.; Sun, L.; Koo, T.-W.; Chan, S.; Sundararajan, N.; Yamakawa, M.; Berlin, A. A. Composite organic-inorganic nanoparticles (COINs) with chemically encoded optical signatures. *Nano letters* **2005**, *5*, 49–54.

(20) Driskell, J. D.; Kwarta, K. M.; Lipert, R. J.; Porter, M. D.; Neill, J. D.; Ridpath, J. F. Low-level detection of viral pathogens by a surface-enhanced Raman scattering based immunoassay. *Analytical chemistry* **2005**, *77*, 6147–54.

(21) Fulton, R. J.; McDade, R. L.; Smith, P. L.; Kienker, L. J.; Kettman, J. R. Advanced multiplexed analysis with the FlowMetrix system. *Clinical chemistry* **1997**, *43*, 1749–56.

(22) Trau, M.; Battersby, B. J. Novel Colloidal Materials for High-Throughput Screening Applications in Drug Discovery and Genomics. *Advanced Materials* **2001**, *13*, 975–979.

(23) Chan, W. C. W.; Maxwell, D. J.; Gao, X.; Bailey, R. E.; Han, M.; Nie, S. Luminescent quantum dots for multiplexed biological detection and imaging. *Current opinion in biotechnology* **2002**, *13*, 40–6.

(24) Wang, D.; Rogach, A. L.; Caruso, F. Semiconductor Quantum Dot-Labeled Microsphere Bioconjugates Prepared by Stepwise Self-Assembly. *Nano Letters* **2002**, *2*, 857–861.

(25) Li, Y.; Cu, Y. T. H.; Luo, D. Multiplexed detection of pathogen DNA with DNA-based fluorescence nanobarcodes. *Nature biotechnology* **2005**, *23*, 885–9.

(26) Xu, J.; Liang, J.; Li, J.; Yang, W. Multicolor dye-doped silica nanoparticles independent of FRET. *Langmuir : the ACS journal of surfaces and colloids* **2010**, *26*, 15722–5.

(27) Ehlert, O.; Thomann, R.; Darbandi, M.; Nann, T. A four-color colloidal multiplexing nanoparticle system. *ACS nano* **2008**, *2*, 120–4.

(28) Herz, E.; Burns, A.; Bonner, D.; Wiesner, U. Large stokes-shift fluorescent silica nanoparticles with enhanced emission over free dye for single excitation multiplexing. *Macromolecular rapid communications* **2009**, *30*, 1907–10.

(29) Ow, H.; Larson, D. R.; Srivastava, M.; Baird, B. a; Webb, W. W.; Wiesner, U. Bright and stable core-shell fluorescent silica nanoparticles. *Nano letters* **2005**, *5*, 113–7.

(30) Burns, A.; Sengupta, P.; Zedayko, T.; Baird, B.; Wiesner, U. Core/Shell fluorescent silica nanoparticles for chemical sensing: towards single-particle laboratories. *Small (Weinheim an der Bergstrasse, Germany)* **2006**, *2*, 723–6.

(31) Herz, E.; Marchincin, T.; Connelly, L.; Bonner, D.; Burns, A.; Switalski, S.; Wiesner, U. Relative quantum yield measurements of coumarin encapsulated in core-shell silica nanoparticles. *Journal of fluorescence* **2010**, *20*, 67–72.

(32) Burns, A. A.; Vider, J.; Ow, H.; Herz, E.; Penate-Medina, O.; Baumgart, M.; Larson, S. M.; Wiesner, U.; Bradbury, M. Fluorescent silica nanoparticles with efficient urinary excretion for nanomedicine. *Nano letters* **2009**, *9*, 442–8.

(33) Larson, D. R.; Ow, H.; Vishwasrao, H. D.; Heikal, A. a.; Wiesner, U.; Webb, W. W. Silica Nanoparticle Architecture Determines Radiative Properties of Encapsulated Fluorophores. *Chemistry of Materials* **2008**, *20*, 2677–2684.

(34) Iyer, S.K.; Wilkes, M.; Cohen, R.; Wiesner, U.B.; Barbara, B. Multicolor Fluorescent Core-Shell Silica Nanoparticles for Multiplexed and Multicolor Intra-cellular Imaging. *in preparation* **2013**.

(35) Burns, A.; Ow, H.; Wiesner, U. Fluorescent core-shell silica nanoparticles: towards “Lab on a Particle” architectures for nanobiotechnology. *Chemical Society reviews* **2006**, *35*, 1028–42.

(36) Mertz, J.; Xu, C.; Webb, W. W. Single-molecule detection by two-photon-excited fluorescence. *Optics letters* **1995**, *20*, 2532.

(37) Clegg, R. M. Fluorescence resonance energy transfer. *Current opinion in biotechnology* **1995**, *6*, 103–10.

CHAPTER 4

Synthesis and characterization of bright near infrared chemiluminescent silica nanoparticles *

4.0 Abstract

Chemiluminescence brightness depends on the efficiency of interaction between a reactive intermediate and a dye and the ability of the excited fluorescent species to emit photons via radiative decay channels from the excited state. In this report we synthesized silica nanoparticles with different architectures in the size range of 60-70 nm. In particular we introduce a new class of bright near infrared (NIR) peroxyoxalate chemiluminescent (POCL) mesoporous silica nanoparticles (MSNs). Via covalent dye incorporation these nanoparticles suspended in ethyl acetate/1-hexanol solution showed four-fold enhancements in peak chemiluminescence intensity in the near infrared (NIR) region of the optical spectrum when compared to the free parent dye. This particle architecture further resulted in an 18-fold increase in the total photon counts emitted compared to free dye. By means of transient absorption measurements increased brightness in chemiluminescence was associated with switching off of a non-radiative decay pathway present only in the free parent dye. Comparison with other model particle architectures suggests that this behavior is due to particular orientational states of the dye as a result of the surfactant directed particle growth. The enhanced NIR radiative properties make these particles viable for sensitive analyte detection.

* Paper for submission as: S. K. Iyer, K. Johnson, S. Huettner, R.H. Friend, U. Wiesner. “Synthesis and characterization of bright near infrared chemiluminescent silica nanoparticles”

4.1 Introduction

Chemiluminescence (CL) is the emission of light by molecules that are electronically excited as a result of a chemical reaction without any external source of light. Due to the absence of photoexcitation, no background fluorescence occurs which ensures high signal to noise ratios, thus making it feasible to develop sensitive methods to detect and quantify analytes (chemicals) that participate in the CL reaction as a reactant or catalyst and generate photons.[1–6] Peroxyoxalate chemiluminescence (POCL) is commonly used to detect hydrogen peroxide which is involved in various pathological conditions and peroxide based explosives.[5,7–10]

POCL is an indirect type of CL, as the reactive intermediates (RI) or the reaction product from the primary reaction (step 1) do not emit a significant quantity of light, but transfer their energy to a fluorophore (denoted F in the following scheme) which becomes electronically excited (step 2, denoted F*) and subsequently releases its energy in the form of light, thereby returning to its ground state (step 3).[11,12] The steps in the light-generating process can be described as follows:

$$\text{Oxalate} + H_2O_2 + \text{base catalyst} \rightarrow \text{RI} \qquad (1)$$

$$\text{RI} + \text{F} \rightarrow \text{F*} \qquad (2)$$

$$\text{F*} \rightarrow \text{F} + h\nu \qquad (3)$$

The intermediates generated in POCL can excite many different types of fluorophores and thus the emission wavelength can be tuned through the entire visible and NIR spectrum by proper choice of emitters. It is important to note that the POCL reaction is a complex multistep process, hence the complete reaction mechanism has still not

been fully resolved despite numerous investigations.[11–18] The formation of the high energy intermediate (step 1) is the rate determining step and in turn affects the quantum efficiency of CL.[4] In order to obtain bright CL, various catalysts have been employed to alter the rate of formation of RI, however this has also accelerated the reaction thus requiring faster detection techniques.[14,17]

Recent reports have been published related to developing nanoparticle based contrast agents to detect hydrogen peroxide via POCL.[20–22] These agents were synthesized by physically encapsulating the organic dye and the oxalate molecule in nanoparticles[23,24] or encapsulating dyes in peroxyoxalate-based polymer nanoparticles[20,25], such that the oxalate precursors are in close spatial proximity to the dye, thus making it possible to carry out hydrogen peroxide detection via CL reactions. Despite initial success, these systems do pose the concern of dye leaching from the nanoparticle, thus limiting their applications.

In this study we have developed near infrared (NIR) CL probes that show an enhancement in brightness compared to the free parent dye (ADS832WS) as a result of covalent dye incorporation into a surfactant directed mesoporous silica nanoparticle. Stöber based silica nanoparticles have been explored for a variety of applications including photonics and biomedicine.[26,27] The modified Stöber method involves covalently incorporating organic dyes to obtain bright fluorescent silica based nanoparticles.[27–33] These dye incorporated nanoparticles show enhancement in the radiative rate of decay as well as decrease in the non-radiative rate of decay over free dye in aqueous solution leading to an enhancement in per dye fluorescence quantum yield.[30] Bright fluorescent dye incorporated silica nanoparticles are highly desirable

because they show low toxicity, are chemically stable at ambient conditions and show versatility towards functionalization chemistry.[27,29,32–34] Silica nanoparticles have also been synthesized by using surfactants that act as structure directing agents and are located in pores of the final silica matrix.[27,35,36] The intrinsic properties of these materials, such as high surface area, uniform pore distribution and large pore volume make them highly desirable as probes for sensing, biomedical imaging and as drug delivery carriers.[34,36–40]

In this work both dye modified Stöber particles and dye incorporated mesoporous silica nanoparticles were synthesized and their CL properties compared in ethylacetate/1-hexanol solution to the free parent dye. Dye incorporated mesoporous silica nanoparticles (dMSNs) resulted in an 18-fold increase in total photon counts and four-fold increase in CL peak intensity due to the presence of a single excited state compared to two excited states for the free parent dye as shown by transient absorption (TA) spectroscopy.

4.2 Experimental Section

Chemicals and Materials

All chemicals were used as purchased. ADS832WS dye (American Dye Source, Inc.) was dissolved in dimethylsulfoxide (DMSO, anhydrous > 99%, Sigma Aldrich). The dye was conjugated in DMSO solution with (3-isocyanatopropyl)triethoxysilane (ICPTS, ≥ 95%, Gelest Inc.). To synthesize nanoparticles, hexadecyltrimethylammonium bromide (CTAB, Sigma), ethyl acetate (ACS grade, Mallinckrodt Chemicals), ammonium hydroxide (NH_4OH, 29% Fisher Scientific) tetraethylorthosilicate (TEOS, ≥ 99%, GC, Aldrich) and deionized water

(DI-H_2O, Milli-Q, 18.2 MΩ-cm) were used. The particles were then suspended in 1-hexanol (analytical standard, Sigma Aldrich) to carry out CL measurements. To carry out CL measurements bis-(2-carbopentyloxy-3,5,6-trichlorophenyl)oxalate (CPPO, Sigma Aldrich) was dissolved in ethylacetate (ACS grade, Mallinckrodt Chemicals). Potassium hydroxide (KOH, AR (ACS) grade, Mallinckrodt Chemicals) was dissolved in hydrogen peroxide (H_2O_2, 30% aqueous, AR (ACS) grade, Mallinckrodt Chemicals) to initiate CL reaction.

Dye conjugation

To 1 mL of ADS832WS (4.5 mM in DMSO) solution neat ICPTS (56 μL) was added in a vial and stirred at room temperature in glove box under nitrogen atmosphere for 16 hours to obtain dye conjugate. The resultant dye conjugate was used for subsequent synthesis of dye-incorporated mesoporous silica nanoparticles without further purification.

Synthesis of dyed - core and core-shell silica nanoparticles

For a 10mL particle synthesis, DI water (1.2 M), 2.0 M ammonia in ethanol (0.3 M) and TEOS (0.105 M) was added to 9.1 mL ethanol. This reaction was left to stir overnight for about 16 hours. To 10mL of the basic solution, 150μL of dye-conjugate was added (from above) yielding dye coated core silica nanoparticles (dSNPs).

In order to make core-shell silica nanoparticles, different silica shell thickness was added to dSNP solutions resulting in dSNP-S1 and dSNP-S2. To dSNP solutions 70 μL of TEOS was added at a dose rate of 10 μL every 30 minutes to form dSNP-S1.

To synthesize dSNP-S2, 150 μL of TEOS was added at a dose rate of 10 μL every 30 minutes to dSNP solutions.

Synthesis of Mesoporous Silica Nanoparticles

Dye-incorporated mesoporous silica nanoparticles (dMSNs) were synthesized via a sol-gel method with CTAB as a template. In a 100 mL round bottom flask, 40 mL DI-H_2O, 2 mL of 54.8 mM CTAB solution and 352 μL ethyl acetate were added. After 3 minutes, 800 μL of NH_4OH was added. After 1 minute, 176 μL of the dye conjugate solution (from above) was added. After 1 minute, 200 μL of TEOS was added. After 5 minutes, 14.7 mL DI-H_2O was added. After 14 minutes, hydrochloric acid (2.0 M) was added until the solution was neutralized. To remove unreacted chemicals, the particle solution was cleaned by centrifugation and re-suspended in DI-H_2O three times. To remove CTAB, 1 mL of glacial acetic acid (95%, v/v) was added per 20 mL of particle solution and left to stir for 1 hour. To remove the acid and extracted CTAB, the particle solution was washed with DI-H_2O and ethanol solutions via centrifugation and particles finally re-suspended in ethanol and stored.[41,42] For CL measurements the nanoparticles were re-suspended in 1-hexanol at concentrations of about 4 mg/mL.

Chemiluminescence Measurements

Absorbance matching and CL measurements:

Equivalent dye concentrations of free parent dye (ADS832WS), dSNP, dSNP-S1, dSNP-S2 and dMSN solutions were prepared in ethyl acetate/1-hexanol containing CPPO, by absorbance matching the nanoparticle solution to a solution of the dye with known concentrations on a UV-visible spectrometer (Varian Cary 5000 UV-Vis-NIR).

For this purpose, CPPO (2.2 mM in ethyl acetate, 600 µL) and 1-hexanol (50 µL) were mixed in 3 mL plastic disposable cuvettes (PMMA), and baseline corrected for in the UV-visible spectrometer. ADS832WS (26 µM in 1-hexanol, 50 µL) was added to the sample cuvette to give a dye:oxalate ratio of 1:1050, and the absorbance was recorded between 750 – 900 nm. After that, to the additional cuvettes dSNP, dSNP-S1, dSNP-S2 and dMSN in 1-hexanol were added until the absorbance of the resulting solutions matched the absorbance of the ADS832WS dye solution. The final ethylacetate to 1-hexanol solvent ratio was maintained at 6:1 volume ratio. These solutions were subsequently used for CL measurements.

Immediately before CL measurements, a solution of KOH in hydrogen peroxide (0.8 mg/mL KOH in 30% hydrogen peroxide, 6µL) was added to the absorbance matched dye solutions. The resulting solutions were first mixed and then placed in the spectrofluorometer where the emission was measured at 832 nm, 15 seconds after KOH/peroxide addition over a period of 10 minutes (Photon Technologies International Quantamaster). In the time dependent CL measurements, t_{max} was the time at which the CL peak maximum was recorded and the half life ($t_{1/2}$) was calculated as the time at which the CL intensity value had decayed to half its peak maximum as measured at t_{max}. The total photons emitted during CL were calculated by integrating the area under the emission versus time curve. For each measurement the background photon counts were measured and subsequently subtracted from the CL measurements to calculate the total emitted photons. The integrated area under the curve for the free dye and the nanoparticle solutions was calculated between the limits

of $0 - 500$ seconds. note that the zero time point determined the start of data acquisition and did not include the 15 seconds of mixing.

Transient Absorption Spectroscopy

A Ti: Sapphire amplifier system (Spectra-Physics, Solstice) was used to produce a 1kHz train of 90 fs pulses at 800 nm. Portions of this were used to pump two home-built broadband non-collinear optical parametric amplifiers (NOPAs). One was tuned to generate a broadband probe over the 500-800 nm range and the other was cut to the 650-725 nm range and used as the pump pulse. For measurements from 100 fs to 2 ns the pump pulse was delayed using a mechanical stage (Newport) and every second one was blocked with a mechanical chopper. Pump and probe beams were focused to the same spot on the sample, then each probe pulse was detected and the differential transmission ($\Delta T/T$) calculated after averaging 1000 "pump on" and "pump off" shots for each time point. A fraction of the probe beam was split off before the sample, passed through a different area of the sample and used as a reference to correct for shot-to-shot variation in the probe. For detection, probe and reference beams were spectrally dispersed by a spectrograph (Andor, Shamrock SR-303i) onto two 1024-pixel, NMOS linear image sensors (Hamamatsu, S8381-1024Q) read out by custom-built electronics (Stresing Entwicklungsburo). Samples were measured in quartz cuvettes (Hellma) at room temperature.

Sample preparation: Free dye and dMSNs were dissolved in methanol to concentrations of 30 μg/mL and 10 mg/mL respectively. Although this is a different solvent than used for the original CL measurements, results suggest that the

mechanistic insights into the effects of encapsulation on CL efficiency may be applicable across different solvents.

Photoluminescence: Photoluminescence spectra were measured using a spectrograph (Andor, Shamrock SR-303i) coupled to an intensified CCD (Andor, iStar DH740-18U-73). The excitation pulse used was the same as that for the transient absorption spectroscopy.

4.3 Results and Discussion

4.3.1 Nanoparticle synthesis

The near-infrared dye ADS832WS was conjugated to a silica precursor molecule to obtain dense silica nanoparticles and mesoporous silica nanoparticles. As a first step, the amine group on the dye was covalently linked with 3-isocyanatoproplytriethoxysilane to form a dye conjugate (1, Figure 4.1(a)). A pre-requisite for CL to occur is that the reactive intermediate can diffuse to and interact with the dye.[12,15] Traditional dye incorporated core-shell silica nanoparticles or C dots are prepared by co-condensing the dye conjugate with tetraethylorthosilicate resulting in dye incorporated core particles, followed by growing thin silica shells.[29,31,32] However, this type of particle architecture is expected to prevent the interaction between the incorporated dye and the reactive intermediate, thus producing no CL emission. To circumvent this issue, Stöber based blank silica nanoparticles of 60 nm diameter were first synthesized followed by co-condensing a dye conjugate layer to the surface of these particles to form dye-coated silica nanoparticles (dSNP, Figure 4.1(b)).[26] To portions of these particles, thin silica shells of two distinct diameters

were grown to separate the conjugated dye from the solution environment to obtain dSNP-S1 and dSNP-S2 (see experimental section).[29,31–33,43]

We also synthesized dye incorporated mesoporous silica nanoparticles (dMSNs) to expand the particle architectures tested (Figure 4.1(c)). These were synthesized using CTAB as a structure directing agent in a basic aqueous solution resulting in highly porous nanoparticles (see experimental section). Previous results have shown that these particles have high surface area with pore sizes of 2.5-3.0 nm, potentially making them viable as CL probes as the porosity could facilitate the diffusion of the reactive intermediate to the incorporated dye. [41,42]

Scanning electron microscopy studies of the blank silica nanoparticles showed that they were narrowly dispersed in size with a diameter of 65 nm (Figure C.1, supplementary information). The addition of the dye layer and subsequent thin silica shells was then monitored by dynamic light scattering (Figure 4.2a). The hydrodynamic diameter first grew to 69 nm upon dye addition (~2 nm thickness) for dSNP, and then to 71 nm (dSNP-S1, 1 nm thick silica shell) and 73 nm (dSNP-S2, ~2 nm thick silica shell) on addition of first and second silica shells, respectively. The dSNP, dSNP-S1 and dSNP-S2 nanoparticles were subsequently suspended in ethylacetate/1-hexanol to carry out CL measurements.

Transmission electron microscopy (TEM) showed an average particle size for dMSNs of 60 nm (Figure 4.2b). The TEM image suggests that despite the incorporation of the dye, the hexagonal pore structure of the particle was preserved. Barret-Joyner-Halenda (BJH) analysis of nitrogen adsorption-desorption measurements showed the pore size to be 2.7 nm, consistent with previous work.[41]

This further corroborated that the structural integrity of the particles was preserved upon dye incorporation.

4.3.2 Effect of particle architecture on CL

POCL reactions that use aromatic based oxalate esters are typically carried out in mildly polar organic solvents like ethylacetate due to the poor stability of the diaryloxalate esters in polar or aqueous solutions[12,44,45] For stable silica nanoparticle suspensions, 1-hexanol was the choice of co-solvent as it showed good miscibility with ethylacetate. To investigate the CL profiles of the different particle architectures, dSNPs and dMSNs suspended in ethylacetate/1-hexanol (6:1 volume ratio) solutions were absorbance matched to the free parent dye for quantitative comparisons via UV-visible absorbance spectroscopy. Vials with CPPO in a mixture of ethylacetate and 1-hexanol were prepared as described in the experimental section. The dye doped nanoparticles and free dyes were suspended in 1-hexanol prior to absorbance matching. Various free dye to CPPO molar ratios were used to optimize the emission intensity for the free dye. For this study the dye to CPPO molar ratio chosen was 1:1050. ADS832WS shows an absorbance maximum at 840 nm in ethyl acetate/1-hexanol solvent mixture and the nanoparticles containing the dye were absorbance matched to the free parent dye at this maximum as demonstrated in Figure 4.3(a).

The CL emission peak maximum was observed at ~840 nm, i.e. in the NIR part of the optical spectrum, (Figure C.2, supplementary information). This wavelength was used to monitor the brightness and duration of CL emission as a function of time (Figure 4.3b). The results from CL measurements for the different particle architectures are summarized in Table 4.1 and compared to free parent dye.

Background subtraction was carried out for all solutions before plotting the CL time profile and calculating the total photon counts.

The CL profile of the free parent dye showed a peak maximum at approximately 25 seconds with a half life of 40 seconds (Figure 4.3c). The dSNP and dSNP-S1 solutions showed a peak maximum at approximately 30 seconds with a half life of 50 seconds, respectively, compared to free parent dye solution. However the peak intensity maxima for dSNP and dSNP-S1 solutions showed marginal changes compared to the CL emission maximum for free parent dye solution (Table 4.1). On further increasing the shell thickness to 2 nm (dSNP-S2), no CL was observed. The inset in figure 3c suggests that by 100 seconds dSNP, dSNP-S1 and dSNP-S2 show completion of CL with no further photon emission, whereas the free parent dye shows a gradual CL temporal decay with low CL emission intensity beyond 100 seconds. The total photon counts for dSNP and dSNP-S1 was measured to be 0.6 and 0.92, respectively, compared to free dye for the entire measurement time scale of 0-500 seconds.

In contrast to the conventional Stöber particles, CL of mesoporous silica nanoparticles was significantly enhanced. CL measurements of dMSN solutions (Figure 3c) resulted in an intensity peak maximum at 30 seconds with a half life of 100 seconds. These particles show a similar gradual decay in CL beyond 200 seconds as the free parent dye, albeit at higher overall intensities. Compared to free parent dye, dMSNs show a four-fold enhancement in CL peak intensity and an 18-fold increase in total photon counts over the entire measurement time scale of 0 – 500 seconds.

Addition of a 1 nm thick silica shell for dSNP-S1 solutions resulted in a marginal increase in CL peak maxima, however it showed a drop in the total photon counts released compared to the free parent dye. The disappearance of CL for dSNP-S2 solutions with a 2 nm thick silica shell suggests that the diffusion of the reactive intermediate to the dye in this case is completely inhibited. In contrast the high and regular porosity of dMSNs apparently, facilitates the diffusion of the reactive intermediate to the dye resulting in an 18-fold increase in total photon emission, thus significantly enhancing the CL compared to the free parent dye and dye bound to spherical particle surface. Surprisingly, and in contrast to what we had originally expected these porous particles did not show a significant delay in CL peak maximum. In order to better understand the underlying reason for this CL enhancement, transient absorption spectroscopy was carried out on samples of free parent dye and dMSNs.

4.3.3 Transient absorption spectroscopy

CL brightness depends on the efficiency of interaction between reactive intermediate and dye, ability of the excited species to react through a CL pathway and emit photons via radiative decay channels of the excited state. Previous work has shown that covalent encapsulation of fluorescent dyes in silica nanoparticles increases the radiative rate of decay and decreases the non-radiative rate of decay, resulting in increased particle brightness.[30] In order to understand the change in radiative properties upon encapsulation in the present CL measurements, transient absorption (TA) spectroscopy measurements were carried out to compare free parent dye and dMSNs.

In TA spectroscopy the excitation (pump) pulse promotes a fraction of the molecules to an electronically excited state, and is followed by a probe pulse at delay time τ with respect to the pump pulse. This allows measurement of the differential transmission ($\Delta T/T$), and in particular its temporal evolution, after new photoexcited species are created by the pump pulse. Certain key characteristics are associated with TA spectroscopy measurements. Increased transmission (positive $\Delta T/T$), can result from either depopulation of the ground state, called ground state bleach (GSB), or from stimulated emission (SE) of photoexcited species.[46,47] Decreased transmission (negative $\Delta T/T$) is additional photoinduced absorption (PIA) caused by any excited state species present. The evolution of these features with time allows the population dynamics of the photoexcited species to be tracked.[46,47] TA measurements provide the lifetime of the excited state, thus giving information about the electronic structure of the dye and the presence of deactivation pathways.[45]

Although measured in different solvents, the chemiluminescence spectrum of the free parent dye (Figure C.3(a), supplementary information) is similar to the photoluminescence spectrum (Figure C.3(b), supplementary information), so we assume that the photoexcited state is the same as the final emissive state accessed during the chemiluminescence process. Figure 4.4a and 4.4b compares the evolution of differential transmission for free dye and dMSNs, respectively, at different delay times, τ. Overall, the transient absorption spectra for free dye and dMSN solutions are very similar. There are two features apparent for both samples in the region of the visible spectrum probed: a low energy tail of the ground state bleach (GSB) at 700-800 nm and a photoinduced absorption (PIA) peaked around 575 nm. Additionally, in

the dMSN sample there is significant signal from 650-725nm resulting from scattering of the pump laser by the particles. As the PIA feature is apparent upon excitation and the spectral shape does not change significantly over the 2ns range tested by the experiment it is assigned to absorption of the initial photoexcited state, $S_1 \rightarrow S_n$.

Based on the TA spectra in Figure 4.4a and 4.4b, the normalized differential transmission of PIA (550-600 nm) and GSB (750-800 nm) traces were plotted as a function of time (Figure C.4(a), supplementary information). The PIA traces show no significant change in shape for the free dye and the dMSNs. The number of species involved and their lifetimes were obtained by fitting the PIA kinetic traces with exponential functions (Figure 4.4c). The dMSNs were best fit with a mono-exponential decay suggesting that the excitation of dyes incorporated in the nanoparticles resulted in one excited species with a longer lifetime of 276 ps. The PIA kinetics of the free parent dye was best fitted with a bi-exponential decay suggesting that its excitation resulted in two different excited state populations. For relevant comparisons, the free dye was fitted with a bi-exponential fit by fixing the 276 ps component, resulting in 76% of populations with a lifetime of 15 ps and 24% of the populations with a lifetime of 276 ps. No dependence was observed when the excitation fluence was reduced by an order of magnitude for the free dye and dMSNs (Figure C.4(b), supplementary Information). This suggests there are no bi-molecular, excitation density dependent processes involved in the decay of the photoexcited state in either the free dye or the dMSNs.

During CL measurements, the free parent dye and dMSN solutions were absorbance matched and the dye to CPPO ratio was kept the same, thus the source for

CL excitation was constant. The TA spectroscopy results show two different lifetimes for the free parent dye, which could indicate structural heterogeneity or the existence of the free dye in two different conformations. As shown in Figure 4.3b, the CL spectral shape and peak maxima look very identical for the free dye and dMSN solutions, suggesting no structural changes to the incorporated dye compared to free dye. Furthermore, no change in lifetime values were observed for the free parent dye over the two orders of magnitude concentration range tested (from 3 to 300 μg/mL, Figure C.5, supplementary information) which implies the absence of dimerization/aggregation. The low CL emission brightness is the result of a dominant non-emissive relaxation for one of the populations, possibly due to structural heterogeneity of the dye or a conformational change in the excited state. Upon covalent incorporation of the dye into mesoporous silica nanoparticles the non-radiative pathway is apparently suppressed as a mono-exponential decay is seen with an increased lifetime of 276 ps. Naturally this increases the emission, and so the CL, yield. This implies interaction between the reactive intermediate and the dye in dMSNs resulting in a similar, single excited state for the dye.

Comparison of the CL results of the mesoporous particles with those of conventional Stöber particles suggests that the brightness enhancement cannot be a result of dye incorporation into the silica matrix as the addition of silica layers on top of the dye either only had small effects on the CL (1 nm shell) or prevented it altogether (2 nm shell). Furthermore, as observed for the Stöber particles without an additional silica shell (dSNP) simple conjugation of the dye to the particle surface did not result in such enhancements either. So structurally there is something specific

about the way the dye is incorporated into the mesoporous silica nanoparticles (dMSNs).

As shown in Figure 4.1a the absorber dye ADS832WS is negatively charged which should lead to repulsive interactions with negatively charged silica. In the case of the mesoporous particles, however, silica grows around CTAB micelles which have positively charged head groups. It is thus likely that the negatively charged dyes are first associating with those micelles and that silica subsequently grows around this structure. This is consistent with the dyes staying accessible to the reactive intermediate, RI, of the light generating process in POCL. It is further conceivable that the dye – CTAB head group interaction leads to a specific orientation distribution of the dyes on the surface of the hexagonal silica pores which subsequently, once the CTAB surfactants are washed away, favors efficient CL. While results presented in this study clearly hint in this direction, more careful studies are necessary to identify the exact structural contributions to the highly efficient CL observed.

4.4 Conclusion

In this study different nanoparticle architectures were synthesized and tested for their suitability as NIR CL probes. The structural integrity of the mesoporous silica nanoparticles was preserved upon dye incorporation. Compared to conventional silica particle architectures with a dye surface layer and thin (1 or 2 nm) silica shells on top of the dye layer on silica cores and the free parent dye, dMSNs diplayed an 18-fold increase in the total photons released and at least a four-fold enhancement in CL peak maxima. TA spectroscopy results showed that the enhancement in CL brightness for dMSNs compared to the free parent dye was due to the disappearance of a shorter

lifetime component associated with a non-radiative decay mechanism, and hence an increase in lifetime as a result of covalent dye incorporation of the dye in a silica matrix. We suggest this could be due to a specific conformational restriction of the (excited) dye or elimination of the structural heterogeneity of the dye within the mesoporous silica particle. The increase in brightness shown by these particles makes them viable for sensitive hydrogen peroxide detection.

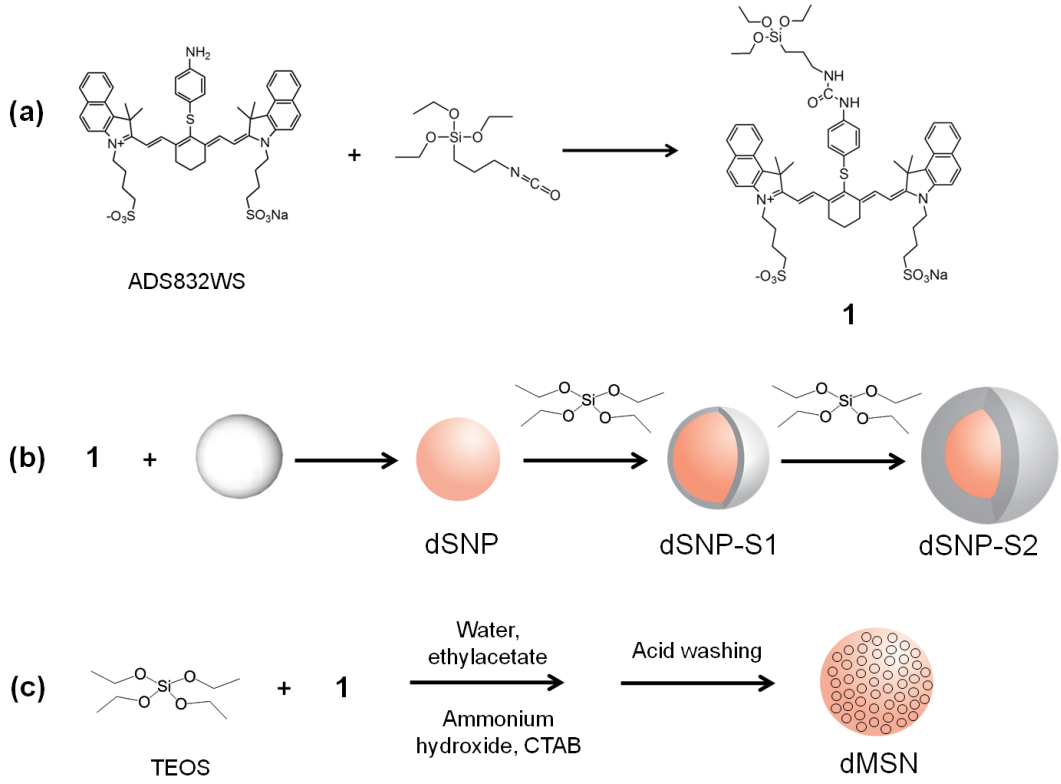

Figure 4.1. Overview of nanoparticle synthesis: (a) Reaction of ADS832WS with 3-isocyanatopropyl-triethoxysilane (ICPTS) to give dye conjugate (1); (b) Co-condensation reaction of dye conjugate (1) with blank silica nanoparticle to give dyed silica nanoparticles (dSNP), followed by thin silica shell addition to give dSNP-S1 and dSNP-S2; (c) Synthesis of dye incorporated mesoporous silica nanoparticles (dMSN).

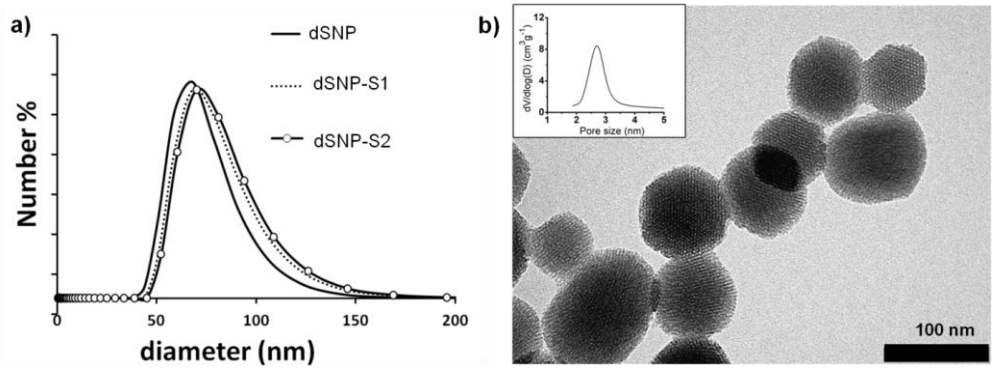

Figure 4.2. Characterization of nanoparticles (a) Dynamic light scattering of dSNP and dSNP-shells; (b) Transmission electron microscopy (TEM) of dMSN particles. Inset: Pore size distributions as obtained from adsorption measurements (V = pore volume and D = pore size).

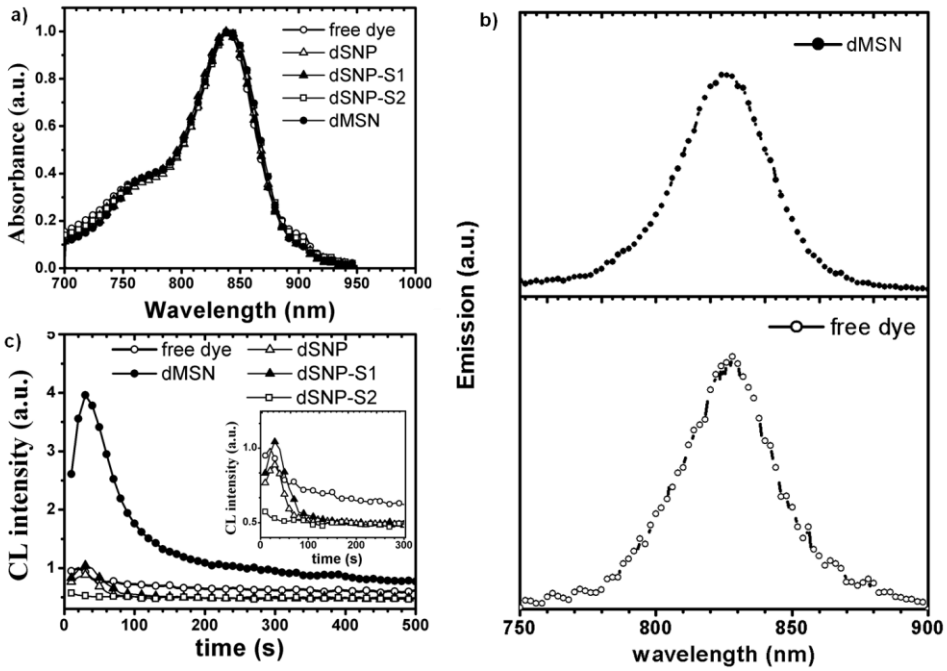

Figure 4.3. (a) Absorbance spectra of dSNP, dSNP-S1, dSNP-S2 and dMSN solutions matched to free parent dye. (b) Chemiluminescence emission profile as a function of wavelength for dMSN and free dye solutions. (c) Chemiluminescence emission profile as a function of time for dSNP, dSNP-S1, dSNP-S2 and dMSN solutions, compared to free parent dye. The inset shows a magnification of the early time region.

TABLE 1. CL emission profile of various particle architectures compared to parent free dye

sample	t_{max} (s)	half life ($t_{1/2}$,s)	I_{max} (counts)	enhancements (normalized to free dye)	total photon counts (area under the curve)	total photon counts normalized to free dye
free dye	25	40	1240.0	1.0	56801.0	1
dSNP	30	45	1178	0.95	33980.0	0.60
dSNP-S1	30	45	1364.0	1.1	52334.0	0.92
dMSN	30	100	5050.0	4.0	1040420.0	18.3

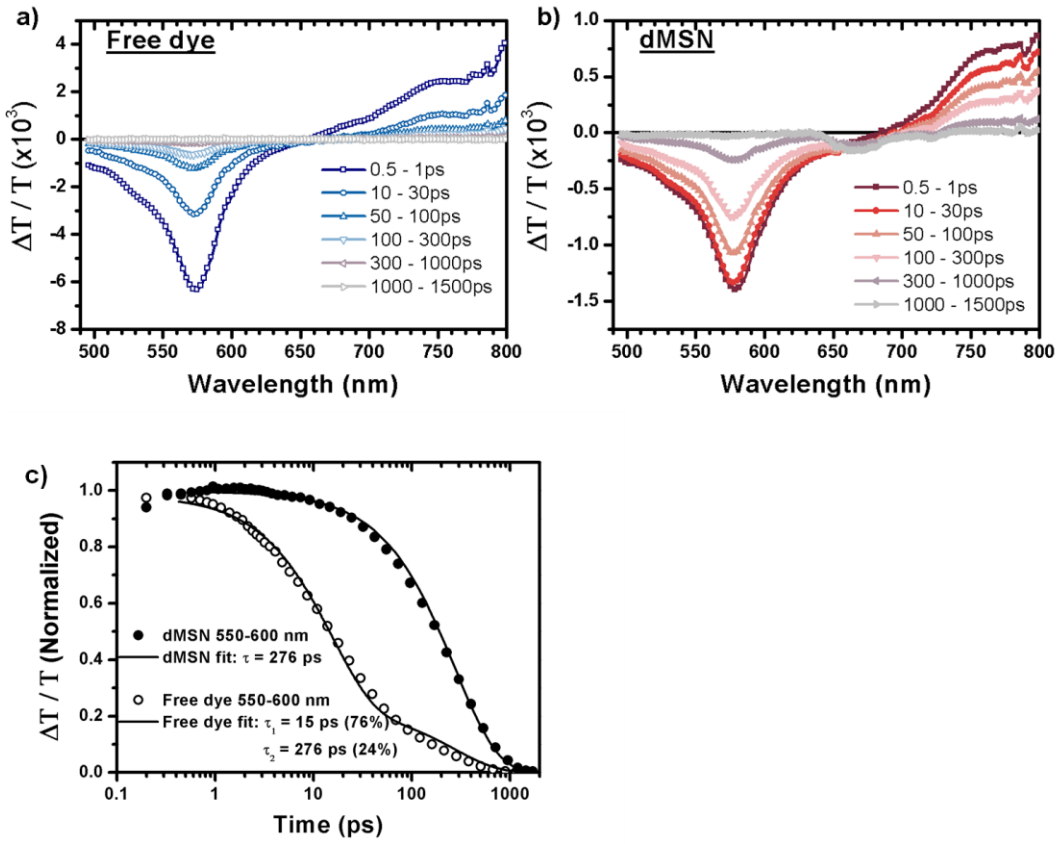

Figure 4.4. Transient absorption spectra of (a) the free dye and (b) the dye incorporated in the nanoparticle. (c) Transient absorption PIA kinetics for dye doped nanoparticles (dMSNs) and free dye, described by single exponential and bi-exponential fits, respectively. (λ_{ex} = 650-725nm, 50 μJ cm^{-2} per pulse).

REFERENCES

(1) Scott, G.; Seitz, W. R.; Ambrose, J. Improved determination of hydrogen peroxide by measurement of peroxyoxalate chemiluminescence. *Analytica Chimica Acta* **1980**, *115*, 221–228.

(2) Kobayashi, S.-I.; Sekino, J.; Honda, K.; Imai, K. Application of high-performance liquid chromatography with a chemiluminescence detection system to determine catecholamines in urine. *Analytical biochemistry* **1981**, *112*, 99–104.

(3) Sigvardson, K.; Kennish, J.; Birks, J. Peroxyoxalate chemiluminescence detection of polycyclic aromatic amines in liquid chromatography. *Analytical Chemistry* **1984**, *1102*, 1096–1102.

(4) Hanaoka, N.; Givens, R. S.; Schowen, R. L.; Kuwana, T. Stopped-flow determination of the parameters affecting the application of peroxyoxalate chemiluminescence to high-performance liquid chromatographic detection. *Analytical Chemistry* **1988**, *60*, 2193–2197.

(5) Schulte-Ladbeck, R.; Kolla, P.; Karst, U. Trace analysis of peroxide-based explosives. *Analytical chemistry* **2003**, *75*, 731–5.

(6) Tsunoda, M.; Imai, K. Analytical applications of peroxyoxalate chemiluminescence. *Analytica Chimica Acta* **2005**, *541*, 13–23.

(7) Lim, S. D.; Sun, C.; Lambeth, J. D.; Marshall, F.; Amin, M.; Chung, L.; Petros, J. a; Arnold, R. S. Increased Nox1 and hydrogen peroxide in prostate cancer. *The Prostate* **2005**, *62*, 200–7.

(8) Chang, M. C. Y.; Pralle, A.; Isacoff, E. Y.; Chang, C. J. A selective, cell-permeable optical probe for hydrogen peroxide in living cells. *Journal of the American Chemical Society* **2004**, *126*, 15392–3.

(9) Miller, E. W.; Albers, A. E.; Pralle, A.; Isacoff, E. Y.; Chang, C. J. Boronate-based fluorescent probes for imaging cellular hydrogen peroxide. *Journal of the American Chemical Society* **2005**, *127*, 16652–9.

(10) Albers, A. E.; Okreglak, V. S.; Chang, C. J. A FRET-based approach to ratiometric fluorescence detection of hydrogen peroxide. *Journal of the American Chemical Society* **2006**, *128*, 9640–1.

(11) Chandross, E. A new chemiluminescent system. *Tetrahedron Letters* **1963**, 761–765.

(12) Rauhut, M. Chemiluminescence from concerted peroxide decomposition reactions. *Accounts of Chemical Research* **1969**, *2*, 80–87.

(13) Alvarez, F. J.; Parekh, N. J.; Matuszewski, B.; Givens, R. S.; Higuchi, T.; Schowen, R. L. Multiple intermediates generate fluorophore-derived light in the oxalate/peroxide chemiluminescence system. *Journal of the American Chemical Society* **1986**, *108*, 6435–6437.

(14) Orosz, G. The role of diaryl oxalates in peroxioxalate chemiluminescence. *Tetrahedron* **1989**, *45*, 3493–3506.

(15) Koo, J.-Y.; Schuster, G. B. Chemiluminescence of diphenoyl peroxide. Chemically initiated electron exchange luminescence. A new general mechanism for chemical production of electronically excited states. *Journal of the American Chemical Society* **1978**, *100*, 4496–4503.

(16) Catherall, C. L. R.; Palmer, T. F.; Cundall, R. B. Chemiluminescence from reactions of bis(pentachlorophenyl)oxalate, hydrogen peroxide and fluorescent compounds. Kinetics and mechanism. *Journal of the Chemical Society, Faraday Transactions 2* **1984**, *80*, 823.

(17) Jonsson, T.; Irgum, K. New nucleophilic catalysts for bright and fast peroxyoxalate chemiluminescence. *Analytical chemistry* **2000**, *72*, 1373–80.

(18) Stevani, C. V.; Lima, D. F.; Toscano, V. G.; Baader, W. J. Kinetic studies on the peroxyoxalate chemiluminescent reaction: imidazole as a nucleophilic catalyst. *Journal of the Chemical Society, Perkin Transactions 2* **1996**, 989.

(19) Hadd, A.; Seeber, a; Birks, J. Kinetics of two pathways in peroxyoxalate chemiluminescence. *The Journal of organic chemistry* **2000**, *65*, 2675–83.

(20) Lee, D.; Khaja, S.; Velasquez-Castano, J. C.; Dasari, M.; Sun, C.; Petros, J.; Taylor, W. R.; Murthy, N. In vivo imaging of hydrogen peroxide with chemiluminescent nanoparticles. *Nature materials* **2007**, *6*, 765–9.

(21) Chen, R.; Zhang, L.; Gao, J.; Wu, W.; Hu, Y.; Jiang, X. Chemiluminescent nanomicelles for imaging hydrogen peroxide and self-therapy in photodynamic therapy. *Journal of biomedicine & biotechnology* **2011**, *2011*, 679492.

(22) Miller, E. W.; Albers, A. E.; Pralle, A.; Isacoff, E. Y.; Chang, C. J. Boronate-based fluorescent probes for imaging cellular hydrogen peroxide. *Journal of the American Chemical Society* **2005**, *127*, 16652–9.

(23) Dasari, M.; Lee, D.; Erigala, V. R.; Murthy, N. Chemiluminescent PEG-PCL micelles for imaging hydrogen peroxide. *Journal of Biomedical Materials Research Part A* **2009**, *89A*, 561–566.

(24) Lim, C.-K.; Lee, Y.-D.; Na, J.; Oh, J. M.; Her, S.; Kim, K.; Choi, K.; Kim, S.; Kwon, I. C. Chemiluminescence-Generating Nanoreactor Formulation for Near-Infrared Imaging of Hydrogen Peroxide and Glucose Level in vivo. *Advanced Functional Materials* **2010**, *20*, 2644–2648.

(25) Lee, D.; Erigala, V. R.; Dasari, M.; Yu, J.; Dickson, R. M.; Murthy, N. Detection of hydrogen peroxide with chemiluminescent micelles. *International journal of nanomedicine* **2008**, *3*, 471–6.

(26) Stöber, W.; Fink, A.; Bohn, E. Controlled growth of monodisperse silica spheres in the micron size range. *Journal of colloid and interface science* **1968**, *69*, 62–69.

(27) Burns, A.; Ow, H.; Wiesner, U. Fluorescent core-shell silica nanoparticles: towards "Lab on a Particle" architectures for nanobiotechnology. *Chemical Society reviews* **2006**, *35*, 1028–42.

(28) Van Blaaderen, A.; Vrij, A. Synthesis and characterization of colloidal dispersions of fluorescent, monodisperse silica spheres. *Langmuir* **1992**, *8*, 2921–2931.

(29) Ow, H.; Larson, D. R.; Srivastava, M.; Baird, B. a; Webb, W. W.; Wiesner, U. Bright and stable core-shell fluorescent silica nanoparticles. *Nano letters* **2005**, *5*, 113–7.

(30) Larson, D. R.; Ow, H.; Vishwasrao, H. D.; Heikal, A. a.; Wiesner, U.; Webb, W. W. Silica Nanoparticle Architecture Determines Radiative Properties of Encapsulated Fluorophores. *Chemistry of Materials* **2008**, *20*, 2677–2684.

(31) Herz, E.; Burns, A.; Bonner, D.; Wiesner, U. Large stokes-shift fluorescent silica nanoparticles with enhanced emission over free dye for single excitation multiplexing. *Macromolecular rapid communications* **2009**, *30*, 1907–10.

(32) Burns, A.; Sengupta, P.; Zedayko, T.; Baird, B.; Wiesner, U. Core/Shell fluorescent silica nanoparticles for chemical sensing: towards single-particle laboratories. *Small (Weinheim an der Bergstrasse, Germany)* **2006**, *2*, 723–6.

(33) Herz, E.; Marchincin, T.; Connelly, L.; Bonner, D.; Burns, A.; Switalski, S.; Wiesner, U. Relative quantum yield measurements of coumarin encapsulated in core-shell silica nanoparticles. *Journal of fluorescence* **2010**, *20*, 67–72.

(34) Burns, A. A.; Vider, J.; Ow, H.; Herz, E.; Penate-Medina, O.; Baumgart, M.; Larson, S. M.; Wiesner, U.; Bradbury, M. Fluorescent silica nanoparticles with efficient urinary excretion for nanomedicine. *Nano letters* **2009**, *9*, 442–8.

(35) Vallet-Regí, M.; Balas, F.; Arcos, D. Mesoporous materials for drug delivery. *Angewandte Chemie (International ed. in English)* **2007**, *46*, 7548–58.

(36) Fan, J.; Yu, C.; Gao, F.; Lei, J.; Tian, B.; Wang, L.; Luo, Q.; Tu, B.; Zhou, W.; Zhao, D. Cubic mesoporous silica with large controllable entrance sizes and advanced adsorption properties. *Angewandte Chemie (International ed. in English)* **2003**, *42*, 3146–50.

(37) De, M.; Ghosh, P. S.; Rotello, V. M. Applications of Nanoparticles in Biology. *Advanced Materials* **2008**, *20*, 4225–4241.

(38) Park, K.; Lee, S.; Kang, E.; Kim, K.; Choi, K.; Kwon, I. C. New Generation of Multifunctional Nanoparticles for Cancer Imaging and Therapy. *Advanced Functional Materials* **2009**, *19*, 1553–1566.

(39) Tan, W.; Wang, K.; He, X.; Zhao, X. J.; Drake, T.; Wang, L.; Bagwe, R. P. Bionanotechnology based on silica nanoparticles. *Medicinal research reviews* **2004**, *24*, 621–38.

(40) Wan, Y.; Zhao, D. On the controllable soft-templating approach to mesoporous silicates. *Chemical reviews* **2007**, *107*, 2821–60.

(41) Suteewong, T.; Sai, H.; Lee, J.; Bradbury, M.; Hyeon, T.; Gruner, S. M.; Wiesner, U. Ordered mesoporous silica nanoparticles with and without embedded iron oxide nanoparticles: structure evolution during synthesis. *Journal of Materials Chemistry* **2010**, *20*, 7807.

(42) Suteewong, T.; Sai, H.; Cohen, R.; Wang, S.; Bradbury, M.; Baird, B.; Gruner, S. M.; Wiesner, U. Highly aminated mesoporous silica nanoparticles with cubic pore structure. *Journal of the American Chemical Society* **2011**, *133*, 172–5.

(43) Nyffenegger, R.; Quellet, C.; Ricka, J. Synthesis of fluorescent, monodisperse, colloidal silica particles. *Journal of colloid and interface science* **1993**, *159*, 150–157.

(44) Hadd, A. G.; Lehmpuhl, D. W.; Kuck, L. R.; Birks, J. W. Chemiluminescence Demonstration Illustrating Principles of Ester Hydrolysis Reactions. *Journal of Chemical Education* **1999**, *76*, 1237.

(45) Garcia-Campana, A. *Chemiluminescence in analytical chemistry*; Garcia-Campana, A. M., Ed.; CRC Press, 2001, 2001.

(46) Monti, S.; Chiorboli, C. *The Exploration of Supramolecular Systems and Nanostructures by Photochemical Techniques*; Ceroni, P., Ed.; Springer Netherlands: Dordrecht, 2012; Vol. 78.

(47) Berera, R.; Van Grondelle, R.; Kennis, J. T. M. Ultrafast transient absorption spectroscopy: principles and application to photosynthetic systems. *Photosynthesis research* **2009**, *101*, 105–18.

CHAPTER 5

Tailoring Peroxyoxalate Chemiluminescence of Near-Infrared Bright Silica Nanoparticles using Polymer Additives *

5.0 Abstract

Peroxyoxalate chemiluminescence (POCL) is commonly used to develop sensitive and reliable hydrogen peroxide sensors due to high chemiluminescence (CL) quantum yields. In this report, we tuned POCL by polymer additives in ethyl acetate/1-hexanol solutions containing near infrared (NIR) dye-incorporated mesoporous silica nanoparticles (dMSNs). Addition of poly(*N*,*N*-dimethylaminoethyl methacrylate) (PDMAEMA) showed delays in POCL intensity maxima compared to the free dye of upto 125 seconds, while addition of polyethyleneimine (PEI) induced a continued emission for about 15 minutes and about 40-fold increase in total photon counts. The ability to tune the POCL reaction kinetics makes dMSN – polymer additive systems attractive for sensitive hydrogen peroxide NIR detection over extended time scales.

* Prepared for submission as: S. K. Iyer, K. Sarakune, J. Werner, H. Sai and U. B. Wiesner." Tailoring Peroxyoxalate Chemiluminescence of Near-Infrared Bright Silica Nanoparticles using Polymer Additives"

5.1 Introduction

Peroxyoxalate chemiluminescence (POCL) has been the most desired method for analytical detection and quantification of fluorescent derivative compounds and hydrogen peroxide.[1–4] Amongst all existing chemiluminescent (CL) methodologies, POCL is the most efficient non-enzymatic CL reaction, with CL quantum yields reported in the range of 22-27% when reactions are carried out under optimum conditions.[5,6] POCL involves emission of energy in the form of light, by fluorophores that are electronically excited as a result of a chemical reaction involving oxalate diesters and hydrogen peroxide. This provides a platform for detecting hydrogen peroxide for diagnosis of diseases, enzymatic reactions involving oxidases and explosives.[2,4,7–11]

The POCL reaction proceeds in three key steps as is summarized in Figure 5.1. As a first step, a sterically bulky oxalate diester reacts with hydrogen peroxide to produce 1,2-dioxetanedione, a key intermediate molecule (Figure 5.1a). As a next step (Figure 5.1b) decomposition of 1,2-dioxetanedione into carbon dioxide converts the chemical energy of this intermediate into electronic excitation energy that excites the fluorophore. The energy transfer occurs through a charge transfer complex with the fluorophore via chemically initiated electron exchange luminescence (CIEEL).[12,13] Finally, the excited species emits energy in the form of light (Figure 5.1c) which can be tuned through the entire visible to near-infrared (NIR) spectrum depending on the fluorophore used. Each of these steps depends on different parameters hence optimization of POCL detection is an extremely complex process.

The rate determining step of POCL is the formation of 1,2-dioxetanedione, thus efforts to tune the kinetics have to be focused on this step.[14] Formation of 1,2-dioxetanedione occurs due to nucleophilic attack by hydrogen peroxide on one of the oxalate carbonyl carbons. To ensure the formation of this reactive intermediate, diaryloxalate esters with strongly electron withdrawing groups are typically used as the reactant precursor for the formation of 1,2-dioxetanedione. Typical oxalates used are bis(2-cyclopentyloxy-3,5,6-trichlorophenyl)oxalate (CPPO) and 2,4,6-trichlorophenyl oxalate (TCPO).[15–17] POCL reactions are typically carried out in mildly polar organic solvents due to high reactivity of the diaryloxalate esters in aqueous solutions.[6,18,19] The presence of a base (e.g. potassium hydroxide or benzyltrimethylammonium hydroxide) or a nucleophilic catalyst (e.g. imidazole, pyridine) increases the rate of formation of 1,2-dioxetanedione.[6,20] Addition of these reagents results in acceleration and increase of CL intensity for free dyes, which requires fast detection methods. Therefore, research efforts need to be directed towards prolonging CL to allow easy detection. Despite the complexity in the formation of 1,2-dioxetanedione mentioned above, additives that decelerate its formation may provide a simple means to prolong or delay emission thus simplifying the detection of CL.

Depending on the wavelength of interest, appropriate fluorophores can be used for desired applications. It has been shown in previous studies that covalent encapsulation of organic fluorophores in silica matrix tunes the photophysics towards obtaining high quantum efficiency compared to the parent free dye.[21,22] We have shown that, by incorporating a NIR absorber dye ADS832WS as a CL probe in a

mesoporous silica nanoparticle, the non-radiative rate of decay is reduced, hence, increasing the CL brightness.[23] This provides a good platform for bright NIR CL probes which increases the signal to noise ratio and makes detection easier.

In this report, we present a way to tune the kinetics of POCL through simple polymer additives. We used dye-encapsulated mesoporous silica nanoparticles (dMSNs) with average size of about 60 nm as a bright model system for studying CL. The dMSNs were combined with different polymer additives in the form of polybases in an ethyl acetate/1-hexanol solvent mixture to study the tunability of the CL process. We show that using different polyamines, the CL can be delayed while exhibiting a substantial increase in photon yield compared to the free dye. Finally, NMR studies provide a clue as to the possible molecular mechanisms responsible for observed variations in POCL kinetics.

5.2 Experimental section

Chemicals and Materials

All chemicals were used as purchased. ADS832WS dye (American Dye Source, Inc.) was dissolved in dimethyl sulfoxide (DMSO, anhydrous > 99%, Sigma Aldrich). The dye solution was conjugated with (3-isocyanatopropyl)triethoxysilane (ICPTS, ≥ 95%, Gelest Inc.). To synthesize nanoparticles, hexadecyltrimethylammonium bromide (CTAB, Sigma), ethyl acetate (ACS grade, Mallinckrodt Chemicals), ammonium hydroxide (NH_4OH, 29% Fisher Scientific) tetraethyl orthosilicate (TEOS, ≥ 99%, GC, Aldrich) and deionized water (DI-H_2O, Milli-Q, 18.2 MΩ-cm) were used. The particles were then suspended in 1- hexanol (analytical standard, Sigma Aldrich). To carry out CL measurements bis-(2-carbopentyloxy-3,5,6-trichlorophenyl)oxalate

(CPPO, Sigma Aldrich) was dissolved in ethyl acetate (ACS grade, Mallinckrodt Chemicals). Potassium hydroxide (KOH, AR (ACS) grade, Mallinckrodt Chemicals) was dissolved in hydrogen peroxide (H_2O_2, 30% aqueous, AR (ACS) grade, Mallinckrodt Chemicals) to initiate CL reaction. Polyethyleneimine (PEI, 20 kg/mol, Sigma Aldrich) was used as an additive. The other additives poly(isoprene–*block*–*N*,*N*-dimethylaminoethylmethacrylate) (PI-*b*-PDMAEMA) with molar masses of 19 kg/mol (PI-*b*-PDMAEMA-1) and 28 kg/mol (PI-*b*-PDMAEMA-2), as well as the respective homopolymers, polyisoprene (PI) and poly(*N*,*N*-dimethylaminoethylmethacrylate) (PDMAEMA) with molar masses of 10 kg/mol and 5 kg/mol, respectively, were synthesized in lab (see polymer synthesis).

Synthesis of Mesoporous Silica Nanoparticles

To 1 mL of ADS832WS (4.5 mM in DMSO) solution, neat ICPTS (56 µl) was added in a vial and stirred at room temperature in glove box under nitrogen atmosphere for 16 hours to obtain dye-silane conjugate. The resultant dye conjugate was used for subsequent synthesis of dye-incorporated mesoporous silica nanoparticles.

Dye-incorporated mesoporous silica nanoparticles (dMSNs) were synthesized via a sol-gel method with CTAB as a template. In a 100 mL round bottom flask, 40 mL DI-H_2O, 2 mL of 54.8 mM CTAB solution and 352 µl ethyl acetate were added. After 3 minutes, 800 µl of NH_4OH was added. After 1 minute, 176 µl of the dye conjugate solution (from above) was added. After 1 minute, 200 µl of TEOS was added. After 5 minutes, 14.68 mL DI-H_2O was added. After 14 minutes, hydrochloric acid (2.0 M) was added until the solution was neutralized. To remove unreacted chemicals, the particle solution was cleaned by centrifugation and re-suspended in DI-H_2O three

times. To remove CTAB, 1 mL of glacial acetic acid (95%, v/v) was added per 20 mL of particle solution and left to stir for 1 hour. To remove the acid and CTAB, the particle solution was washed by DI-H_2O and ethanol solutions via centrifugation and particles were finally re-suspended in ethanol for storage.[24,25]

Prior to carrying out CL measurements, the particles suspended in ethanol were transferred to 1-hexanol via centrifugation. All steps were carried out at room temperature.

Polymer synthesis

Synthesis of polymers poly(isoprene-*block*-*N*,*N*-dimethylaminoethylmethacrylate) (PI-*b*-PDMAEMA), polyisoprene (PI) and poly(*N*,*N*-dimethylaminoethyl methacrylate) (PDMAEMA) were performed via living anionic polymerization according to methods described in previous work.[26,27,28] Table D.1 summarizes(supplementary information) the molar masses and polydispersity indices (PDIs) of all polymers used in this study.

Methods

Chemical Preparation and critical micelle concentration (CMC) measurements:

Dynamic light scattering (DLS) was carried out on a Malvern Nano-SZ operated at 20 ^{o}C, to determine the CMC of the block copolymers.[29] Stock solutions of PI-*b*-PDMAEMA-1 and PI-*b*-PDMAEMA-2 were prepared in 1-hexanol at 7.6 mg/mL and 6.6 mg/mL, respectively. CMC measurements were carried out in an ethyl acetate/1-hexanol solvent mixture, the volume of each measured solution was adjusted to 1.4 mL (1.2 mL ethyl acetate and 0.2 mL 1-hexanol). To this end six solutions at concentrations of 0.05 mg/mL, 0.075 mg/mL, 0.1 mg/mL, 0.3 mg/mL, 0.6 mg/mL and 0.9 mg/mL were prepared for PI-*b*-PDMAEMA-1, and concentrations of 0.04 mg/mL,

0.08 mg/mL, 0.25 mg/mL, 0.045 mg/mL, 0.6 mg/mL and 0.9 mg/mL for PI-*b*-PDMAEMA-2.

Each size measurement was carried out three times and the diameter reported was the average diameter obtained from number percent statistics. After obtaining the sizes at the different polymer concentrations, a graph of concentration versus size was plotted (Figure S1) to determine the CMC of the block copolymers as described elsewhere.[29]

Absorbance matching and CL measurements:

Equivalent dye concentrations of free ADS832WS dye and dMSNs solutions were prepared in ethyl acetate/1-hexanol containing CPPO, by absorbance matching the nanoparticle solution to a solution of the dye with known concentrations on a UV-visible spectrometer (Varian Cary 5000 UV-Vis-NIR). For this purpose, CPPO (2.2 mM in ethyl acetate, 600 µl) and 1-hexanol (50 µl) were mixed in 3 mL plastic disposable cuvettes (PMMA), and baseline corrected for in the UV-visible spectrometer. ADS832WS (26 µM in 1-hexanol, 50 µl) was added to the sample cuvette to give a dye:oxalate ratio of 1:1050, and the absorbance was recorded between 750– 900 nm. After that, to the additional cuvettes dMSNs in 1-hexanol was added until the absorbance of the resulting solution matched the absorbance of the ADS832WS dye solution. These solutions were subsequently used for CL measurements.

Stock solutions of the polymer additives were prepared in 1-hexanol. Aliquots of PI-*b*-PDMAEMA-1 (7.1 mg/mL), PI-*b*-PDMAEMA-2 (7.0 mg/mL), polyisoprene 10 kg/mol (5.5 mg/mL, PI), polydimethylaminoethylmethacrylate 5 kg/mol (5 mg/mL,

PDMAEMA) and polyethyleneimine 20 kg/mole (3.5 mg/mL, PEI) were added as described in Tables 5.1 – 5.4 to nanoparticle containing solutions from absorbance matching. Please note, the final ethylacetate to 1-hexanol solvent ratio was maintained at 6:1 volume ratio.

Immediately before CL measurements, a solution of KOH in hydrogen peroxide (0.8 mg/mL KOH in 30% hydrogen peroxide, 6µl) was added to the dye solution or nanoparticle solution with or without additive from absorbance matching. The resulting solution was mixed for 15 seconds before its emission was measured at 832 nm over periods of upto 25 minutes on a spectrofluorometer (Photon Technologies International Quantamaster).

The total photons emitted during CL were calculated by integrating the area under the emission versus time curves. For each measurement the background photon counts were measured and subsequently subtracted from the CL measurements to calculate the total emitted photons. For the free dye, dMSN (with no additives) and dMSN with polymer systems PI-*b*-PDMAEMA-1, PI-*b*-PDMAEMA-2, PI and PDMAEMA the integrated area under the curve was calculated between the limits of 0 – 500 seconds. For dMSNs with PEI as additive, the integrated area under the curve was calculated from 0 – 1500 seconds.

^{1}H-NMR Spectroscopy:

The chemical influence of the polymer additives was investigated using ^{1}H-NMR spectrometry. CPPO was dissolved in ethyl acetate followed by addition of aliquots of stock solutions of PDMAEMA and PEI in 1-hexanol. The final volume ratio of ethyl acetate/1-hexanol solvent mixture was maintained at 6:1, by further addition of 1-

hexanol to each sample. The final concentrations of PDMAEMA and PEI prepared for ^{1}H-NMR spectrometry, are shown in Tables 5.3 and 5.4, respectively. After two hours in the ethyl acetate/1-hexanol mixture, the solvents were evaporated completely and the resulting solid dissolved in deuterated chloroform (Chloroform-d, 99.8 atom% D, Aldrich) at a concentration of 15-20 mg/mL. ^{1}H-NMR spectra were recorded on a Varian Mercury spectrometer at 300 MHz.

5.3 Results and Discussion

In a previous study we compared CL profiles of free parent dye (ADS832WS) and dye incorporated mesoporous silica nanoparticles (dMSNs) suspended in ethyl acetate/1-hexanol solvent mixture (final volume ratio of 6:1).[23] Vials containing the dioxalate ester CPPO, were dissolved in a solvent mixture of ethyl acetate/1-hexanol as described in the experimental section. ADS832WS and dMSNs were suspended in ethyl acetate/1-hexanol solvent mixture containing CPPO, such that the molar ratio of dye to CPPO was maintained at 1:1050. The dMSN solution was absorbance matched to free parent dye solutions followed by addition of H_2O_2/KOH to the sample solution for quantitative comparisons. The temporal evolution of CL brightness was monitored at the CL peak maximum of 832 nm. The dMSN solutions showed a four-fold enhancement in CL brightness compared to free parent dye solutions. The time point of CL as measured at the intensity maximum (t_{max}) and its duration measured as the half width at half maximum of the emission signal, which we referred to as half life, $t_{1/2}$, of dMSNs were determined to be 30 seconds and 100 seconds, respectively, for the conditions investigated. In comparison, the free dye showed a t_{max} at 25 seconds and a $t_{1/2}$ of 45 seconds. Additionally, the area under the curve for the CL of dMSNs

as calculated over the entire time duration of CL emission, resulted in an 18-fold increase in total photons emitted compared to free parent dye. Based on these earlier findings, we decided that the 60 nm diameter dMSNs provided an appropriate platform to investigate the effects of polymer additives on CL behavior.

5.3.1 Block copolymer additives

Block copolymers are known to form micelles above a critical micelle concentration (CMC) in polar solvents.[29] First we investigated the feasibility of affecting CL in the POCL system by trapping reactants in the hydrophobic core of block copolymer micelles. For this purpose, dynamic light scattering measurements were carried out to first determine the CMC of each of these polymers in the ethyl acetate/1-hexanol solvent system in which POCL was studied (see supporting information, Figure S1).[29] On increasing the concentration of the block copolymer at a relatively well defined point a significant increase in hydrodynamic radius was observed which we interpreted as the CMC at which unimers start to form micelles. The CMC was determined to be around 0.6 mg/mL and 0.5 mg/mL for 19 kg/mol PI-*b*-PDMAEMA (PI-*b*-PDMAEMA-1) and a 28 kg/mol PI-*b*-PDMAEMA (PI-*b*-PDMAEMA-2), respectively.

The effect of PI-*b*-PDMAEMA on CL was investigated by adding PI-*b*-PDMAEMA at concentrations below, at and above the CMC to mixtures of absorbance matched dMSN solutions containing CPPO before the addition of KOH/H_2O_2 and subsequent recording of the CL spectra.

For PI-*b*-PDMAEMA-1, at concentration of 0.05 mg/mL, the CL intensity peak maximum was observed at t_{max} of 75 seconds with a $t_{1/2}$ of 120 seconds as shown

in Figure 5.2a, while the brightness remained as high as for dMSNs without additives. On increasing the block copolymer concentration to 0.5 mg/mL, the t_{max} shifted to 95 seconds; however the CL intensity brightness dropped by about 60% compared to the brightness of dMSNs without additives. The $t_{1/2}$ shifted to 150 seconds. At concentrations of 0.9 mg/mL, no CL emission was observed.

Similar measurements were carried out for dMSNs by adding PI-*b*-PDMAEMA-2. In Figure 5.2b, for a concentration of 0.04 mg/mL, the CL intensity maximum peaks at t_{max} of 100 seconds, with a $t_{1/2}$ of 165 seconds. On increasing the concentration of block copolymer to 0.4 mg/mL and beyond the CMC to 0.6 mg/mL no CL was observed.

Results of the CL time profiles of dMSNs with block copolymer additives at concentrations below their CMC are summarized in Table 5.1. Addition of block copolymers to absorbance matched dMSNs below their CMC did not show any negative influence on the CL intensity compared to dMSN solutions without additives. At these block copolymer concentrations, we noticed the CL intensity maximum peak was delayed relative to dMSNs by 45 and 70 seconds for PI-*b*-PDMAEMA-1 and PI-*b*-PDMAEMA-2, respectively. On comparing the half life of these systems to free dye (45 seconds), $t_{1/2}$ for PI-*b*-PDMAEMA-1 increases by 75 seconds, whereas for PI-*b*-PDMAEMA-2 it increases by 120 seconds. Moreover, based on area under the curve analysis over the entire time scale (0 – 500 seconds), the total number of photons released for these additives shows an approximately 17-fold increase compared to the free dye, which is close to the 18-fold increase observed for dMSNs as compared to free dye.

From the above results, we concluded that while the idea of affecting CL in the POCL system by trapping reactants in the hydrophobic core of block copolymers did not work, polymer additives seem to have a significant effect. In order to further investigate this as the next step we turned our attention to homopolymer additives.

5.3.2 Homopolymer additives

In order to better understand the observed CL effects upon block copolymer addition, the influence of each constituting block was investigated by addition of the respective homopolymer to the POCL reaction solution. Thus, chemiluminescence of dMSNs was measured at varying concentrations of poly(isoprene) (PI, 10 kg/mol) and poly(*N*,*N*-dimethylaminoethylmethacrylate) (PDMAEMA, 5 kg/mol).

On addition of PI at different concentrations, the CL profiles showed no significant alterations as compared to the parent particle solution (Figure 5.3a). In contrast, addition of PDMAEMA at various concentrations showed both a delay and a decrease in CL. At a concentration of 0.06 mg/mL of PDMAEMA, the t_{max} shifted to 150 seconds with a $t_{1/2}$ of 250 seconds, and the maximum intensity dropped by ~ 55% compared to the CL profile of additive free dMSN solutions (Figure 5.3b). On increasing the concentration of PDMAEMA to 0.09 mg/mL, we noticed a further decrease in the CL intensity, with a shift of t_{max} to 165 seconds with a $t_{1/2}$ of 275 seconds. On further increasing the PDMAEMA concentration to 0.15 mg/mL CL pretty much dropped to levels of the free dye. The area under the curve from the CL time profiles, which corresponds to the total photons released during CL, showed about 17-fold increase (0.06 mg/mL PDMAEMA) compared to the free dye, similar to dMSN solutions without PDMAEMA. These results indicate that the polybase

PDMAEMA is responsible for the delay and drop in CL, suggesting that the effects are due to chemical interactions. On first sight such an influence of a polybase with tertiary amines is a surprising result. Based on previous work tertiary amines like triethylamine acted as nucleophilic catalysts, accelerating and increasing CL intensity.[30] Based on these results for PDMAEMA, we extended the study to a different polybase i.e. polyethyleneimine (PEI), to further investigate the chemical influence of polybases on CL of dMSNs.

On addition of PEI to the dMSN solutions, we observed a slightly different effect on CL profile compared to PDMAEMA. At a PEI concentration of 0.02 mg/mL the CL peaked as soon as the reaction started, however, it lasted for about 900 seconds (15 minutes) with a $t_{1/2}$ of 375 seconds (Figure 5.4). On increasing PEI concentration to 0.05 mg/mL, a CL maximum appeared at 125 seconds while the overall intensity dropped by ~ 50% compared to solutions containing only dMSNs (with no additives). At high concentrations of 0.24 mg/mL practically no significant CL was observed.

The effects of polybases on the CL time profiles of dMSNs as compared to CL of free dye without additives are summarized in Table 5. 2. The results demonstrate that polymer additives are very effective in enhancing CL of dMSNs, in particular in prolonging CL emission. Similar effects on the CL emission profiles were observed upon polybase addition to free parent dye solutions, (see supplementary information, Figure S2), albeit at much lower emission intensities. The effects are thus most dramatic when particle incorporation and polymer additive effects together are compared to the CL of free parent dye. For example, area under the curve analysis for CL profiles of dMSNs upon the addition of PDMAEMA (0.06 mg/mL) and PEI (0.02

mg/mL) showed a 17-fold and 40-fold increase, respectively, in number of photons released compared to the free dye. Overall these results provide useful tools how to effectively tune CL time profiles towards desired outcomes.

5.3.3 Chemical influence of polybases

Previous work has suggested that increase in the base/nucleophile concentration causes a decrease in the concentration of the oxalate diester hence causing a drop in CL intensity.[14] This indicates that the base/nucleophile might be interacting or changing the chemical composition of the oxalate diester. To investigate the chemical composition changes of oxalate diester-polybase solutions we carried out ^{1}H-NMR spectroscopy.

As a first step we looked at the ^{1}H-NMR spectrum of CPPO, which was first dissolved in ethylacetate/1-hexanol solvent system and after solvent evaporation, was re-dissolved in deuterated chloroform. The ^{1}H-NMR spectrum in Figure 5.5a shows three aromatic proton peaks at δ: 7.63 ppm (s, H^{C}), 7.67 ppm (s, H^{B}) and 7.71 ppm (s, $2H^{A}$), which correspond to the aromatic protons of the leaving group. Another peak at δ = 11.17 ppm was observed and assigned to the phenolic proton. Two triplets at δ = 4.37 ppm (coupling constant: 7.5 Hz) and δ = 4.44 ppm (coupling constant: 6 Hz) can be assigned to the oxygen-adjacent CH_2 protons of the pentyl ester on the aromatic groups associated with two different molecules. The ^{1}H-NMR spectrum of CPPO dissolved in deuterated chloroform should show an aromatic peak at 7.71 ppm and an aliphatic peak at 4.44 ppm. However, due to the instability of CPPO in polar solvents, the solvent 1-hexanol may act as a nucleophile resulting in the formation of the asymmetric oxalate ester 3,4,6-trichloro-2-(pentyloxycarbonyl)phenyl-1-hexyloxalate

(Figure 5.5b).[6,18] As a result of this equilibrium reaction between CPPO and 1-hexanol, two other compounds with aromatic protons arise helping to understand the various peaks observed in the ^{1}H-NMR spectrum. The peak at 7.71 ppm corresponds to CPPO (compound I, H^{A}), while the peaks at 7.67 ppm and 7.63 ppm can be assigned to 3,4,6-trichloro-2-(pentyloxycarbonyl)phenyl-1-hexyloxalate (compound II, H^{B}) and 2-carbopentyloxy-3,5,6-tricholorphenol (compound IV, H^{C}), respectively. The presence of 2-carbopentyloxy-3,5,6-trichlorophenol is also confirmed by the presence of the phenolic peak (H^{D}) at 11.17 ppm. These results qualitatively suggest that in presence of 1-hexanol, CPPO forms small amounts of 3,4,6-trichloro-2-(pentyloxycarbonyl)phenyl-1-hexyloxalate and 2-carbopentyloxy-3,5,6-tricholorphenol. Furthermore, the asymmetric oxalate ester can undergo a second transesterfication reaction to form dihexyloxalate. However, the ^{1}H-NMR spectrum does not indicate this successive reaction to take place.

Following this result, we investigated the effect of polybases on the CPPO molecule. The concentrations of CPPO in ethyl acetate and 1-hexanol were kept identical for relevant comparative studies. We carried out measurements for different PDMAEMA and PEI concentrations. Figure 5.6, shows the effect of increasing the PDMAEMA concentration on the ^{1}H-NMR spectrum of CPPO. Based on the peak assignments, we noticed that the peak for compound I (H^{A}) decreased and the peaks corresponding to compound II (H^{B}) and compound IV (H^{C} and H^{D}) increased on increasing PDMAEMA concentration. The amounts of these three compounds were quantified using signal integrations. As mentioned above, proton peaks at 7.63 and 11.17 ppm correspond to the aromatic proton (H^{C}) and phenolic proton (H^{D}),

respectively, of compound IV. We noticed the integrals for these two proton peaks to be identical, thus corroborating the assignments of the proton peaks for compound IV.

In the ^{1}H-NMR spectrum of CPPO without additive (0 mg/mL), we observed that the integrals corresponding to peaks H^{B} and H^{C} were equivalent. On increasing the PDMAEMA concentration, however, we noticed that the H^{C} peak was greater than H^{B} peak, suggesting the occurrence of the second equilibrium reaction as shown in Figure 5.5b. The mixed oxalate, i.e. compound II, still has an aromatic leaving group, which can further react with 1-hexanol to form dihexyloxalate (compound III). This second reaction can explain the mismatch of the integrals of the two peaks for H^{B} and H^{C} upon addition of PDMAEMA to the system.

The presence of the dihexyloxalate cannot be detected selectively from ^{1}H-NMR data, since the peak appears at approximately 4.3 ppm where it overlays with peaks corresponding to pentyl esters on the aromatic groups. However, its presence explains the discrepancy in the integrals of the aromatic protons H^{B} and H^{C}.

In order to quantify our findings, we calculated the mole fractions of compound I, compound II and compound III at different PDMAEMA concentrations. As mentioned above, dihexyloxalate cannot be detected directly from ^{1}H-NMR. However, the scheme in Figure 5.5b shows that one mole of compound II forms along with one mole of compound IV, and compound III forms with 2 moles of compound IV. The peak H^{B} corresponds to compound II, thus in an indirect way based on the integrals obtained for compound IV and compound II, we calculated the amount of compound III produced during the reaction (see supporting information). The resulting

relative ratios of the three oxalate diesters as a function of the concentration of the added polybase PDMAEMA are tabulated in Table 5. 3.

In the absence of PDMAEMA, CPPO breaks down to give a small amount of compound II and a negligible amount of compound III. On adding 0.06 mg/mL of PDMAEMA, the relative amount of compound I decreased significantly and compound II became the major oxalate component of the system. At this concentration of the polybase compound III was present in similar quantities as compound I. At 0.09 mg/mL of PDMAEMA, compound I was almost completely converted into compound II and III, with the ratio of compound II to III being approximately 2:1. Finally, at 0.15 mg/mL, CPPO is completely converted to compound II and compound III while the ratio between these two compounds stayed roughly the same.

Based on the ^{1}H-NMR data, it is obvious that on increasing the concentration of PDMAEMA, the equilibria of the two reactions were shifted towards the complete disappearance of compound I and the formation of compound II as the major oxalate of the system, next to compound III that was present at half of the molar amount of compound II.

The ^{1}H-NMR results for PEI addition are shown in Figure 5.7 and are summarized in Table 5. 4. On adding 0.02 mg/mL PEI, we noticed only a slight increase in compound II as compared to the system without PEI. On increasing the PEI concentration to 0.05 mg/mL, small amounts of compound III were formed, with compound I still being the major oxalate component. As more PEI was added, the relative concentration of compound I dropped and at 0.24 mg/mL, compound II and compound III represented the major components of the system with a ratio between

compounds I, II and III of 1:2:2. The ^{1}H-NMR studies for PEI suggest that, at PEI concentrations up to 0.05 mg/mL, the equilibrium favors compound I, while at higher PEI concentrations, compounds II and III are the major components.

From the ^{1}H-NMR data for the addition of the two polybases, we noticed that CPPO underwent chemical modification to form a mixture of oxalate diester molecules. Comparison of the ^{1}H-NMR data for the two polybases suggests that even for low PDMAEMA concentrations, the chemical equilibria are shifted towards compound II, whereas for PEI at similar concentrations, the CPPO stays the major oxalate present. At higher concentrations, both polybases shift the equilibrium away from compound I, towards compound II and compound III. However, the ratios between compounds II and III at this point stayed significantly different.

The rate of formation of 1,2-dioxetanedione upon the addition of KOH/H_2O_2 depends on the type of oxalate diesters present in the solution. Figure 5.8 summarizes the three reactions forming 1,2-dioxetanedione from the different oxalate diesters I, II, and III found in the reaction mixtures. The formation of 1,2-dioxetanedione from compound II in presence of alkaline hydrogen peroxide should be slower than from compound I, since the rate limiting step in the formation of 1,2-dioxetanedione is the release of the aliphatic hexanolic group, which is a worse leaving group than the phenolic group due to the higher pKa of 1-hexanol compared to the substituted phenol. The dihexyloxalate has two hexanolic groups and does not form 1,2-dioxetanedione as in this case, both ester sides on the molecule are occupied with poor leaving groups.

According to the different rates of formation of 1,2-dioxetanedione from the different oxalate diesters (compound I, compound II and compound III), differences in

CL behavior are expected for the mixtures with different concentrations of these compounds. Thus, upon addition of PDMAEMA at concentrations of 0.06 mg/mL and 0.09 mg/mL, the CL intensity maximum peaked at 150 seconds and 165 seconds, respectively, while for PEI at 0.05 mg/mL, the CL intensity maximum peaked at 125 seconds. Compared to free dye, this corresponds to a delay in CL for PDMAEMA and PEI by a factor of 6 and 5, respectively. As suggested by ^{1}H-NMR spectroscopy, at these base concentrations we observe the equilibrium shift towards the formation of compound II, which as shown in Figure 5.8 is expected to slow the rate of formation of 1,2-dioxetanedione, consistent with the observed delay in the CL peak maximum. At high polybase concentrations, we do not observe any significant CL emission for both polybases, despite the presence of compound II as shown by the respective ^{1}H-NMR spectra. This inconsistency maybe attributed to the fact that at high polybase concentrations, 1,2-dioxetanedione might be interacting with the polybases thus making it unavailable for any fluorophore interaction. Unfortunately, due to the absence of protons and short lifetime of 1,2-dioxetanedione it is difficult to carry out ^{1}H or ^{13}C-NMR spectroscopy to record any such interactions. For low PEI concentration (0.02 mg/mL) the CL is prolonged for about 15 minutes. From the ^{1}H-NMR spectroscopy results we observe compound I to be six times greater than compound II suggesting that the kinetics should still be fast. Besides chemically modifying the oxalate diester, PEI might thus be physically influencing the effect of CL. Further investigations are thus needed to fully understand the effects of PEI at low concentrations.

5.4 Conclusions

In this report, we presented new polymer additives in the form of polybases like PDMAEMA and PEI that can be used to effectively prolong the emission of CL reactions. Compared to other additives like triethylamine, which accelerates the CL reactions, by carefully controlling the concentrations of these polymers the reaction rates can be decelerated such that the CL brightness of dMSN is maintained along with the desired delay or prolonging of CL. ^{1}H-NMR showed that polybases PDMAEMA and PEI induce chemical modifications of CPPO, thus affecting the rate of formation of 1,2-dioxetanedione. These additives provide great potential towards tailoring CL based detection of hydrogen peroxide for example from explosives or in the diagnosis of diseases. Furthermore by devising a system containing all the CL reactants for example in polymer capsules, additives may also be used for developing CL based assays which are simple and cost effective as they may not require fast detection schemes.

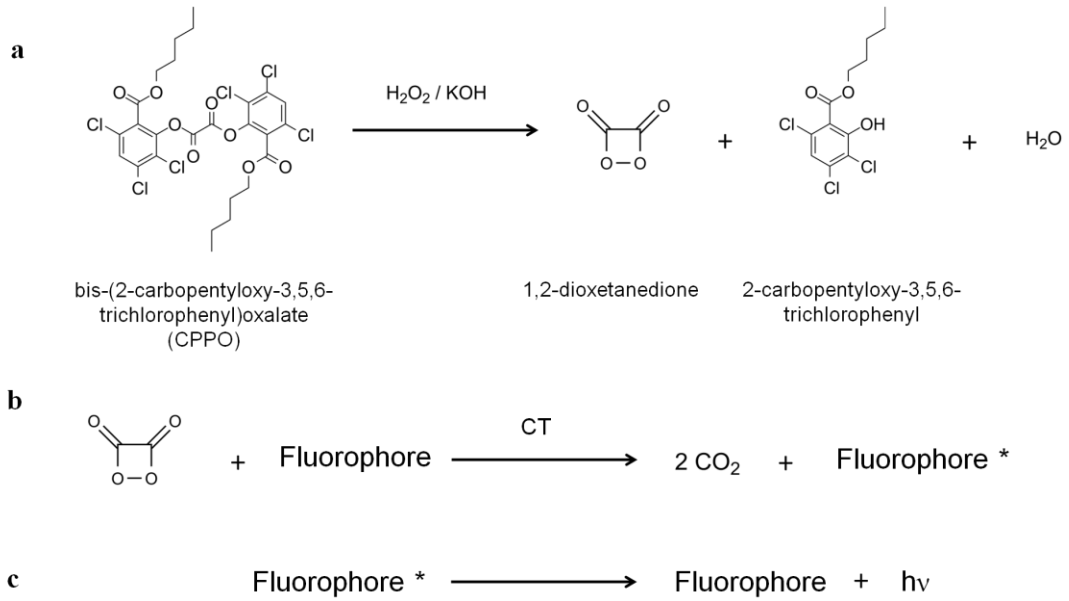

Figure 5.1. Overview of peroxyoxalate chemiluminescence (POCL) reaction process. (a) In presence of basic hydrogen peroxide, the oxalate diester (CPPO) forms a highly reactive four membered ring intermediate 1,2-dioxetanedione along with 2-carbopentyloxy-3,5,6-tricholorphenol as by-product. (b) The intermediate 1,2-dioxetanedione, forms a charge transfer (CT) complex with the fluorophore, which, upon decomposition of 1,2-dioxetanedione yields carbon dioxide and an electronically excited fluorophore. (c) As a final step, the excited fluorophore relaxes to the ground state via emission of light.[6]

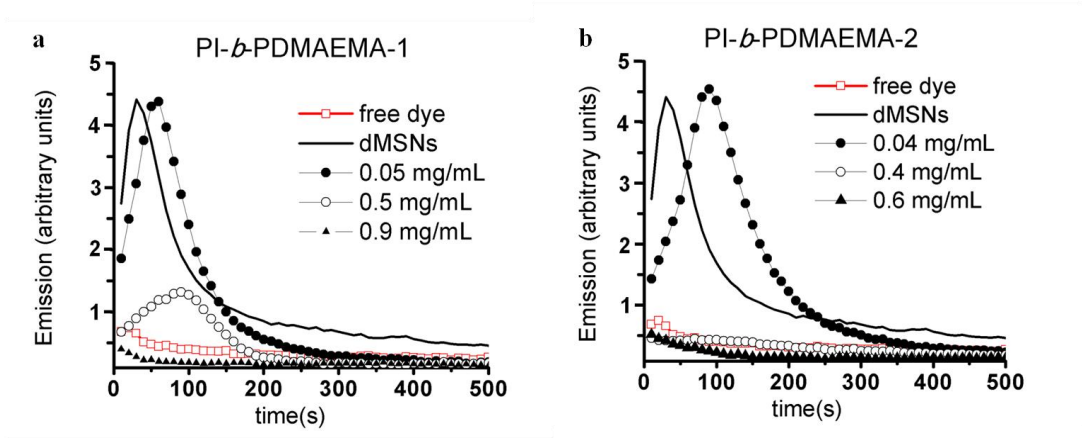

Figure 5.2. Chemiluminescence emission profiles of dMSNs on addition of (a) 19 kg/mol PI-*b*-PDMAEMA (PI-*b*-PDMAEMA-1) and (b) 28 kg/mol PI-*b*-PDMAEMA (PI-*b*-PDMAEMA-2) below (—●—), at (—○—) and above the CMC (—▲—).

Table 5.1. Effect of block copolymer additives on CL emission profiles of dMSNs below CMC

Sample	t_{max} (s)	I max (counts)	Enhancements (normalized to free dye)	half life ($t_{1/2}$, s)	time delay compared to free dye (Δt, s)
free dye (no additives)	25	1240.0	1.0	45	-
dMSNs (no additives)	30	5030.0	4.0	100	5
PI-*b*-PDMAEMA-1 (0.05 mg/mL) and dMSNs	75	5200.0	4.0	120	45
PI-*b*-PDMAEMA-2 (0.04 mg/mL) and dMSNs	100	5240.0	4.1	165	75

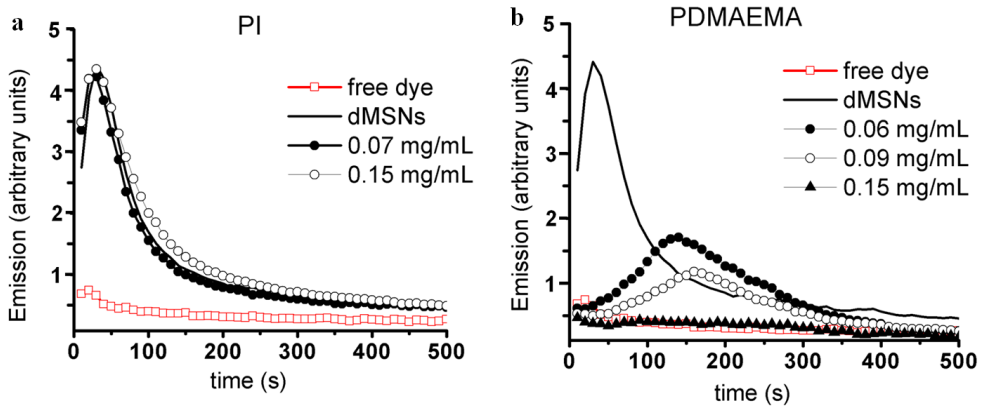

Figure 5.3. Chemiluminescence emission profiles of dMSNs on addition of (a) 10 kg/mol polyisoprene (PI) and (b) 5 kg/mol poly(2,2-dimethylaminoethylmethacrylate) (PDMAEMA) at different concentrations.

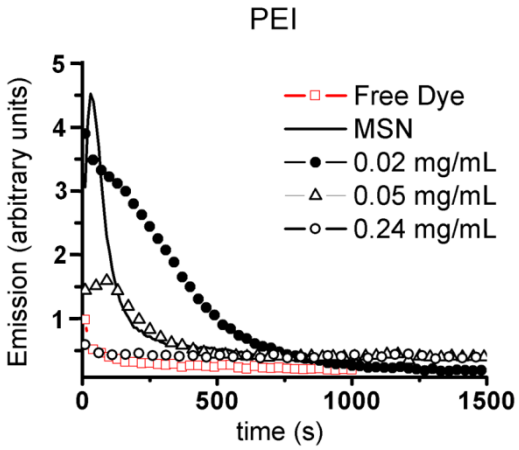

Figure 5.4. Chemiluminescence emission profiles of dMSNs on addition of PEI at different concentrations.

Table 5.2: Effect of polybase additives on CL emission profile of dMSNs

sample	t_{max} (s)	half life ($t_{1/2}$,s)	Total photon counts (area under the curve)	Total photon counts normalized to free dye
free dye (no additives)	25	45	56801.0	1.0
dMSNs (no additives)	30	5	1040420.0	18.3
PDMAEMA (0.06 mg/mL) and dMSNs	150	250	971297.1	17.1
PEI (0.02 mg/mL) and dMSNs	-	375	2312044.1	40.7

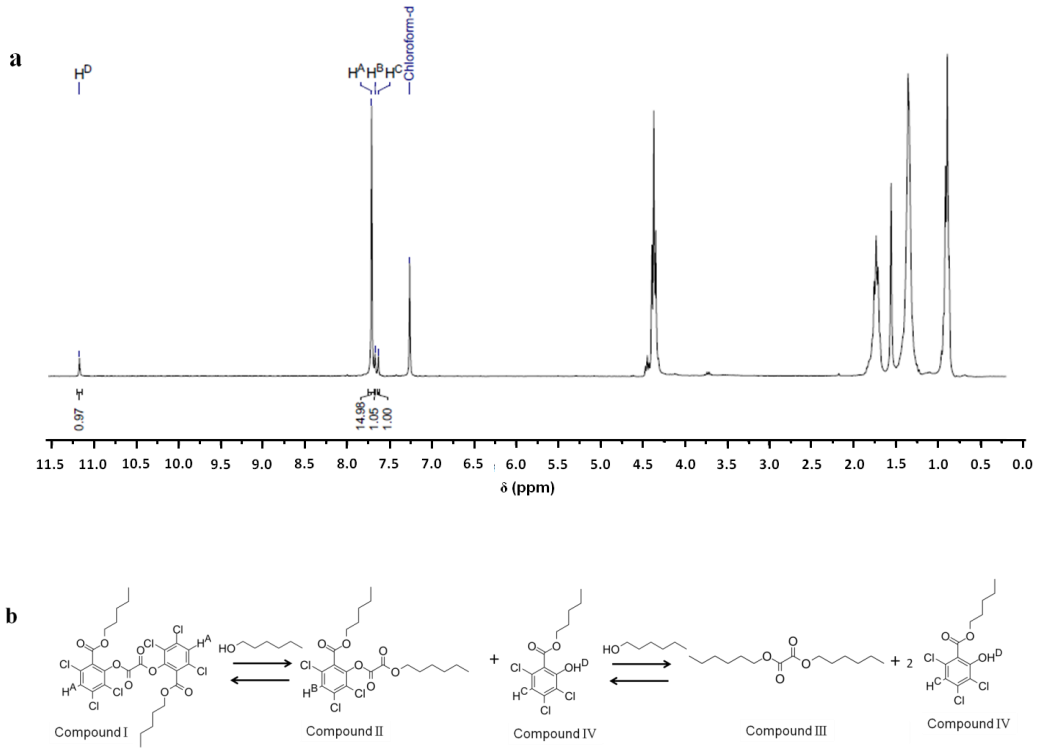

Figure 5.5. (a) ^{1}H-NMR spectrum of CPPO in presence of 1-hexanol. (b) Reaction scheme showing possible decompositions of CPPO in the presence of 1-hexanol.

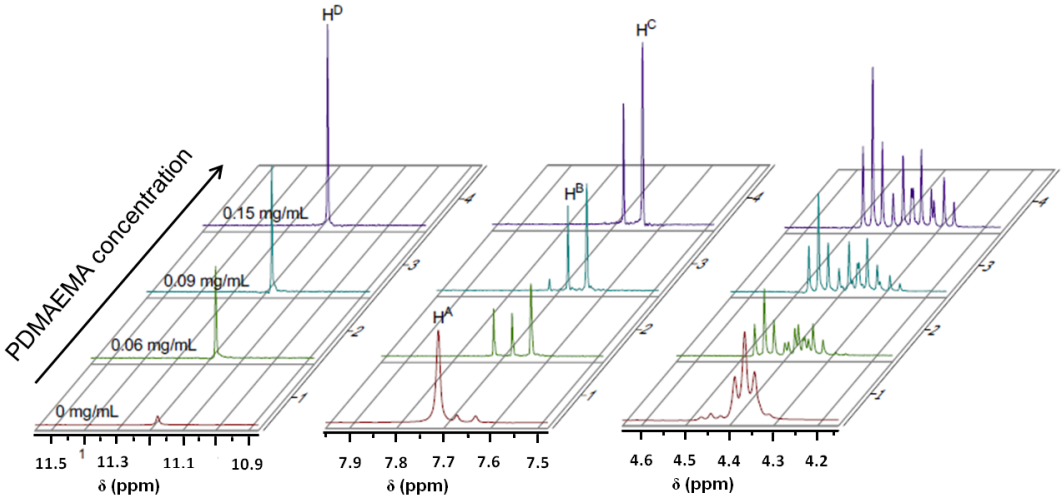

Figure 5.6. ^{1}H-NMR spctrum showing the effect of increasing the concentration of PDMAEMA on CPPO.

Table 5.3. Effect of PDMAEMA on molar ratios of oxalate diester molecules

Concentration of PDMAEMA	Molar ratio of compound I : II : III
0 mg/mL	0.86: 0.14 : 0
0.06 mg/mL	0.24 : 0.48 : 0.28
0.09 mg/mL	0.05 : 0.67 : 0.29
0.15 mg/mL	0.00 : 0.66 : 0.34

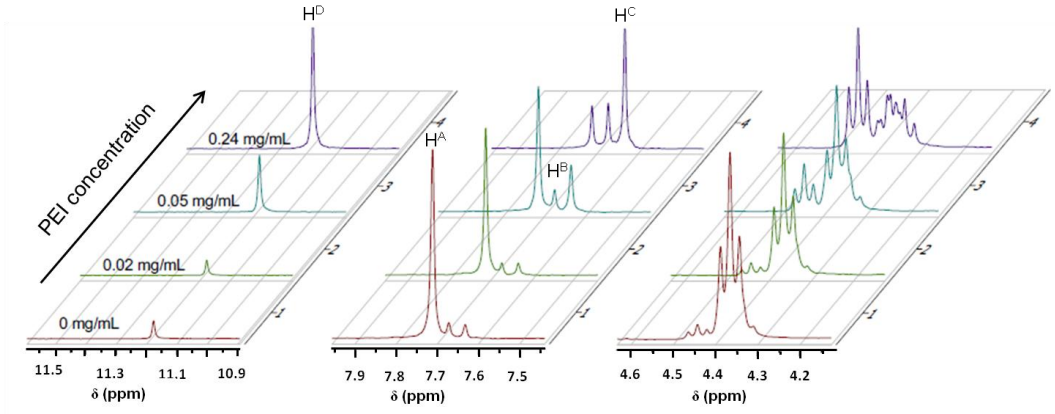

Figure 5.7. ^{1}H-NMR showing the effect of increasing the concentration of PEI on CPPO.

Table 5.4. Effect of PEI concentration on the molar ratios of oxalate diester molecules.

Concentration of PEI	Molar ratio of compound I : II : III
0 mg/mL	0.88 : 0.12 : 0.00
0.02 mg/mL	0.86 : 0.14 : 0.00
0.05 mg/mL	0.65 : 0.21 : 0.14
0.24 mg/mL	0.20 : 0.42 : 0.38

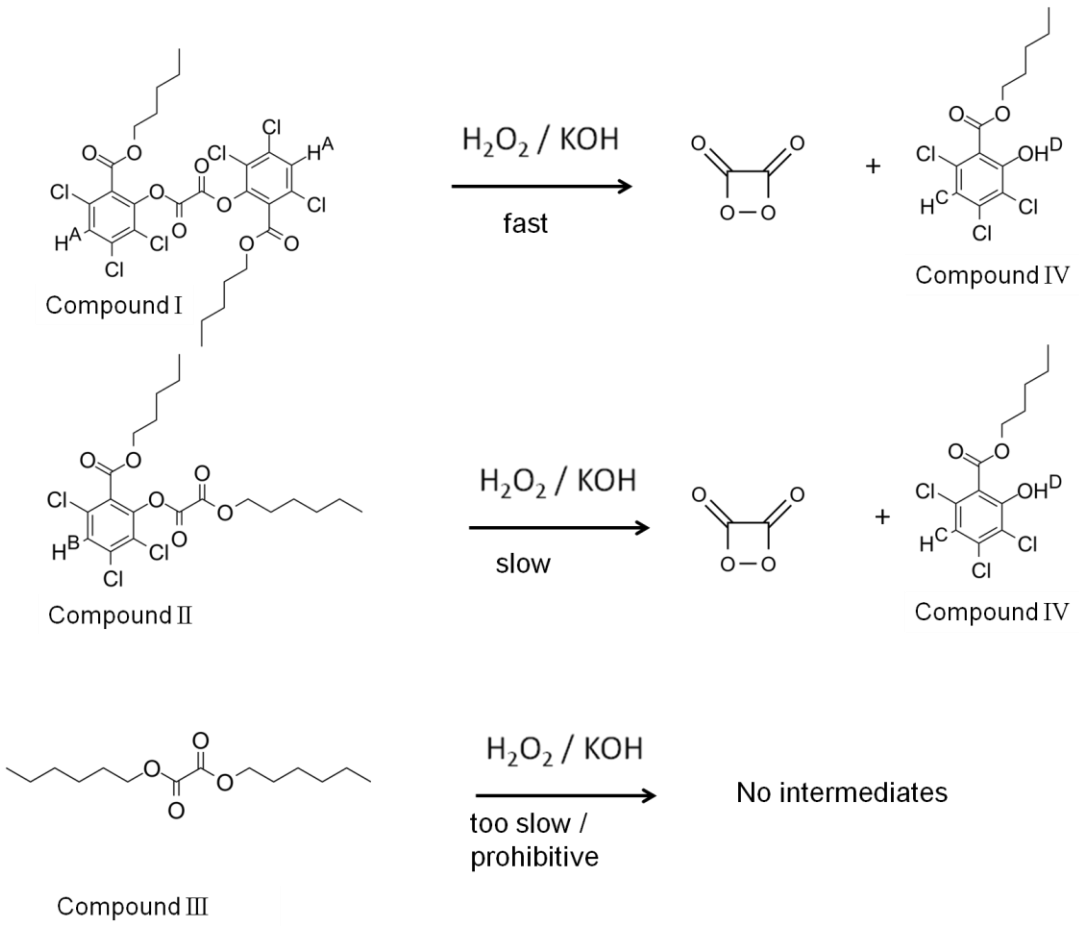

Figure 5.8. Schematic summary of the different reaction rates of the diesters I, II, and III to form 1,2-dioxetanedione upon addition of H_2O_2/KOH.

REFERENCES

(1) Tsunoda, M.; Imai, K. Analytical applications of peroxyoxalate chemiluminescence. *Analytica Chimica Acta* **2005**, *541*, 13–23.

(2) Lee, D.; Khaja, S.; Velasquez-Castano, J. C.; Dasari, M.; Sun, C.; Petros, J.; Taylor, W. R.; Murthy, N. In vivo imaging of hydrogen peroxide with chemiluminescent nanoparticles. *Nature materials* **2007**, *6*, 765–9.

(3) Casanova, D.; Bouzigues, C.; Nguyên, T.-L.; Ramodiharilafy, R. O.; Bouzhir-Sima, L.; Gacoin, T.; Boilot, J.-P.; Tharaux, P.-L.; Alexandrou, A. Single europium-doped nanoparticles measure temporal pattern of reactive oxygen species production inside cells. *Nature nanotechnology* **2009**, *4*, 581–5.

(4) Lim, C.-K.; Lee, Y.-D.; Na, J.; Oh, J. M.; Her, S.; Kim, K.; Choi, K.; Kim, S.; Kwon, I. C. Chemiluminescence-Generating Nanoreactor Formulation for Near-Infrared Imaging of Hydrogen Peroxide and Glucose Level in vivo. *Advanced Functional Materials* **2010**, *20*, 2644–2648.

(5) Chandross, E. A new chemiluminescent system. *Tetrahedron Letters* **1963**, 761–765.

(6) Rauhut, M. Chemiluminescence from concerted peroxide decomposition reactions. *Accounts of Chemical Research* **1969**, *2*, 80–87.

(7) Sigvardson, K.; Kennish, J.; Birks, J. Peroxyoxalate chemiluminescence detection of polycyclic aromatic amines in liquid chromatography. *Analytical Chemistry* **1984**, *1102,* 1096–1102.

(8) Chen, R.; Zhang, L.; Gao, J.; Wu, W.; Hu, Y.; Jiang, X. Chemiluminescent nanomicelles for imaging hydrogen peroxide and self-therapy in photodynamic therapy. *Journal of biomedicine & biotechnology* **2011**, *2011*, 679492.

(9) Dasari, M.; Lee, D.; Erigala, V. R.; Murthy, N. Chemiluminescent PEG-PCL micelles for imaging hydrogen peroxide. *Journal of Biomedical Materials Research Part A* **2009**, *89A*, 561–566.

(10) Emteborg (b. Stigbrand), M.; Irgum, K.; Gooijer, C.; Brinkman, U. A. T. Peroxyoxalate chemiluminescence in aqueous solutions: Coupling of immobilized enzyme reactors and 1,1′-oxalyldiimidazole chemiluminescence reaction to flow-injection analysis and liquid chromatographic systems. *Analytica Chimica Acta* **1997**, *357*, 111–118.

(11) Appelblad, P.; Jonsson, T.; Bäckström, T.; Irgum, K. Determination of C-21 Ketosteroids in Serum Using Trifluoromethanesulfonic Acid Catalyzed Precolumn Dansylation and 1,1‘-Oxalyldiimidazole Postcolumn Peroxyoxalate Chemiluminescence Detection. *Analytical Chemistry* **1998**, *70*, 5002–5009.

(12) Koo, J.-Y.; Schuster, G. B. Chemiluminescence of diphenoyl peroxide. Chemically initiated electron exchange luminescence. A new general mechanism for chemical production of electronically excited states. *Journal of the American Chemical Society* **1978**, *100*, 4496–4503.

(13) Stevani, C. V.; Silva, S. M.; Baader, W. J. Studies on the Mechanism of the Excitation Step in Peroxyoxalate Chemiluminescence. *European Journal of Organic Chemistry* **2000**, *2000*, 4037–4046.

(14) Catherall, C. L. R.; Palmer, T. F.; Cundall, R. B. Chemiluminescence from reactions of bis(pentachlorophenyl)oxalate, hydrogen peroxide and fluorescent compounds. Kinetics and mechanism. *Journal of the Chemical Society, Faraday Transactions 2* **1984**, *80*, 823.

(15) Scott, G.; Seitz, W. R.; Ambrose, J. Improved determination of hydrogen peroxide by measurement of peroxyoxalate chemiluminescence. *Analytica Chimica Acta* **1980**, *115*, 221–228.

(16) Kobayashi, S.-I.; Sekino, J.; Honda, K.; Imai, K. Application of high-performance liquid chromatography with a chemiluminescence detection system to determine catecholamines in urine. *Analytical biochemistry* **1981**, *112*, 99–104.

(17) Hayakawa, K.; Hasegawa, K.; Imaizumi, N.; S. Wong, O.; Miyazaki, M. Determination of amphetamine-related compounds by high-performance liquid chromatography with chemiluminescence and fluorescence detections. *Journal of Chromatography A* **1991**, *464*, 343–352.

(18) Hadd, A. G.; Lehmpuhl, D. W.; Kuck, L. R.; Birks, J. W. Chemiluminescence Demonstration Illustrating Principles of Ester Hydrolysis Reactions. *Journal of Chemical Education* **1999**, *76*, 1237.

(19) Garcia-Campana, A. *Chemiluminescence in analytical chemistry*; Garcia-Campana, A. M., Ed.; CRC Press, 2001, 2001.

(20) Hanaoka, N.; Givens, R. S.; Schowen, R. L.; Kuwana, T. Stopped-flow determination of the parameters affecting the application of peroxyoxalate chemiluminescence to high-performance liquid chromatographic detection. *Analytical Chemistry* **1988**, *60*, 2193–2197.

(21) Ow, H.; Larson, D. R.; Srivastava, M.; Baird, B. a; Webb, W. W.; Wiesner, U. Bright and stable core-shell fluorescent silica nanoparticles. *Nano letters* **2005**, *5*, 113–7.

(22) Herz, E.; Burns, A.; Bonner, D.; Wiesner, U. Large stokes-shift fluorescent silica nanoparticles with enhanced emission over free dye for single excitation multiplexing. *Macromolecular rapid communications* **2009**, *30*, 1907–10.

(23) Iyer, S. K.; Sarakune, K.; Johnson, K.; Huettner, S.; Wiesner, U. B. Synthesis of Bright Dye Incorporated Silica Nanoparticles as Chemicluminescent Probes for Hydrogen Peroxide Sensing. *in preparation*.

(24) Suteewong, T.; Sai, H.; Lee, J.; Bradbury, M.; Hyeon, T.; Gruner, S. M.; Wiesner, U. Ordered mesoporous silica nanoparticles with and without embedded iron oxide nanoparticles: structure evolution during synthesis. *Journal of Materials Chemistry* **2010**, *20*, 7807.

(25) Suteewong, T.; Sai, H.; Cohen, R.; Wang, S.; Bradbury, M.; Baird, B.; Gruner, S. M.; Wiesner, U. Highly aminated mesoporous silica nanoparticles with cubic pore structure. *Journal of the American Chemical Society* **2011**, *133*, 172–5.

(26) Creutz, S.; Teyssié, P.; Jérôme, R. Living Anionic Homopolymerization and Block Copolymerization of (Dimethylamino)ethyl Methacrylate. *Macromolecules* **1997**, *30*, 6–9.

(27) Kamperman, M.; Garcia, C. B. W.; Du, P.; Ow, H.; Wiesner, U. Ordered mesoporous ceramics stable up to 1500 degrees C from diblock copolymer mesophases. *Journal of the American Chemical Society* **2004**, *126*, 14708–9.

(28) Li, Z.; Sai, H.; Warren, S. C.; Kamperman, M.; Arora, H.; Gruner, S. M.; Wiesner, U. Metal Nanoparticle/Block Copolymer Composite Assembly and Disassembly. *Chemistry of materials : a publication of the American Chemical Society* **2009**, *21*, 5578–5584.

(29) Schädler, V.; Nardin, C.; Wiesner, U.; Mendes, E. Micellization of Model Macromolecular Surfactants as Studied by Static Light Scattering. *The Journal of Physical Chemistry B* **2000**, *104*, 5049–5052.

(30) Jonsson, T.; Irgum, K. New nucleophilic catalysts for bright and fast peroxyoxalate chemiluminescence. *Analytical chemistry* **2000**, *72*, 1373–80.

CHAPTER 6

Outlook

Early detection of diseases depends on performing assays on large number of biomarkers. Identifying diseases and biomarkers, for screening and developing drugs are broadly classified into three categories – prognostic, predictive and pharmacodynamics.[1] The prognostic biomarkers provide insights into differentiating highly invasive and less fatal systems as in the case of tumor cells, followed by predictive biomarkers that provide information about the response of the patient to a particular treatment and finally pharmacodynamic biomarker studies direct the dose selection of drugs on e.g. the tumor and the neighboring cells. High-throughput based biomarker and data analysis have greatly influenced clinical and genetic evaluations and helped develop appropriate medical diagnostics for early disease identification. In the case of cancer diagnosis, classifying the subtypes of cancer is based on concentrations of specific proteins or biomarkers on the cell surface to differentiate between the highly invasive subtypes and less fatal subtypes.[2–5] Extensive research has been carried out towards the development of multiplexed *in vitro* diagnostic assays to simultaneously detect and quantify biomarkers.[6] However in order to make accurate predictions to classify cancer subtypes, identification of cancer by its molecular expression profiles is required to complement the specific protein marker.[1,2,7] Thus, probes with specific tags need to be developed to carry out intracellular targeting in order to make more reliable predictions for early disease diagnosis.

6.1 Optically encoded multicolor nanoparticles

Fluorescence is the most sensitive and minimally invasive technique for optical detection of biological systems.[8] Several fluorescent probes are used as reporter molecules to detect biomarkers of interest and have been used in planar microarrays and bead based multiplexing for high throughput screening of proteins, antibodies, nucleotides or peptides.[5,9–14] Over the past two decades optically encoded microparticles and nanoparticles have been investigated and optimized for biological applications. Several surface modification methodologies have been developed for inorganic materials and adapted for biocompatible silica based materials to produce bioconjugated nanoparticle probes for various fluorescence based biological assays and applications.[15–18]

As demonstrated in this thesis, bright luminescent silica nanoparticles provide remarkable improvement in applications towards biological systems compared to other commonly used fluorescent probes especially for intracellular imaging. The sub-100 nm *multicolor* C dots (*mc*C dots) show tremendous improvement over other conventional optically encoded micron sized multicolor probes in terms of brightness per particle for each dye color and size. Twenty-six distinguishable encoded nanoparticles were generated as a result of three intensity or number-of-dyes-per-particle levels (0, 5, 20), and three dyes (RGB code, tetramethylrhodamine-5-maleimide (TMRm), Cy5-maleimide (Cy5m) and *N-(7-dimethylamino-4-methylcoumarin-3-yl)-maleimide* (DACm)). Furthermore, the thick blank silica shells spatially separated the dye layers resulting in no significant energy transfer in the onion-like particle structure. Thus *mc*C dots are a tremendous improvement over

Forster resonance energy transfer (FRET) based multicolor colloidal particles since maximum brightness is obtained for each dye in the particles. UV-visible spectroscopy and fluorometry were used to characterize the quantum enhancement, whereas fluorescence correlation spectroscopy provided quantitative information of the average dyes per particle as well the brightness per particle for each dye color. The dye colors used for the particle syntheses were chosen based on commonly available laser lines e.g. used for flow cytometry and confocal imaging. Due to their small size (sub-100 nm), the *mc*C dots provide a platform to extend applications from assay development to targeted intracellular live cell imaging.

As mentioned earlier the silica surface provides a suitable platform to carry out chemical modifications depending on the biological application of interest. To advance the technological platform of *mc*C dots towards intracellular applications, it would be important to have an additional fluorescent reporter molecule bound to the *mc*C dots. With this technology, specific binding events can be traced by correlating the unique barcode of the nanoparticles with the fluorescent signal resulting from the fluorescent reporter binding to the target. To this end, molecular beacons show tremendous potential as fluorescent reporters.[19] Traditionally for diagnostic applications, antibodies have been used extensively in assays due to their specificity for target molecules, however, in the past decade aptamers have emerged as a substitute for antibodies in diagnostic applications.[20] Several groups have expanded the applications of aptamers as fluorescent biosensor by binding fluorophores to specific sites on these oligonucleotides.[19,21] The activatable oligonucleotide is 15-25 nucleotide long hairpin loop structure with a fluorophore and quencher on opposite

terminus of the loop. In the hairpin loop conformation, the aptamer is in the 'off-state', upon binding to target molecule the hairpin loop undergoes conformational change and unfolds, releasing the fluorophore from the quencher and hence being in the "on-state'.[22] Researchers have applied such systems towards intracellular imaging.[23,24] The molecular beacon system along with the *mc*C dots system provides a tremendous platform to help in furthering the efforts towards intracellular fluorescence multiplexing.

6.2 Chemiluminescent probes

Hydrogen peroxide is a source of oxidative stress and the resulting oxidative damage of cells is connected to aging[25], and severe diseases such as cancer[26], cardiovascular disorders[27] and neurodegenerative diseases[28]. There is a great interest in developing contrast agents and imaging technologies for intracellular and *in vivo* imaging of hydrogen peroxide.[29–32] Peroxyoxalate chemiluminescence (POCL) is typically used for hydrogen peroxide detection and based on this several peroyoxalate based nanoparticles have been fabricated by physically incorporating fluorophores.[30,33–36] Developing bright chemiluminescence probes for biological applications is essential and this is demonstrated in this thesis (chapter 4), by covalently incorporating near-infrared dye into silica nanoparticles. For developing POCL based contrast agents it is necessary to have the oxalate molecule in close proximity to the fluorophore for intracellular and *in vivo* applications. However, for the success of such probes it is important to overcome the poor stability of the oxalate molecules in aqueous and polar solvents.[37] Aryl oxalates in the presence of polybases and mildly polar solvents undergo chemical modifications (chapter 5) making it

undesirable as oxalate molecules for developing POCL based contrast agents using aqueous silica nanoparticle synthesis and for physiological applications. However, this study does indicate that formation of an aliphatic-aryl mixed oxalate might be a suitable molecule since it delays chemiluminescence. Specific design criteria needs to be considered to either protect the aryl oxalate molecule from the solvent medium or synthesize new oxalate molecules that are more reactive in the presence of hydrogen peroxide.[37] Besides designing oxalate molecules, it is important from an *in vivo* stand point to make sub-10 nm biocompatible particles for efficient renal clearance.[38]

Bright fluorescent silica nanoparticles show tremendous potential towards biological applications based on size and pore tunability, versatility towards surface chemical modification and biocompatibility. In order to achieve the appropriate surface modification, two design criteria need to be considered: active targeting and stealth.[39] Active targeting requires choosing the appropriate ligands that recognize the target molecule. Following the optimization of the number of ligands per particle for a given size, the viability of active targeting nanoparticles as target molecule recognition in *in vitro* and in cellular and physiological conditions needs to be verified. Prior to intracellular applications, it is critical for the ligands on the particle to retain their conformation in order to recognize the molecule or protein of interest and not undergo conformational change in the presence of serum proteins as reported previously.[40] The stealth layer on the nanoparticle determines the half life of the nanoparticles in the blood circulation system and hence the delivery of the targeting ligand to the tumor. For *in vivo* studies polyethylene glycol chains have been used as a stealth layer to

increase the stability of nanoparticles in physiological buffer conditions and facilitate clearance via the renal system of animal model systems.[38]

Fabrication of these bright luminescent probes along with the remarkable breakthrough in the field of super-resolution microscopy will provide more insights into mechanistic understanding of biological events at the molecular and cellular levels. In order to push the boundaries of intracellular multicolor imaging and *in vivo* imaging, collaborative efforts are needed across the fields of chemistry and optics in order to shed more 'light' into biologically relevant problems.

REFERENCES

(1) Sawyers, C. L. The cancer biomarker problem. *Nature* **2008**, *452*, 548–52.

(2) Smith, A. M.; Dave, S.; Nie, S.; True, L.; Gao, X. Multicolor quantum dots for molecular diagnostics of cancer. *Expert review of molecular diagnostics* **2006**, *6*, 231–44.

(3) Ilyin, S. E.; Belkowski, S. M.; Plata-Salamán, C. R. Biomarker discovery and validation: technologies and integrative approaches. *Trends in biotechnology* **2004**, *22*, 411–6.

(4) Kingsmore, S. F. Multiplexed protein measurement: technologies and applications of protein and antibody arrays. *Nature reviews. Drug discovery* **2006**, *5*, 310–20.

(5) Inglese, J.; Johnson, R. L.; Simeonov, A.; Xia, M.; Zheng, W.; Austin, C. P.; Auld, D. S. High-throughput screening assays for the identification of chemical probes. *Nature chemical biology* **2007**, *3*, 466–79.

(6) Bake, K. D.; Walt, D. R. Multiplexed spectroscopic detections. *Annual review of analytical chemistry (Palo Alto, Calif.)* **2008**, *1*, 515–47.

(7) Hanash, S. M.; Pitteri, S. J.; Faca, V. M. Mining the plasma proteome for cancer biomarkers. *Nature* **2008**, *452*, 571–9.

(8) Weiss, S. Fluorescence Spectroscopy of Single Biomolecules. *Science* **1999**, *283*, 1676–1683.

(9) Ferguson, J. A.; Boles, T. C.; Adams, C. P.; Walt, D. R. A fiber-optic DNA biosensor microarray for the analysis of gene expression. *Nature biotechnology* **1996**, *14*, 1681–4.

(10) Lockhart, D. J.; Winzeler, E. a Genomics, gene expression and DNA arrays. *Nature* **2000**, *405*, 827–36.

(11) Fodor, S.; Read, J.; Pirrung, M.; Stryer, L.; Lu, A.; Solas, D. Light-directed, spatially addressable parallel chemical synthesis. *Science* **1991**, *251*, 767–773.

(12) Braeckmans, K.; De Smedt, S. C.; Leblans, M.; Pauwels, R.; Demeester, J. Encoding microcarriers: present and future technologies. *Nature reviews. Drug discovery* **2002**, *1*, 447–56.

(13) Simeonov, A.; Jadhav, A.; Thomas, C. J.; Wang, Y.; Huang, R.; Southall, N. T.; Shinn, P.; Smith, J.; Austin, C. P.; Auld, D. S.; Inglese, J. Fluorescence spectroscopic profiling of compound libraries. *Journal of medicinal chemistry* **2008**, *51*, 2363–71.

(14) Jun, B.-H.; Kang, H.; Lee, Y.-S.; Jeong, D. H. Fluorescence-based multiplex protein detection using optically encoded microbeads. *Molecules (Basel, Switzerland)* **2012**, *17*, 2474–90.

(15) Wang, L.; Zhao, W.; Tan, W. Bioconjugated silica nanoparticles: Development and applications. *Nano Research* **2008**, *1*, 99–115.

(16) Sperling, R. a; Parak, W. J. Surface modification, functionalization and bioconjugation of colloidal inorganic nanoparticles. *Philosophical transactions. Series A, Mathematical, physical, and engineering sciences* **2010**, *368*, 1333–83.

(17) Vivero-Escoto, J. L.; Huxford-Phillips, R. C.; Lin, W. Silica-based nanoprobes for biomedical imaging and theranostic applications. *Chemical Society reviews* **2012**, *41*, 2673–85.

(18) Wang, K.; He, X.; Yang, X.; Shi, H. Functionalized Silica Nanoparticles: A Platform for Fluorescence Imaging at the Cell and Small Animal Levels. *Accounts of chemical research* **2013**, *XXX*.

(19) Nutiu, R.; Li, Y. Aptamers with fluorescence-signaling properties. *Methods (San Diego, Calif.)* **2005**, *37*, 16–25.

(20) Jayasena, S. D. Aptamers: an emerging class of molecules that rival antibodies in diagnostics. *Clinical chemistry* **1999**, *45*, 1628–50.

(21) Song, S.; Wang, L.; Li, J.; Fan, C.; Zhao, J. Aptamer-based biosensors. *TrAC Trends in Analytical Chemistry* **2008**, *27*, 108–117.

(22) Tyagi, S.; Kramer, F. Molecular beacons: probes that fluoresce upon hybridization. *Nature biotechnology* **1996**, *14*, 303–8.

(23) Shi, H.; He, X.; Wang, K.; Wu, X.; Ye, X.; Guo, Q.; Tan, W.; Qing, Z.; Yang, X.; Zhou, B. Activatable aptamer probe for contrast-enhanced in vivo cancer imaging based on cell membrane protein-triggered conformation alteration. *Proceedings of the National Academy of Sciences of the United States of America* **2011**, *108*, 3900–5.

(24) Paige, J. S.; Nguyen-Duc, T.; Song, W.; Jaffrey, S. R. Fluorescence imaging of cellular metabolites with RNA. *Science (New York, N.Y.)* **2012**, *335*, 1194.

(25) Finkel, T. Oxidant signals and oxidative stress. *Current Opinion in Cell Biology* **2003**, *15*, 247–254.

(26) Ohshima, H.; Tatemichi, M.; Sawa, T. Chemical basis of inflammation-induced carcinogenesis. *Archives of Biochemistry and Biophysics* **2003**, *417*, 3–11.

(27) Shah, a M. Free radicals and redox signalling in cardiovascular disease. *Heart* **2004**, *90*, 486–487.

(28) Barnham, K. J.; Masters, C. L.; Bush, A. I. Neurodegenerative diseases and oxidative stress. *Nature reviews. Drug discovery* **2004**, *3*, 205–14.

(29) Miller, E. W.; Albers, A. E.; Pralle, A.; Isacoff, E. Y.; Chang, C. J. Boronate-based fluorescent probes for imaging cellular hydrogen peroxide. *Journal of the American Chemical Society* **2005**, *127*, 16652–9.

(30) Lee, D.; Khaja, S.; Velasquez-Castano, J. C.; Dasari, M.; Sun, C.; Petros, J.; Taylor, W. R.; Murthy, N. In vivo imaging of hydrogen peroxide with chemiluminescent nanoparticles. *Nature materials* **2007**, *6*, 765–9.

(31) Albers, A. E.; Okreglak, V. S.; Chang, C. J. A FRET-based approach to ratiometric fluorescence detection of hydrogen peroxide. *Journal of the American Chemical Society* **2006**, *128*, 9640–1.

(32) Chang, M. C. Y.; Pralle, A.; Isacoff, E. Y.; Chang, C. J. A selective, cell-permeable optical probe for hydrogen peroxide in living cells. *Journal of the American Chemical Society* **2004**, *126*, 15392–3.

(33) Lim, C.-K.; Lee, Y.-D.; Na, J.; Oh, J. M.; Her, S.; Kim, K.; Choi, K.; Kim, S.; Kwon, I. C. Chemiluminescence-Generating Nanoreactor Formulation for Near-Infrared Imaging of Hydrogen Peroxide and Glucose Level in vivo. *Advanced Functional Materials* **2010**, *20*, 2644–2648.

(34) Chen, R.; Zhang, L.; Gao, J.; Wu, W.; Hu, Y.; Jiang, X. Chemiluminescent nanomicelles for imaging hydrogen peroxide and self-therapy in photodynamic therapy. *Journal of biomedicine & biotechnology* **2011**, *2011*, 679492.

(35) Lee, Y.-D.; Lim, C.-K.; Singh, A.; Koh, J.; Kim, J.; Kwon, I. C.; Kim, S. Dye/peroxalate aggregated nanoparticles with enhanced and tunable chemiluminescence for biomedical imaging of hydrogen peroxide. *ACS nano* **2012**, *6*, 6759–66.

(36) Lee, D.; Erigala, V. R.; Dasari, M.; Yu, J.; Dickson, R. M.; Murthy, N. Detection of hydrogen peroxide with chemiluminescent micelles. *International journal of nanomedicine* **2008**, *3*, 471–6.

(37) Kim, S.; Seong, K.; Kim, O.; Kim, S.; Seo, H.; Lee, M.; Khang, G.; Lee, D. Polyoxalate nanoparticles as a biodegradable and biocompatible drug delivery vehicle. *Biomacromolecules* **2010**, *11*, 555–60.

(38) Burns, A. A.; Vider, J.; Ow, H.; Herz, E.; Penate-Medina, O.; Baumgart, M.; Larson, S. M.; Wiesner, U.; Bradbury, M. Fluorescent silica nanoparticles with efficient urinary excretion for nanomedicine. *Nano letters* **2009**, *9*, 442–8.

(39) Albanese, A.; Tang, P. S.; Chan, W. C. W. The effect of nanoparticle size, shape, and surface chemistry on biological systems. *Annual review of biomedical engineering* **2012**, *14*, 1–16.

(40) Salvati, A.; Pitek, A. S.; Monopoli, M. P.; Prapainop, K.; Bombelli, F. B.; Hristov, D. R.; Kelly, P. M.; Aberg, C.; Mahon, E.; Dawson, K. a Transferrin-functionalized nanoparticles lose their targeting capabilities when a biomolecule corona adsorbs on the surface. *Nature nanotechnology* **2013**, *8*, 137–43.

APPENDIX A

Supplementary information for Chapter 2

Experimental Section

Chemicals and materials

To carry out particle synthesis all chemicals were used as received. Tetraethoxysilane (TEOS, ≥ 99%, GC) and ammonia in ethanol (2.0 M) were purchased from Sigma Aldrich. (3-mercaptopropyl)-trimethoxysilane (MPTMS, >96% purity, Gelest Inc.) was used as a conjugation linker for dye incorporation in silica nanoparticles. The dyes used for the nanoparticle syntheses were Cy5-maleimide (Cy5m, GE Healthcare Life Sciences), tetramethylrhodamine-5-maleimide (TMRm, Life Technologies) and N-(7-dimethylamino-4-methylcoumarin-3-yl)maleimide (DACm, Anaspec, Inc.). The dyes were dissolved in dimethyl sulfoxide (DMSO, anhydrous ≥ 99.9%, Sigma Aldrich). Ethoxy-silane terminated poly-(ethylene glycol) (mPEG-Silane, molar mass ~5000 g/mol) was purchased from Layson Bio. The reactions were carried out in ethanol (200 proof, Pharmaco-Aaper) and deionized water (DI water, 18.2 $M\Omega.cm^{-1}$, purity, Millipore Milli-Q system). The particles were dialyzed using 10,000 molecular weight cut off (MWCO) Snakeskin dialysis membrane tube (Pierce) and were filtered with 0.2 μm PTFE syringe filters (Fisher Scientific). The particles were transferred into Dulbecco's Phosphate-Buffered Saline 1X buffer (DPBS without calcium and magnesium, Life Sciences) to carry out cell measurements using Macrosep® Advance Centrifugal Device, with a MWCO 30,000 (Pall Corporation). Sodium azide (BioUltra, ≥ 99.5%, Sigma Aldrich) was added to the particles in buffer solution to act as biocide.

For cellular imaging, the nanoparticles were electroporated using Gene Pulser X (Bio-Rad). The surface of the cells was labeled with Alexa Fluor 488 cholera toxin subunit B (Invitrogen).

Nanoparticle Syntheses

A.1.1. Dye conjugation:

The maleimide derivative of the dyes TMRm (2.6 mM in DMSO), Cy5m (1.26 mM in DMSO) and DACm (3.4 mM in DMSO) were dissolved in DMSO in nitrogen atmosphere glove box for 15 hours. For nanoparticle syntheses the dyes were conjugated with MPTMS in 1:25 dye to silane molar ratio in the glove box for 10-12 hours. Concentrations of 10×10^{-5} M/4.0×10^{-5} M/45×10^{-5} M were used for TMRm/Cy5m/DACm dye conjugates, respectively.

A.1.2. Syntheses of single color C dots with medium and high dye loadings:

A.1.2.a. Medium and high TMRm loaded nanoparticle syntheses

To 10 ml ethanol solution containing 0.88 M DI water and 0.2 M ammonia in ethanol, 1.3×10^{-5} M TMRm dye conjugate was added and left to stir for 15 minutes. To this solution 0.055 M TEOS was added and the reaction was left to stir for 12 hours. To this solution 0.105 M neat TEOS was added drop wise at a rate of 1 µl per ml of reaction volume every 30 minutes resulting in medium TMRm loaded particles (mG).

For high TMRm loaded particles (hG), 2×10^{-5} M TMRm dye conjugate was added to 5 ml of mG reaction solution and left to stir for 8 hours, followed by addition of 0.105 M neat TEOS at a rate of 1 µl per ml of reaction volume every 30 minutes. The solution was left to stir for 4 hours before further TMRm dye layer-TEOS silica shell addition. This sequence was repeated a total of four times to obtain hG particles.

A.1.2.b. Medium and high Cy5m nanoparticle syntheses

To 10 ml ethanol solution containing 1.2 M DI water and 0.2 M ammonia in ethanol, 1×10^{-5} M Cy5m dye conjugate was added and left to stir for 15 minutes. To this solution 0.055 M TEOS was added and the reaction was left to stir for 12 hours. To this solution 0.105 M neat TEOS was added drop wise at a rate of 1 µl per ml of reaction volume every 30 minutes resulting in medium Cy5m loaded particles (mR).

For high Cy5m loaded particles (hR), 1×10^{-5} M Cy5m dye conjugate was added to 5 ml of mR reaction solution and left to stir for 8 hours, followed by addition of 0.105 M neat TEOS at a rate of 1 µl per ml of reaction volume every 30 minutes. The solution was left to stir for 4 hours before further Cy5m dye layer-TEOS silica shell addition. This sequence was repeated a total of three times to obtain hR particles.

A.1.2.c. Medium and high DACm nanoparticle synthesis

To 10 ml ethanol solution containing 0.88 M DI water and 0.2 M ammonia in ethanol, 5×10^{-5} M DACm dye conjugate was added and left to stir for 15 minutes. To this solution 0.055 M neat TEOS was added and the reaction was left to stir for 12 hours. To this solution 0.15 M neat TEOS was added drop wise at a rate of 1 µl per ml of reaction volume every 30 minutes resulting in medium DACm loaded particles (mB).

To 5 ml of mB particle solutions, 5 ml of ethanol was added to synthesize high DACm loaded particles (hB). The concentrations of DI water and ammonia in ethanol were maintained at 0.88 M and 0.2 M, respectively. 9×10^{-5} M DACm dye conjugate was added to the 10 ml reaction solution and left to stir for 8 hours, followed by 0.15 M neat TEOS at a rate of 1 µl per ml of reaction volume every 30 minutes. The solution

was left to stir for 4 hours before further DACm dye layer-TEOS silica shell addition. This sequence was repeated a total of four times to obtain hB particle solutions.

*A.1.3. Syntheses of multicolor C dots (mc***C dots)*:**

A.1.3.a. Thick silica shell synthesis on medium and high TMRm loaded particles:

Medium TMRm loaded particles (mG) were synthesized by scaling the reaction solution up to 100 ml. 1.3×10^{-5} M TMRm dye conjugate was added to 100 ml of ethanol containing 0.88 M DI water and 0.2 M ammonia in ethanol and left to stir for 15 minutes, followed by 0.055 M neat TEOS and was left to stir for 12 hours. To this solution 0.105 M neat TEOS was added drop wise at a rate of 1 µl per ml of reaction volume every 30 minutes to form a silica shell. Following the mG particle synthesis the solution was separated into two round bottom flasks with 50 ml each. To one of the 50 ml mG particle solution, 2×10^{-5} M TMRm dye conjugate was added and left to stir for 8 hours, followed by addition of 0.105 M neat TEOS at a rate of 1 µl per ml of reaction volume every 30 minutes. The solution was left to stir for 4 hours before further TMRm dye layer-TEOS silica shell addition. This sequence was repeated a total of four times to obtain high TMRm particles (hG).

To each of the 50 ml mG and hG solutions, 2.6 M neat TEOS was added at a rate of 2 µl per ml of reaction volume every 30 minutes to get a 10-12 nm thick silica shell before carrying out dual color particle synthesis.

A.1.3.b. Thick silica shell synthesis on medium and high Cy5m loaded particles:

Medium Cy5m loaded particles (mR) were synthesized by scaling to 30 ml reaction system. 1×10^{-5} M Cy5m dye conjugate was added to 30 ml ethanol solution containing 1.2 M DI water and 0.2 M ammonia in ethanol and left to stir for 15 minutes followed

by 0.055 M neat TEOS and the reaction was left to stir for 12 hours. To this solution 0.105 M neat TEOS was added drop wise at a rate of 1 µl per ml of reaction volume every 30 minutes to form a silica shell. The mR particle solution was separated into two round bottom flasks with 15 ml each. To one of the 15 ml mR particle solution, 1×10^{-5} M Cy5m dye conjugate was added and left to stir for 8 hours, followed by addition of 0.105 M neat TEOS at a rate of 1 µl per ml of reaction volume every 30 minutes. The solution was left to stir for 4 hours before further Cy5m dye layer-TEOS silica shell addition. This sequence was repeated a total of three times to obtain high Cy5m loaded particles (hR).

To each of the 15 ml mR and hR solutions, 1.8 M neat TEOS was added at a rate of 2 µl per ml of reaction volume every 30 minutes to get a shell that was 6-8 nm thick.

Syntheses of dual color C dots:

A.1.3.c. Cy5m dye conjugate addition to medium and high TMRm particles:

To synthesize particles with Cy5m dye as the second layer, 30 ml of mG and hG particle solutions with 10-12 nm thick silica shell were taken in two separate round bottom flasks (from section 1.3.a).

For medium Cy5m loading, 1×10^{-5} M Cy5m dye conjugate was added to each of the reaction flasks containing 30 ml of mG and hG particle solutions and left to stir for 8 hours. To this reaction solution 0.105 M neat TEOS was added drop wise at the rate of 1 µl per ml of reaction volume every 30 minutes to form a thin silica shell. 15 ml was removed from each reaction solution and was set aside as mGmR and hGmR particle solutions.

For high Cy5m loading, 1×10^{-5} M Cy5m dye conjugate was added to each of 15 ml mGmR and hGmR reaction solutions and left to stir for 8 hours, followed by addition of 0.105 M neat TEOS at a rate of 1 µl per ml of reaction volume every 30 minutes. The solution was left to stir for 4 hours before further Cy5m dye layer-TEOS silica shell addition. This alternating Cy5m dye conjugate-TEOS shell addition sequence was carried out a total of two times in order to get particles with mGhR and hGhR particle solutions.

A.1.3.d. DACm dye conjugate addition to medium and high TMRm particles:

To synthesize particles with DACm as the second dye layer, 10 ml of the medium and high TMRm particle solutions with 10-12 nm thick silica shell were taken in two separate round bottom flasks (from section 1.3.a).

For medium DACm loading, 5×10^{-5} M DACm dye conjugate was added to each of the reaction flasks containing 10 ml of mG and hG particle solutions and the reaction solution was left to stir for 8 hours. A thin silica shell was added to the reaction by drop wise addition of 0.15 M neat TEOS at a rate of 1 µl per ml of reaction volume every 30 minutes to form silica shell. 5 ml of the reaction solutions were set aside as mGmB and hGmB particle solutions.

For high DACm loading, 5 ml of ethanol was added to 5 ml of dual color mGmB and hGmB particle solutions. The concentrations of DI water and ammonia in ethanol were maintained at 0.88 M and 0.2 M, respectively. 9×10^{-5} M DACm dye conjugate was added to the 10 ml reaction solution and left to stir for 8 hours, followed by 0.15 M neat TEOS at a rate of 1 µl per ml of reaction volume every 30 minutes. The solution was left to stir for 4 hours before further dye layer-TEOS silica shell addition.

This alternating DACm dye conjugate-TEOS shell addition sequence was carried out a total of three times to get high DACm loaded particles as mGhB and hGhB particle solutions.

A.1.3.e. DACm dye conjugate addition to medium and high Cy5m particles:

To synthesize particles with DACm as the second dye layer, 10 ml of the mR and hR particle solutions with 6-8 nm thick silica shell were taken in two separate round bottom flasks (from section A.1.3.b).

For medium DACm loading, 5×10^{-5} M DACm dye conjugate was added to each of the reaction flasks containing 10 ml of mR and hR particle solutions and the reaction solution was left to stir for 8 hours. A thin silica shell was added to the reaction by drop wise addition of 0.15 M neat TEOS at a rate of 1 µl per ml of reaction volume every 30 minutes to form silica shell. 5 ml of the reaction solutions were set aside as mRmB and hRmB particle solutions.

For high DACm loading, 5 ml of ethanol was added to 5 ml of dual color mRmB and hRmB particle solutions. The concentrations of DI water and ammonia in ethanol were maintained at 0.88 M and 0.2 M, respectively. 9×10^{-5} M DACm dye conjugate was added to the 10 ml reaction solution and left to stir for 8 hours, followed by 0.15 M neat TEOS at a rate of 1 µl per ml of reaction volume every 30 minutes. The solution was left to stir for 4 hours before further dye layer-TEOS silica shell addition. This alternating DACm dye conjugate-TEOS shell addition sequence was carried out a total three times to get high DACm loaded particles as mRhB and hRhB particle solutions.

Syntheses of triple color C dots:

A.1.3.f. Thick silica shell syntheses on dual color particles containing TMRm and Cy5m:

To 10 ml of mGmR, mGhR, hGmR and hGhR as mentioned in section 1.3.c., 1.8 M neat TEOS was added at a rate of 2 µl per milliliter of reaction volume every 30 minutes to get a shell that was 6-8 nm thick. 10 ml solution of each of dual color particles containing TMRm and Cy5m were taken in separate round bottom flasks. The concentrations of DI water and ammonia were maintained at 0.88 M and 0.2 M, respectively.

A.1.3.g. DACm dye conjugate addition to dual color particles loaded with TMRm and Cy5m:

For medium DACm loading, 5×10^{-5} M DACm dye conjugate was added to each of the reaction flasks containing 10 ml of mGmR, mGhR, hGmR and hGhR particle solutions and was left to stir for 8 hours. A thin silica shell was added to the reaction by drop wise addition of 0.15 M neat TEOS at a rate of 1 µl per milliliter of reaction volume every 30 minutes to form silica shell. 5 ml of the reaction solutions were set aside as mGmRmB, mGhRmB, hGmRmB and hGhRmB particles.

For high DACm loading, 5 ml of ethanol was added to 5 ml of triple color particle solutions containing medium DACm loaded particles. The concentrations of DI water and ammonia in ethanol were maintained at 0.88 M and 0.2 M, respectively. 9×10^{-5} M DACm dye conjugate was added to the 10 ml reaction solution and left to stir for 8 hours, followed by 0.15 M neat TEOS at a rate of 1 µl per milliliter of reaction volume every 30 minutes. The solution was left to stir for 4 hours before further DACm dye layer-TEOS silica shell addition. This alternating DACm dye conjugate-TEOS shell

addition sequence was carried out three times to get high DACm loaded particles: mGmRhB, mGhRhB, hGmRhB and hGhRhB particles.

A.1.3.h. Silica shell growth on nanoparticles prior to PEGylation:

A silica shell was grown on all particles by drop wise addition of TEOS to get the same size for all the nanoparticles. Please note for all solutions the concentrations of DI water and ammonia in ethanol were maintained at 0.88 M and 0.2 M, respectively.

To 10 ml solution containing medium (section 1.1.b)/high (section 1.1c) DACm particles, 4.8 M TEOS was added and to medium/high TMRm particles (section 1.3.a), 2.7 M TEOS was added at a rate of 2 µl per milliliter of reaction volume every 30 minutes. To 5 ml of medium and high Cy5m particle solutions (section 1.3.b), 3.6 M TEOS was added at a rate of 2 µl per milliliter of reaction volume every 30 minutes.

To 5 ml of the dual color particle solutions containing G-R (section 1.3.c)/ G-B (section 1.3.d)/R-B (section 1.3.e), 2.6 M TEOS/ 2.6 M TEOS/ 3.3 M TEOS were added, respectively, at a rate of 2 µl per milliliter of reaction volume every 30 minutes.

To 5 ml of the triple color particle solutions containing only medium DACm particles (section1.3.f), an additional 0.7 M TEOS was added at a rate of 2 µl per milliliter of reaction volume every 30 minutes. No additional TEOS was added to triple color particles containing high DACm.

A.1.4. PEGylation of mc*C dots *nanoparticles:

To 1.0 liter of DI water was adjusted to pH 5 by adding 2.0 M hydrochloric acid (aq.) using a pH meter (VWR International Symphony, SB70P). To carry out PEGylation, all the particles were grown to the same size as mentioned in the particle synthesis section. 0.08 M aqueous PEG-silane (mPEG-silane, M.W. 5k) solution was made by

dissolving the PEG-silane in DI water at pH 5. 1 ml of this solution was taken in a vial and 2 ml of ethanol was added and the solution was left to stir for about 10 minutes. 1.0 ml of the as-made particle solution was added drop wise to 3 ml of mPEG-silane dissolved in the ethanol-water mixture, and then the solution was left to stir in an oil bath maintained at 70°C for 24 hours.

After PEGylation the particles were dialyzed in DI water using 10,000 MWCO dialysis membrane tube and filtered with 0.2 µm PTFE syringe filters and stored in dark at room temperature for further characterization.

For cell imaging measurements the particles were transferred into a Dulbecco's Phosphate-Buffered Saline *(*DPBS*)* using Macrosep® Advance Centrifugal Device, with a MWCO of 30,000. Following dialysis, 5 ml of the PEGylated nanoparticle solution was added to 5 ml of buffer solution and centrifuged for 30 minutes at 3500 rpm. This process was repeated three times with buffer solution. As a final step the particles were heated to 75°C for 15 minutes to pasteurize the solution followed by the addition of 0.1 % (w/v) sodium azide aqueous solution.

Characterization of medium and high dye loaded nanoparticles

Photographs of the reflected light image of the 27 cuvettes were taken under ambient light. The photo image was arranged as particles with no TMRm dye (bottom row), particles with ~ 5 TMRm dyes (middle row) and particles with ~ 20 dyes in the core (top row). Each row was taken separately using the identical settings of ISO 100 and 1/20th of a second exposure at f/4.5 on a Canon EOS digital Rebel 400 D camera, fixed on a tripod and was then stacked in the arrangement as mentioned using Adobe Photoshop.

A.2.1. Spectrometry and Spectrofluorometry

The particles were absorbance matched to the respective free dye by diluting the particles or free dye with DI water in a quartz cuvette using a Varian Cary 5000 Spectrometer (Varian, Palo Alto, CA). The extinction coefficients of DACm (25,000 $M^{-1}cm^{-1}$), TMRm (98,000 $M^{-1}cm^{-1}$) and Cy5m (250,000 $M^{-1}cm^{-1}$) were used to quantify the concentration of dyes in the samples.

Fluorescence measurements of absorbance matched samples were performed on a Photon Technologies International Quantamaster Spectrofluorometer (PTI, Birmingham, NJ).

A.2.2. Fluorescence Correlation Spectroscopy (FCS)

To quantify the brightness per particle, hydrodynamic radius and concentration of particles; the absorbance matched samples were measured on a home-built multi-spectral Fluorescence Correlation Spectroscopy (FCS) set up using solid state 405 nm (for DACm particles), HeNe 535 nm (for TMRm particles) and HeNe 633 nm (for Cy5m particles) laser excitation sources. The excitation beam was reflected through a 60X Olympus UPlan SAPO, 1.2NA water immersion objective. A 200μL volume at nanomolar concentrations of the fluorescent sample was placed on a microwell dish with a No. 1.5 coverslip bottom (MatTek P35G-1.5-10-C). The emitted light from the sample was collected by the objective, passed through the excitation/emission dichroic and was reflected into a focusing lens by the emission mirror. The emission light was focused though a long pass filter (Chroma) to remove any excitation light and collect only the emission photons. A 50 micron pinhole was used to axially limit the effective volume from which fluorescence was collected. The light then passed through a

second lens into an avalanche photodiode (SPCM 14, Perkin Elmer). The resulting photocurrent was digitally autocorrelated with a correlator card (Correlator.com).

The data was fit using a triplet corrected autocorrelation function, as shown in the analytical form in equation 1.[1]

$$G(\tau) = 1 + \left(\frac{1}{N}\right) \times \left(1 - A + A \times \exp\left(\frac{t}{\tau_R}\right)\right) \times \left(\frac{1}{\left(1+\frac{t}{\tau_D}\right)}\right) \times \left(\frac{1}{\left(\sqrt{1+\frac{t}{\tau_D}s^2}\right)}\right) \qquad (1)$$

A is the amplitude of triplet correction, τ_R is the apparent diffusion time of a dye molecule/particle in the triplet state, τ_D is the diffusion time of the molecule/particle in the singlet state and *N* is the number of molecules in the focal volume. The structure factor parameter '*s'* describes the 3-D Gaussian focal volume in terms of the ratio of the axial to the radial axis and is calculated from measurements of the standard dye with known diffusion coefficient.[1,2] To obtain the structure factor '*s'* for the 405 nm, 535 nm and 633 nm laser lines the dyes used were N-(7-dimethylamino-4-methylcoumarin-3-yl)-maleimide, tetramethylrhodamine-5-maleimide and Alexa Fluor 647-maleimide, respectively.

Cellular imaging

A.3.1. Cell culture

RBL-2H3 cells were maintained in monolayer culture in MEM supplemented with 20% FBS (Atlanta Biologicals) and 10 μg/ml gentamicin sulfate as described previously.[3]

A.3.2. Nanoparticle delivery into cells via electroporation

Cells were harvested 3–5 days after passage and 0.5 x 10^6/ml RBL-2H3 cells were electroporated in 0.5 ml of cold electroporation buffer (137 mM NaCl, 2.7 mM KCl, 1 mM $MgCl_2$, 1 mg/ml glucose, 20 mM HEPES (pH 7.4) with 200µl of nanoparticles suspended at (5-10 µM). Square wave electroporation was used with settings of 280 V, 10.0 ms pulse length, 4 pulses, and pulse intervals of 0.1 ms using Gene Pulser X (Bio-Rad). Electroporated cells were allowed to recover for approximately an hour before being fixed with 4% paraformaldehyde and 0.1% glutaraldehyde. Fixed cells were then labeled with 0.5 µg/ml Alexa 488 cholera toxin subunit B (Invitrogen) for 15 min at room temperature to stain the cell membrane.

A.3.3. Confocal imaging

Cells containing nanoparticles were imaged on a Zeiss 510 LSM confocal microscope using a 40X water objective (N.A=1.2). Images were taken sequentially using the 405, 488, 561, 633 nm laser lines for excitation and the 420-480 (Band Pass, BP), 575 (Long Pass, LP), 505-550 (BP) and 650 (LP) filter sets for collecting the emitted light.

REFERENCES

(1) Larson, D. R.; Ow, H.; Vishwasrao, H. D.; Heikal, A. a.; Wiesner, U.; Webb, W. W. Silica Nanoparticle Architecture Determines Radiative Properties of Encapsulated Fluorophores. *Chemistry of Materials* **2008**, *20*, 2677–2684.

(2) Cohen, B.; Martin, C.; Iyer, S. K.; Wiesner, U.; Douhal, A. Single Dye Molecule Behavior in Fluorescent Core–Shell Silica Nanoparticles. *Chemistry of Materials* **2012**, *24*, 361–372.

(3) Gosse, J. A.; Wagenknecht-Wiesner, A.; Holowka, D.; Baird, B. Transmembrane sequences are determinants of immunoreceptor signaling. *Journal of immunology (Baltimore, Md. : 1950)* **2005**, *175*, 2123–31.

APPENDIX B

Supplementary information for Chapter 3

Experimental Section

Chemicals and materials

To carry out particle synthesis all chemicals were used as received. Tetraethoxysilane (TEOS, ≥ 99%, GC) and ammonia in ethanol 2.0 M) were purchased from Sigma Aldrich. (3-mercaptopropyl)-trimethoxysilane (> 96% purity, MPTMS, Gelest Inc.) was used as a conjugation linker for dye incorporation in silica nanoparticles. The dyes used for the nanoparticle syntheses were Cy5-maleimide (Cy5m, GE Healthcare Life Sciences), tetramethylrhodamine-5-maleimide (TMRm, Life Technologies) and N-(7-dimethylamino-4-methylcoumarin-3-yl)-maleimide (DACm, Anaspec, Inc.). The dyes were dissolved in dimethyl sulfoxide (DMSO, anhydrous ≥ 99.9%, Sigma Aldrich). Ethoxy-silane terminated poly-(ethylene glycol) (mPEG-Silane, molar mass ~5000 g/mol) was purchased from Layson Bio. The reactions were carried out in ethanol (200 proof, Pharmaco-Aaper) and deionized water (DI water, 18.2 MΩ.cm-1, purity, Millipore Milli-Q system). The particles were dialyzed using 10,000 molecular weight cut off (MWCO) Snakeskin dialysis membrane tube (Pierce) and were filtered with 0.2 μm PTFE syringe filters (Fisher Scientific). The particles were transferred into Dulbecco's Phosphate-Buffered Saline 1X buffer (DPBS without calcium and magnesium, Life Sciences) to carry out cell measurements using Macrosep® Advance Centrifugal Device, with a MWCO 30,000 (Pall Corporation). Sodium azide (BioUltra, ≥ 99.5%, Sigma Aldrich) was added to the particles in buffer solution to act as biocide.

Nanoparticle Syntheses

Dye conjugation:

The maleimide derivative of the dyes TMRm (2.6 mM in DMSO), Cy5m (1.26 mM in DMSO) and DACm (3.4 mM in DMSO) were dissolved in DMSO in nitrogen atmosphere glove box for 15 hours. For nanoparticle syntheses the dyes were conjugated with MPTMS in 1:25 dye to silane molar ratio in the glove box for 10-12 hours. Concentrations of 10×10^{-5} M/4.0×10^{-5} M/45×10^{-5} M were used for TMRm/Cy5m/DACm dye conjugates, respectively.

Medium TMRm dye loaded nanoparticle synthesis at varied shell thickness

To 35ml ethanol solution containing 0.88 M DI water and 0.2 M ammonia in ethanol, 1.3×10^{-5} M TMRm dye conjugate was added and left to stir for 15 minutes. To this solution 0.055 M TEOS was added and the reaction was left to stir for 12 hours.

To this solution varied TEOS concentrations were added to get different silica shell thickness. To obtain a shell thickness 6.5 nm, 1.5 M neat TEOS was added drop wise at a rate of 3 µl per milliliter of reaction volume every 30 minutes. Once the appropriate thickness was obtained, 5mL of the above solution was removed for dye conjugate addition.

To obtain a shell thickness of 9.0 nm, to the remaining 10mL solution, 2.0 M neat TEOS was added drop wise at a rate of 5 µl per milliliter of reaction volume every 30 minutes. From this reaction solution 5mL was further removed for dye conjugate addition once the appropriate shell thickness was obtained.

As a final step to obtain 12 nm thick shells, 2.6 M neat TEOS was added drop wise at a rate of 10 µl per milliliter of reaction volume every 30 minutes. Once the appropriate shell thickness was obtained this solution was set aside for dye conjugate addition.

DACm addition to TMRm nanoparticles:

Following the synthesis of the particle with varied shell thicknesses, three vials were set up containing 2.5 mL of TMRm solution with 0.88 M DI water and 0.2 M ammonia in ethanol. To each of these vials 9×10^{-5} M of DACm was added and the reaction was left to stir overnight for about 10-12 hours. Following the DACm dye conjugate addition, 0.15 M neat TEOS was added to each vial at a rate of 1µl per milliliter of reaction volume every 30 minutes.

Cy5m addition to TMRm nanoparticles:

Following the synthesis of the particle with varied shell thicknesses, three vials were set up containing 2.5 ml of TMRm solution with 0.88 M DI water and 0.2 M ammonia in ethanol. To each of these vials 1×10^{-5} M of Cy5m was added and the reaction was left to stir overnight for about 10-12 hours. Following the Cy5m dye conjugate addition, 0.105 M TEOS was added to each vial at a rate of 1µl per milliliter of reaction volume every 30 minutes.

Multicolor particle synthesis:

The synthesis has been explained in detail in previous work.[1]

Dynamic Light Scattering

The hydrodynamic diameter of the TMRm particles were measured using a Malvern Nano-SZ operated at 20 ^{o}C. Each size measurement was carried out three times and the diameter reported is the average diameter obtained from number percent statistics.

Spectrometry and Spectrofluorometry

The particles were absorbance matched to the respective free dye by diluting the particles or free dye with water in a quartz cuvette using a Varian Cary 5000 Spectrometer (Varian, Palo Alto, CA). The extinction coefficients of DACm (25,000 $M^{-1}cm^{-1}$), TMRm (98,000 $M^{-1}cm^{-1}$) and Cy5 (250,000 $M^{-1}cm^{-1}$) were used to quantify the concentration of dyes in the samples.

Fluorescence measurements of absorbance matched samples were performed on a Photon Technologies International Qantamaster spectrofluorometer (PTI, Birmingham, NJ) to quantify the quantum yield of the particles per dye.

Fluorescence Correlation Spectroscopy

To quantify the brightness per particle, hydrodynamic radius and concentration of particles; the absorbance matched samples were measured using a home-built multicolor Fluorescence Correlation Spectroscopy (FCS) using solid state 405 nm (for DACm particles), HeNe 535 nm (for TMRm particles) and HeNe 633 nm (for Cy5m particles) excitation source. The excitation beam was reflected through a 60X Olympus UPlan SAPO, 1.2NA water immersion objective. A 200μL volume at nanomolar concentrations of the fluorescent sample was placed on a microwell dish with a No. 1.5 coverslip bottom (MatTek P35G-1.5-10-C). The emitted light from the sample was collected by the objective, passed through the excitation/emission dichroic and was reflected into a focusing lens by the emission mirror. The emission light was focused though a long pass filter (Chroma) to remove any excitation light and collect only the emission photons. A 50 micron pinhole was used to axially limit the effective volume from which fluorescence was collected. The light then passed through a

second lens into an avalanche photodiode (SPCM 14, Perkin Elmer). The resulting photocurrent was digitally autocorrelated with a correlator card (Correlator.com).

The data was fit using a triplet corrected autocorrelation function, G (τ), as shown in the analytical form in equation 1.

$$G(\tau) = 1 + \left(\frac{1}{N}\right) \times \left(1 - A + A \times \exp\left(\frac{t}{\tau_R}\right)\right) \times \left(\frac{1}{\left(1+\frac{t}{\tau_D}\right)}\right) \times \left(\frac{1}{\left(\sqrt{1+\frac{t}{\tau_D}s^2}\right)}\right) \qquad (1)$$

A is the amplitude of triplet correction, τ_R is the apparent diffusion time of a dye molecule/particle in the triplet state, τ_D is the diffusion time of the molecule/particle in the singlet state and *N* is the number of molecules in the focal volume. The structure factor parameter *s* describes the 3-D Gaussian focal volume in terms of the ratio of the axial to the radial axis and is calculated from measurements of the standard dye with known diffusion coefficient.[2,3] To obtain the structure factor *s* for the 405 nm, 561 nm and 633 nm laser lines the dyes used were N-(7-dimethylamino-4-methylcoumarin-3-yl)maleimide, tetramethylrhodamine-5-maleimide and AF 647 maleimide, respectively. The number of dyes per particle was derived from the ratio of concentration of dyes from absorbance measurements and concentration of particles as measured by FCS.

REFERENCES

(1) Iyer, S.K.; Wilkes, M.; Cohen, R.; Wiesner, U.B.; Barbara, B. Multicolor Fluorescent Core-Shell Silica Nanoparticles for Multiplexed and Multicolor Intra-cellular Imaging. *in preparation* **2013**.

(2) Larson, D. R.; Ow, H.; Vishwasrao, H. D.; Heikal, A. a.; Wiesner, U.; Webb, W. W. Silica Nanoparticle Architecture Determines Radiative Properties of Encapsulated Fluorophores. *Chemistry of Materials* **2008**, *20*, 2677–2684.

(3) Cohen, B.; Martin, C.; Iyer, S. K.; Wiesner, U.; Douhal, A. Single Dye Molecule Behavior in Fluorescent Core–Shell Silica Nanoparticles. *Chemistry of Materials* **2012**, *24*, 361–372.

Appendix C

Supplementary Information for chapter 4

Figure C.1. Scanning electron microscopy (SEM) of blank silica nanoparticles used for synthesis of dSNP.

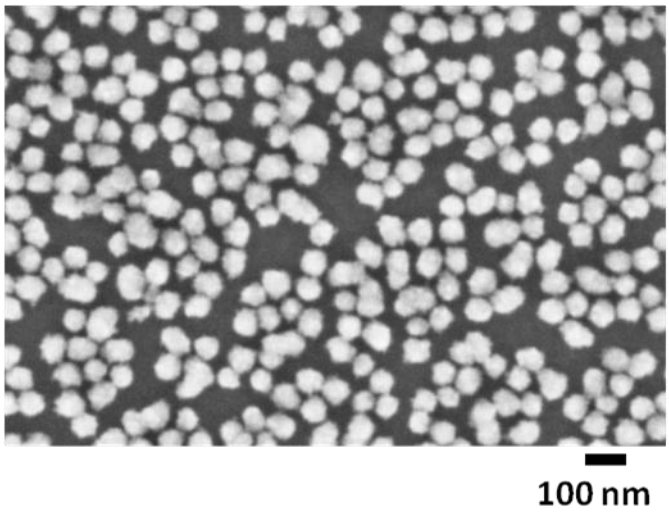

Figure C.2. Optical characterization of ADS832WS free dye showing chemiluminescence emission of free dye at different time points.

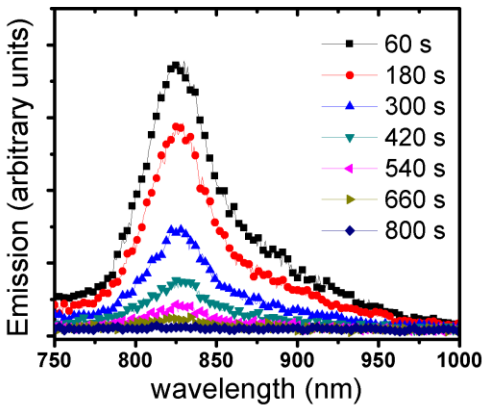

Figure C.3. Spectra comparing (a) chemiluminescence (CL) in ethylacetate/1-hexanol solvent mixture and (b) photoluminescence (PL) in methanol of free parent dye.

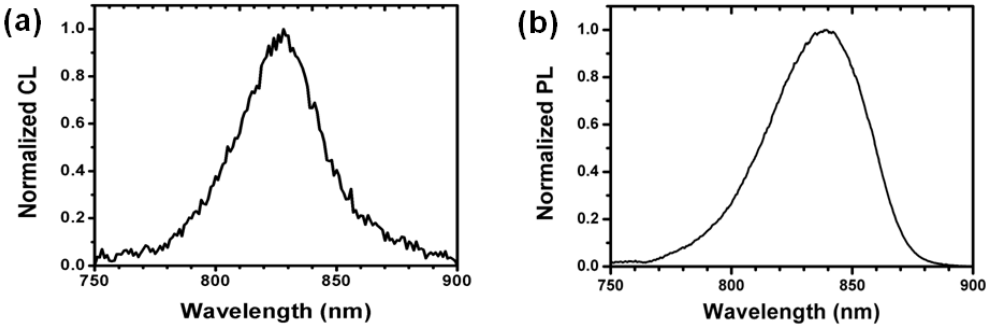

Figure C.4. Transient absorption kinetics of free dye and dye incorporated nanoparticles for PIA and GSB states

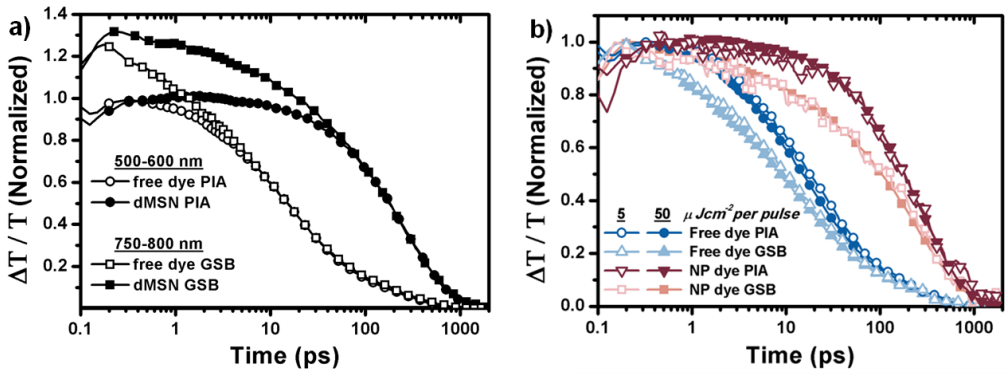

(a) Normalized transient absorption kinetics of the free dye and the dye incorporated in the nanoparticle for PIA and GSB states. The observed discrepancy between the kinetic traces of the GSB and the PIA is likely due to the GSB feature shifting to lower energy, i.e. out of the region probed in this experiment. This results in an apparent decay of the GSB signal by ~ 25% on a sub-4ps timescale for free dye and sub-50 ps timescale for dMSNs, after which the GSB and PIA kinetics are closely matched. The GSB kinetics are scaled to match the PIA kinetics at 10 and 100 ps for free dye and dMSN, respectively. (b) Normalized transient absorption kinetics of the free dye and the dye incorporated in the nanoparticle at fluences of 5 μJcm^{-2} per pulse (open symbols) and 50 μJcm^{-2} per pulse (closed symbols). The excitation wavelength was 650-725nm.

Figure C.5. Normalized transient absorption kinetics of the free dye in the PIA region (550-600nm) at concentrations of 3, 30 and 300 μg/ml. (λ_{ex} = 650-725nm, 50μJcm^{-2} per pulse)

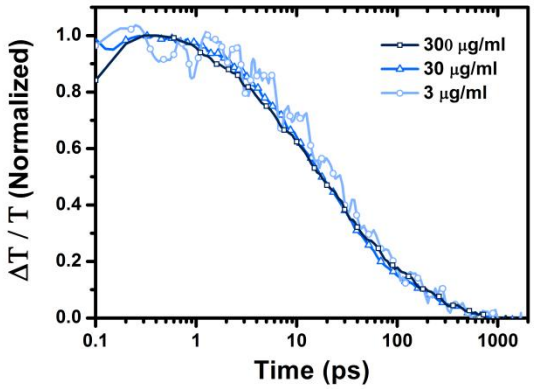

APPENDIX D

Supplementary Information for Chapter 5

Table D.1. Characterization results for PI-*b*-PDMAEMA, PI and PDMAEMA.*

Polymers	PI M_n (kg/mol)	PDMAEMA M_n (kg/mol)	PDI
PI-*b*-PDMAEMA-1	14.0#	4.9	1.03
PI-*b*-PDMAEMA-2	17.3	10.4	1.06
PI	9.7	-	1.06
PDMAEMA	-	4.8	1.10

* Molar masses and PDI's for PI-*b*-PDMAEMA-1, PI-*b*-PDMAEMA-2 and PI were determined from GPC with tetrahydrofuran as eluent. Molar mass and PDI for PDMAEMA homopolymer was determined from GPC with N,N-dimethylformamide as eluent, against a polystyrene calibration curve. PDMAEMA molar masses for the block copolymers were determined from ^{1}H NMR.

Molar mass for the PI block for PI-b-PDMAEMA-1 polymer was determined by 1H NMR, taking the sec-butyl initiator as the standard.

Figure D.1. Determination of critical micelle concentrations (CMC) for (a) PI-*b*-PDMAEMA-1 and (b) PI-*b*-PDMAEMA-2 using dynamic light scattering measurements.

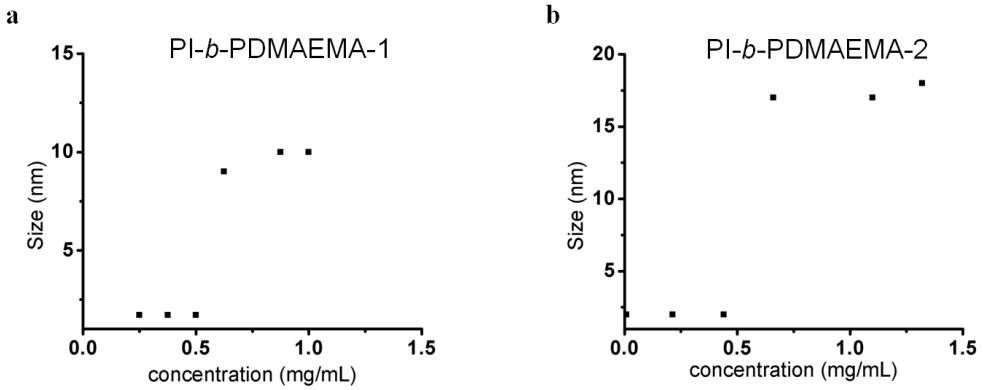

Figure D.2. Chemiluminescence emission profiles of free parent dye on addition of PEI at different concentrations.

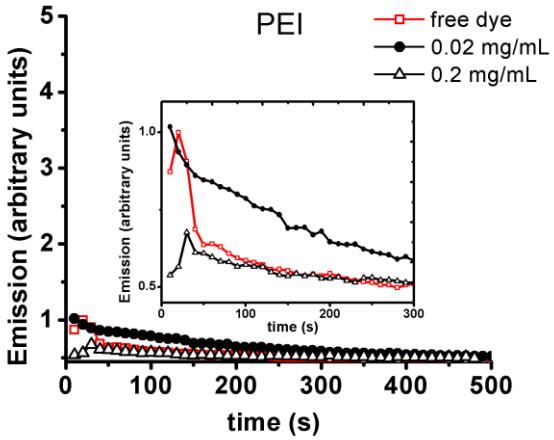

Calculations for oxalate molecules from ^{1}H-NMR measurements:

From ^{1}H-NMR measurements we can quantify the amount of CPPO (compound I), compound II and compound IV after addition of PEI. The peaks were integrated and normalized w.r.t. the remaining CPPO peak.

From the ^{1}H-NMR experiments we get the ratio of the integrals for compound I (δ: 7.71 ppm), compound II (δ: 7.67 ppm), and compound IV (δ: 7.63 ppm). Since CL depends on the amount of compound I, compound II and compound III, we need to calculate the amount of compound III indirectly from the amount of compound IV from the ^{1}H-NMR results. Reaction a, shows that one mole of Compound II was formed at the expense of one mole of compound IV, and reaction b shows that compound III was formed at the expense of 2 moles of compound IV.

From the above information we can define concentrations for each of the oxalates after PEI/PDMAEMA addition as:

Concentration of Compound I = $\frac{\text{Integral of compound I}}{2} = \frac{I_I}{2}$

Concentration of Compound II = Integral of compound II = I_{II}

Concentration of Compound IV = Integral of compound IV = I_{IV}

Calculation for concentration of compound III:

One mole of compound III is formed along with 2 moles of compound IV = $I_{IV} - I_{II}$ = Integral value of two protons from compound IV

Therefore, concentration of compound III = $\frac{I_{IV} - I_{II}}{2}$

Total oxalate in solution = initial CPPO concentration = $\frac{I_I}{2} + I_{II} + \frac{I_{IV} - I_{II}}{2} = \frac{I_I + I_{IV} + I_{II}}{2}$

The mole fraction for each of the oxalate compound can be calculated w.r.t. total oxalate concentration:

Mole fraction of compound I = $\frac{\frac{I_I}{2}}{\frac{I_I+I_{IV}+I_{II}}{2}}$

Mole fraction of compound II = $\frac{I_{II}}{\frac{I_I+I_{IV}+I_{II}}{2}}$

Mole fraction of compound III = $\frac{\frac{I_{IV}-I_{II}}{2}}{\frac{I_I+I_{IV}+I_{II}}{2}}$

e.g. for a PEI concentration of 0.05 mg/mL –

The ratio of ^{1}H-NMR integrals for compound I : II : IV gave a molar ratio of 1 : 0.16 : 0.37 respectively.

Total oxalate concentration = 0.765

Mole fraction of compound I = $\frac{0.5}{0.765} = 0.65$

Mole fraction of compound II = $\frac{0.16}{0.765} = 0.21$

Mole fraction of compound III = $\frac{0.105}{0.765} = 0.14$

The same method was used to calculate the mole fraction for the various oxalates at different PEI concentration.